QUANTITATIVE T_2 MAPPING IN CARDIAC MRI

By

Tomoe Barr

A Thesis Submitted to the Faculty of the

GRADUATE INTERDISCIPLINARY PROGRAM IN BIOMEDICAL ENGINEERING

In Partial Fulfillment of the Requirements for the Degree of

MASTER OF SCIENCE
WITH A MAJOR IN BIOMEDICAL ENGINEERING

In the Graduate College

THE UNIVERSITY OF ARIZONA

2012

STATEMENT BY AUTHOR

This thesis has been submitted in partial fulfillment of requirements for an advanced degree at The University of Arizona.

Brief quotations from this thesis are allowable without special permission, provided that accurate acknowledgment of the source is made. Requests for permission for extended quotation from or reproduction of this manuscript in whole or in part may be granted by the head of the major department or the Dean of the Graduate College when in his or her judgement the proposed use of the material is in the interests of scholarship. In all other instances, however, permission must be obtained from the author.

SIGNED: Tomoe Barr

APPROVAL BY THESIS DIRECTOR

This thesis has been approved on the date shown below:

Maria I. Altbach, PhD
Associate Professor of Radiology

Date

ACKNOWLEDGEMENTS

I would like to express my sincere gratitude to my mentor, Dr. Maria I. Altbach for her advice, guidance, and support throughout my graduate studies. I am also thankful to the faculty members who served on my committee: Drs. Ali Bilgin, J.P. Galons, and Phillip Kuo. I am indebted to them for their support as well as the knowledge and experience they have imparted upon me.

I would also like to thank the following inspirational people whom I have met during my time as a graduate student: Mr. Scott W. Squire, a senior research specialist, has taught me how to operate a MRI scanner and given me insightful and valuable advice. Dr. Theodore Trouard taught my first graduate course in biomedical engineering on medical imaging. Drs. Aiden Abidov, Bujji Babu Ainapurapu, Dipak Babu KC, and Jaspreet Singh have collaborated with our group for the cardiac MRI studies discussed herein and their perspective as medical professionals has been invaluable. As a radiologist with expertise in CMR, Dr. Ryan Avery instructed me regarding the interpretation of CMR images.

I would also like to acknowledge the fellow students I have worked and studied with. My former colleague in our lab, Dr. Chuan Huang, has given me tremendous amount of advice, especially regarding the algorithms developed in our group. Mahesh Bharath Keerthivasan and Vineeth Abraham have shared both their academic experience and their friendships. Dr. Christian Graff has been a great friend and a mentor to me since my undergraduate studies, and I am indebted to him for introducing me to the MRI research that ultimately led me to this group.

Although there are many others to whom I owe my gratitude, I would like to end by thanking my husband, Joshua Barr, for his support in all aspects of my life, as well as my parents, who supported my undergraduate studies overseas and who have always believed in me.

TABLE OF CONTENTS

TABLE OF CONTENTS – *continued*

TABLE OF CONTENTS – *continued*

LIST OF TABLES

LIST OF FIGURES

LIST OF FIGURES – *continued*

LIST OF FIGURES – continued

LIST OF FIGURES – continued

ABSTRACT

The thesis discusses a quantitative method to examine the myocardium using an MR-dependant tissue parameter known as the spin-spin relaxation time, T_2. This parameter is related to cardiac pathologies, such as myocardial edema, or inflammation. The goal of my project was to optimize a data acquisition technique (double-inversion radial fast spin echo or DIR-RADFSE), previously developed in Dr. Altbach's lab, for cardiac MRI applications. The data collected with DIR-RADFSE can be used to calculate T_2 via specialized reconstruction algorithms. First, the setups with DIR-RADFSE sequence were optimized with the goal of reducing artifacts due to aliasing, chemical shift, indirect echoes and cardiac motion (due to higher heart rates). Then, reproducibility studies were conducted on healthy controls to evaluate the reproducibility of the T_2 values in the myocardium. The technique was also tested on patients who were undergoing a routine clinical examination. The results of this initial clinical study are presented in the thesis.

CHAPTER 1

BASICS OF MAGNETIC RESONANCE IMAGING

Magnetic Resonance Imaging (MRI) is a non-invasive imaging modality used clinically to produce images of the human body with excellent soft tissue contrast. MRI utilizes non-ionizing radiation, and allows the acquisition of 3D images. Fundamentally, MRI is based on the Nuclear Magnetic Resonance (NMR) phenomena. As such, in this chapter the fundamental elements of NMR phenomena are introduced along with those of MRI.

1.1. Nuclear Magnetic Resonance phenomena

1.1.1. Introduction

Nuclei that have an odd number of nucleons (protons and neutrons) possess a net spin, and for the purposes of MRI and NMR, they can be interpreted semi-classically as charged particles that spin uniformly around an axis passing through their center. Such nuclei have an intrinsic nuclear angular momentum, **L**, which we refer to here simply as spin, as well as a magnetic moment $\boldsymbol{\mu}$ as depicted in Figure 1.1. The magnetic moment is proportional to the net angular momentum,

$$\boldsymbol{\mu} = \gamma \mathbf{L}\,, \tag{1.1}$$

where γ is the gyromagnetic ratio.

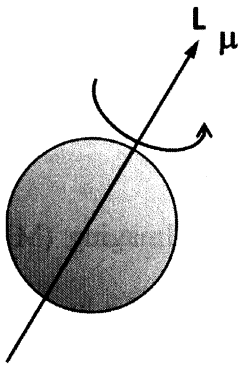

Figure 1.1. A spinning charged particle.

The latter is the ratio of a point charge q with mass m engaged in a circular motion ($\gamma = q/2m$). It is important to note that the gyromagnetic ratio is a nuclei-dependent constant that varies from element to element. For example, hydrogen (^{1}H), which is the most abundant species in the human body, has a relatively large gyromagnetic ratio ($2.675 \times 10^{8}\ radian \cdot s^{-1} \cdot T^{-1}$) due to its small mass (^{1}H has only one proton and a neutron in its nucleus), whereas ^{31}P, which is an element found in bones (85%) and is an essential part of the molecules related to energy production in cells, has γ of $1.083 \times 10^{8}\ radian \cdot s^{-1} \cdot T^{-1}$[1].

In classical terms, when spin-possessing nuclei, like the ^{1}H nucleus, are placed in an external magnetic field, a torque causes the spins to precess about the main direction of the magnetic field, $\mathbf{B}_0$.

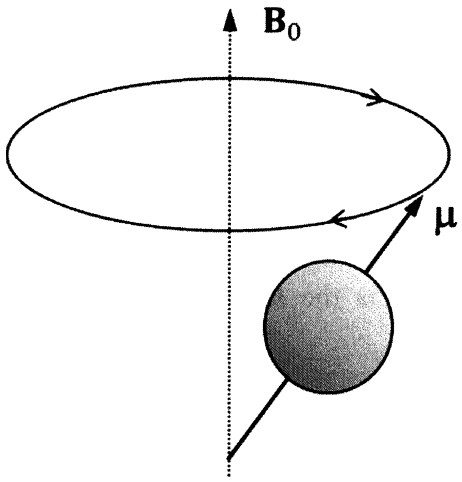

Figure 1.2. A spin precessing around an external magnetic field $\mathbf{B}_0$.

The precession frequency is called the Larmor (or resonant) frequency and can be expressed as:

$$\omega_0 = \gamma \mathrm{B}_0. \tag{1.2}$$

For example, at 1.5T (a typical magnetic field strength in the context of clinical MRI), the Larmor frequency of ^{1}H is 63.86 MHz.

Within quantum mechanics, a spin ½ nucleus can only exist in one of two energy states. In the low energy state, denoted as n_+, spins are aligned with the external magnetic field whereas in the high energy state, n_-, spins are aligned opposite to it. The Boltzmann distribution gives the distribution of spins in equilibrium at finite temperature, i.e.:

$$\frac{n_-}{n_+} = e^{-\frac{\gamma \hbar \mathrm{B}_0}{kT}}. \tag{1.3}$$

where k is Boltzmann's constant, $\hbar$ is the Planck's constant, h, divided by 2π, and T is the absolute temperature of the system. As the thermal energy scale, kT, is far greater than the magnetic energy scale, the nuclei exhibit only a slight preference for the lower energy state. This slight excess of spins in the lower energy state gives rise to a net magnetization **M**, which is the total sum of the nuclear magnetic moments per unit volume.

$$\mathbf{M} = \Sigma\ \boldsymbol{\mu}. \tag{1.4}$$

1.1.2. Signal generation and detection

The net magnetization vector, **M**, does not generate a detectable signal directly. Rather, an oscillating RF field is applied to perturb the net magnetization, **M**, away from preferred direction, which is dictated by the primary magnetic field, $\mathbf{B_0}$, as described above. When the frequency of this RF pulse matches the Larmor frequency of the nuclei, resonance occurs and the nuclear spins can be "tipped" toward the XY plane, as depicted in Figure 1.3 for a "flip angle" of α°. As a whole, this process gives rise to a changing magnetic field produced by the nuclei, and therefore induces a measurable voltage within a receiver coil.

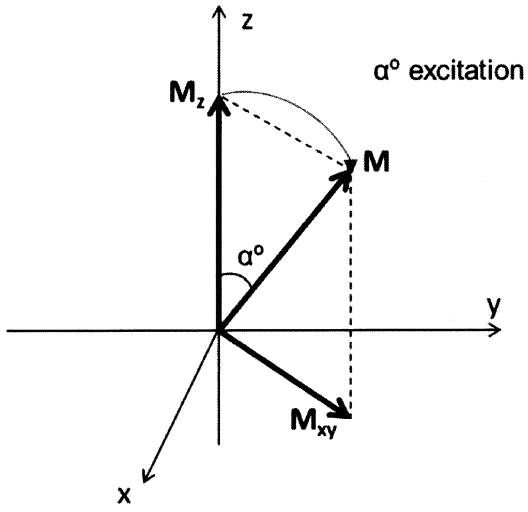

Figure 1.3. Magnetization after and α° RF pulse is applied.

At this point the magnetization **M** can be divided into two components, the longitudinal component $\mathbf{M_z}$ (component along the axis of the $\mathbf{B_0}$ field) and the transverse component $\mathbf{M_{xy}}$ (component in the XY plane). These components can be expressed in terms of the tip angle as:

$$\mathbf{M}_{xy} = |\mathbf{M}| \sin \alpha \tag{1.5}$$

$$\mathbf{M}_z = |\mathbf{M}| \cos \alpha \tag{1.6}$$

Since $\mathbf{M_{xy}}$ produces the detectable signal, it is desirable to set the flip angle to 90° in order to obtain the largest possible transverse magnetization.

1.1.3. Longitudinal and transverse relaxation

The detected signal decays over time due to two relaxation mechanisms. The first of these is a longitudinal relaxation that causes $\mathbf{M_z}$ to relax to its original state, $\mathbf{M_0}$, as a

result of energy exchange between the spins and the surrounding tissue (the lattice). Thus, the longitudinal relaxation is also known as the spin-lattice relaxation and is described by:

$$\frac{\mathbf{dM_z}}{\mathbf{dt}} = -\frac{\mathbf{M_z - M_0}}{\mathbf{T_1}}, \tag{1.7}$$

where T_1 is the time constant that describes the recovery time. Integrating over time, Equation 1.7 becomes:

$$\mathbf{M_z}(t) = \left(1 - e^{-\frac{t}{T_1}}\right)\mathbf{M_0}. \tag{1.8}$$

Figure 1.4 shows the recovery of the magnitude of $\mathbf{M_z}$ to its equilibrium value of M_o. Note that at ~5 T_1, the magnitude of $\mathbf{M_z}$ is ~ M_o.

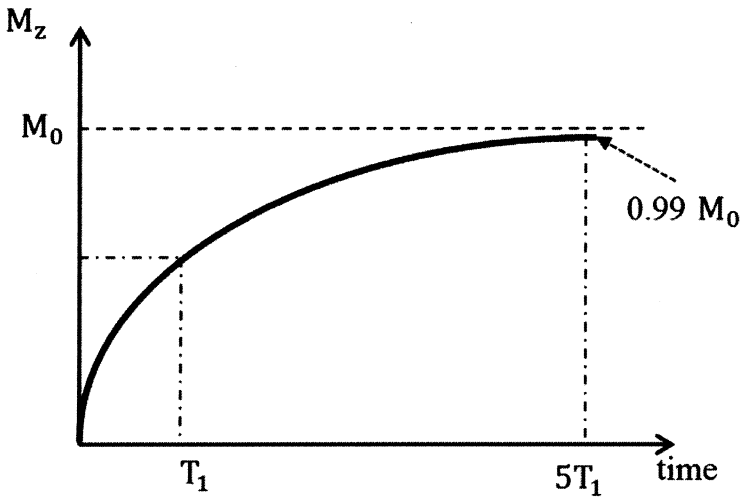

Figure 1.4. T_1 relaxation.

In the transverse plane, the net $\mathbf{M_{xy}}$ magnetization will also decay from its initial value (i.e. the value immediately after the RF excitation) due to the interaction with local magnetic fields produced by neighboring spins. These perturbations due to local magnetic

fields alter the resonant frequencies of the spins, thereby causing the nuclear spins to precess at different rates, ultimately resulting in dephasing as shown in Figure 1.5.

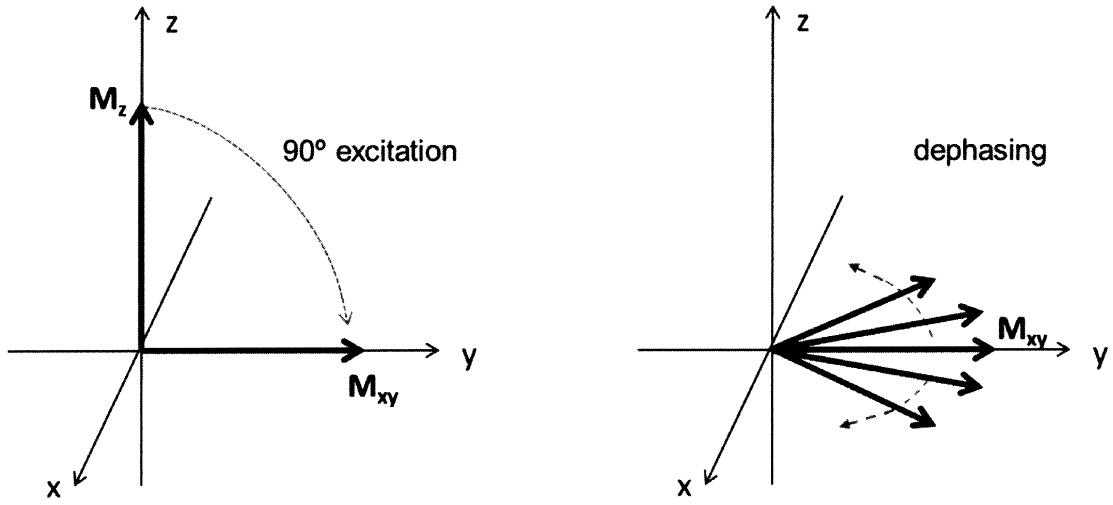

Figure 1.5. Dephasing of spins after a 90° RF excitation.

When spins are completely dephased the net magnetization, $\mathbf{M_{xy}}$, becomes zero, although it is important to note that the individual nuclei still possess magnetic moments with transverse components. This relaxation mechanism is called transverse or spin-spin relaxation and is described by:

$$\frac{d\mathbf{M_{xy}}}{dt} = -\frac{\mathbf{M_{xy}}}{T_2}, \tag{1.9}$$

where T_2 is the time constant that describes the temporal scale associated with the dephasing. Integrating Equation 1.9 over time gives:

$$\mathbf{M_{xy}}(t) = \mathbf{M_{xy}}(0)e^{-\frac{t}{T_2}}, \tag{1.10}$$

where $\mathbf{M_{xy}}(0)$ is $\mathbf{M_{xy}}$ at time = 0. Figure 1.6 shows the decay of the magnitude of $\mathbf{M_{xy}}$.

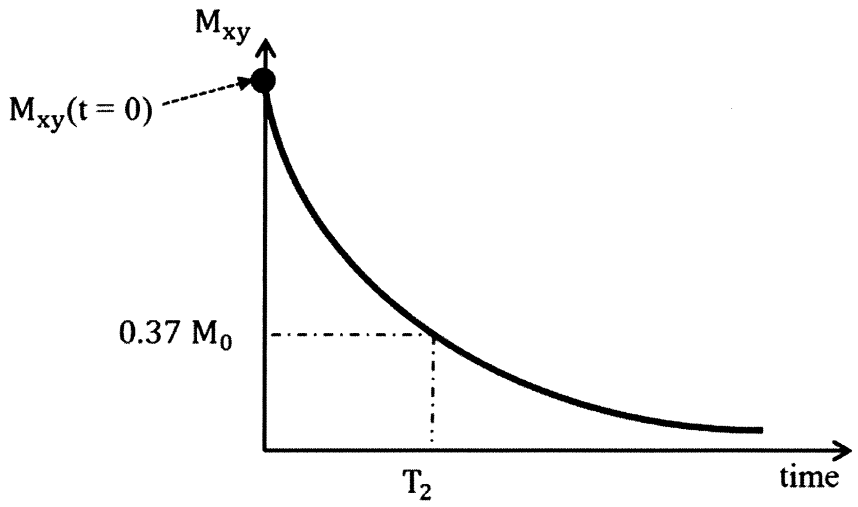

Figure 1.6. T_2 relaxation.

1.2. Magnetic resonance imaging (MRI)

In an MRI experiment, the NMR signal needs to be spatially encoded by using a gradient field. This makes it possible to resolve the signal spatially in the direction in which the gradient field is applied. In two dimensional (2D) MRI, a slice is selected by exciting only the spins lying within a plane, a process known as slice selection, and then in-plane spatial encoding takes place. For example, if the slice selection direction is along the Z axis, and the in-plane spatial encoding plane is parallel to the XY plane, then the applied gradient fields are noted as: $\mathbf{G_x}$, , $\mathbf{G}_y$, and $\mathbf{G_z}$ in the X, Y, and Z directions, respectively. The gradients allow us to extract the information on the proton's distribution along the gradient direction [1].

1.2.1. Slice selection

In order to resolve the signal spatially along the Z axis, a slice-select magnetic field gradient, $\mathbf{G}_z$, is applied. This gradient field causes changes in the effective net magnetic field and therefore the resonant frequencies of the nuclei, to vary as a function of position along the Z axis:

$$\omega(z) = \gamma(B_0 + G_z z). \tag{1.11}$$

Thus, using a frequency-selective RF transmit pulse (i.e., a pulse that only excites a certain range of frequencies) it is possible to excite spins within a specific region along the Z axis.

The bandwidth of the RF pulse and the strength of the $\mathbf{G}_z$ gradient determine the slice thickness. This is illustrated in Figure 1.7, where the thickness of the selected slice is depicted as Δz. In order to change the slice location, z', the central excitation frequency of the RF pulse is adjusted according to the gradient $\mathbf{G}_z$.

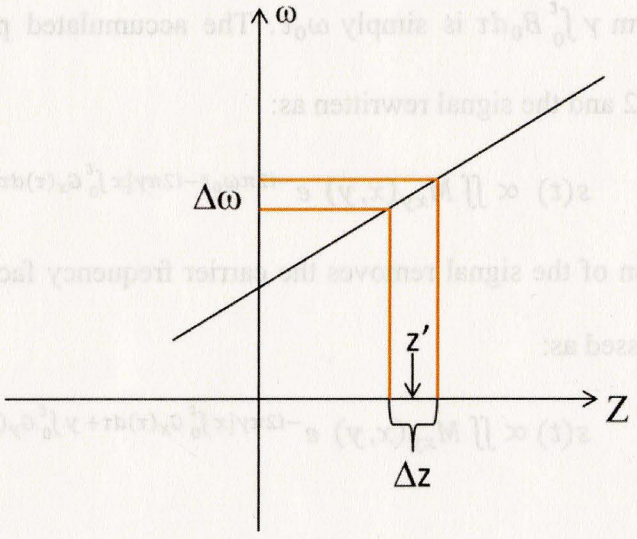

Figure 1.7. Slice selection at the slice location, z', with the slice thickness Δz.

1.2.2. In plane spatial encoding

After the slice selection, the transverse magnetization will contribute to the detectable signal, which is proportional to the sum of $M_{xy}(x,y)$ at all locations:

$$s(t) \propto \iint M_{xy}(x,y)e^{-i2\pi\omega t}\, dxdy \tag{1.12}$$

[2]. The signal described in Equation 1.12 is not spatially resolvable in the XY plane. In plane spatial encoding is achieved by applying the frequency encoding gradient, $\mathbf{G_x}$, and the phase encoding gradient, $\mathbf{G_y}$. When these gradients are applied the Larmor frequency of the spins changes with location:

$$\omega(x,y) = \gamma(B_0 + G_x x + G_y y) \tag{1.13}$$

at a particular instant in time. By making the gradient term **G** in Equation 1.13 time dependent, **G**(t), the accumulated phase, ωt, of the precessing magnetization over time due to a time-dependent gradient can be expressed as:

$$\omega t = \gamma \int_0^t B_0 d\tau + \gamma x \int_0^t G_x(\tau)d\tau + \gamma y \int_0^t G_y(\tau)d\tau\,. \tag{1.14}$$

The first term $\gamma \int_0^t B_0 d\tau$ is simply $\omega_0 t$. The accumulated phase can be inserted into Equation 1.12 and the signal rewritten as:

$$s(t) \propto \iint M_{xy}(x,y)\; e^{-i2\pi\omega_0 t - i2\pi\gamma[x\int_0^t G_x(\tau)d\tau + y\int_0^t G_y(\tau)d\tau]}dxdy. \tag{1.15}$$

Demodulation of the signal removes the carrier frequency factor $e^{-i2\pi\omega_0 t}$ and the signal can be expressed as:

$$s(t) \propto \iint M_{xy}(x,y)\; e^{-i2\pi\gamma[x\int_0^t G_x(\tau)d\tau + y\int_0^t G_y(\tau)d\tau]}dxdy. \tag{1.16}$$

This temporal signal is the 2D Fourier transform of $M_{xy}(x,y)$ at spatial frequencies, $(\frac{\gamma}{2\pi}\int_0^t G_x(\tau)d\tau,\ \frac{\gamma}{2\pi}\int_0^t G_y(\tau)d\tau)$. The spatial frequencies can be denoted as $k_x(t)$ and $k_y(t)$:

$$k_x(t) = \frac{\gamma}{2\pi}\int_0^t G_x(\tau)d\tau \tag{1.17}$$

$$k_y(t) = \frac{\gamma}{2\pi}\int_0^t G_y(\tau)d\tau \tag{1.18}$$

and the Equation 1.16 is simplified to:

$$s(t) \propto \iint M_{xy}(x,y)\ e^{-i2\pi[k_x(t)x+k_y(t)y]}dxdy \tag{1.19}$$

Equation 1.19 shows that the signals *s(t)* are samples of the Fourier transform of M_{xy}, where $k_x(t)$ and $k_y(t)$ exist in a domain called k-space.

The set of $s(t)$ samples must be collected to fill a sufficient part of k-space to allow reconstruction of $\mathbf{M_{xy}}$. In order to do so, the Nyquist sampling criterion must be satisfied, which states that data must be sampled such that the inverse of the sampling step in k-space, Δk, is larger than the size A of the object to be imaged [1]. This means that the field-of-view (FOV) must be larger than the object size A:

$$FOV_x > A_x, or\ \Delta k_x < 1/A_x$$

$$FOV_y > A_y, or\ \Delta k_y < 1/A_y \tag{1.20}$$

Thus, the uniform sampling in k-space is done satisfying Equation 1.20.

1.3. K-space trajectories

A sampling trajectory is a complete path taken to sample the k-space data. There are different trajectories that can be designed by manipulating the gradients. The most common k-space trajectory is based on a Cartesian grid.

1.3.1. Cartesian k-space trajectory

In a Cartesian k-space trajectory, data are collected in a rectilinear pattern. Data for a line (row) is sampled first along one of the directions (k_x direction); subsequent lines are filled until the other direction (k_y direction) has the required sampling. This is illustrated in Figure 1.8.

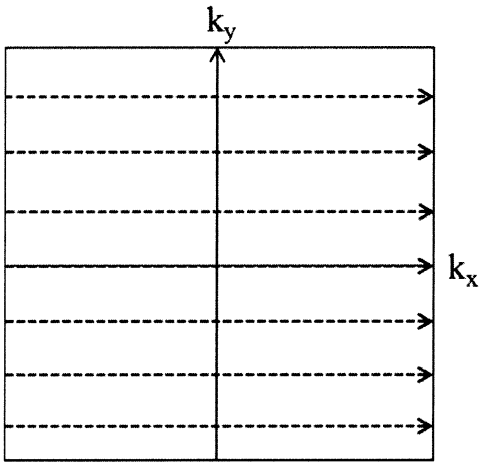

Figure 1.8. Cartesian k-space trajectory.

The image can be reconstructed from the k-space data via the use of the 2D inverse discrete Fourier transform (IDFT).

1.3.2. Radial k-space trajectories

Another trajectory used in MRI is the radial k-space trajectory where the points are sampled on a polar grid. In radial trajectories, data are acquired along lines extending radially outward, as shown in Figure 1.9.

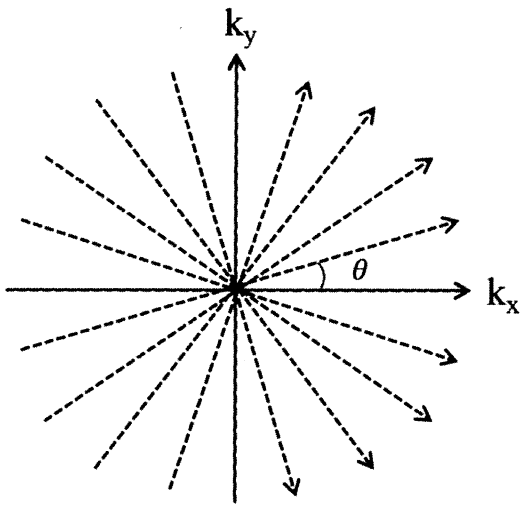

Figure 1.9. Radial k-space trajectory.

Each radial k-space line (view) goes through the center of k-space with an angle θ with respect to the k_x axis. By varying the value of θ during the different acquisition periods, different radial k-space lines can be collected. Because the center of k-space is oversampled, radial acquisitions have the advantage of reducing artifacts due to motion [3]; i.e. by heavily sampling the data near the center of k-space, the effects of motion are averaged out. However, the high spatial frequency regions of k-space are comparatively sparse. As long as the Nyquist criterion is satisfied, aliasing can be avoided. The Nyquist criterion in a radial trajectory is satisfied when the distance between two sampled points

in the azimuthal direction (Δk_θ) equals the distance between two sampled points in the radial direction (Δk_r). The radius, r, at which this condition is satisfied is called the Nyquist radius and it is illustrated in Figure 1.10. From the expression

$$\Delta k_r = \Delta k_\theta = 2r sin\left(\frac{\theta}{2}\right), \tag{1.21}$$

we can derive a relationship between the number of acquired points in the radial (N_r) and azimuthal (N_θ) directions that satisfies the Nyquist condition. Using the approximation $\sin(\theta/2) \sim \theta/2$ for small angles, Equation 1.21 can be reformulated as:

$$\Delta k_\theta = r\theta. \tag{1.22}$$

Using $\theta = \pi / N_\theta$:

$$\Delta k_\theta = \frac{r\pi}{N_\theta}. \tag{1.23}$$

Since $\Delta k_r = {}^{2r}/_{N_r}$, the equation $\Delta k_r = \Delta k_\theta$ becomes

$$\frac{2r}{N_r} = \frac{r\pi}{N_\theta}, \tag{1.24}$$

which can be reduced to:

$$N_\theta = \frac{\pi}{2} N_r. \tag{1.25}$$

Equation 1.25 gives the relationship between the number of projections and number of readout points needed to satisfy the Nyquist condition.

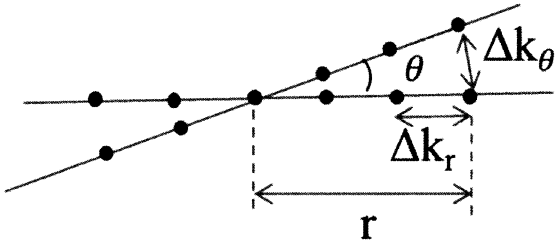

Figure 1.10. Nyquist sampling illustration.

Radially acquired data can be reconstructed using gridding or filter backprojection (FBP). The gridding technique re-grids the radially sampled data points onto a Cartesian grid and reconstructs it using an IDFT. FBP is based upon the central slice theorem. In this technique, each radial k-space line is multiplied by a ramp filter, |k|, to compensate for differences in the sampling density. A 1D FT of each line of the data then yields a "filtered projection" of the object. The projections of all the lines are then back-projected on the 2D space to reconstruct an image [1].

1.4. Spin-echo (SE) imaging

Section 1.1.3 described the dephasing of the transverse magnetization due to spin-spin interactions (i.e., T_2 relaxation), which is a random process dependent on fluctuations in the local magnetic fields caused by other spins. In real MRI systems, additional dephasing is created by the magnetic field inhomogeneity and susceptibility effects caused by tissues surrounding the spins. This additional dephasing can be modeled using T_2'. In this case, the overall transverse magnetization can be written using a different parameter, T_2^*,

$$\mathbf{M_{xy}}(t) = \mathbf{M_{xy}}(0)e^{-\frac{t}{T2^*}}, \tag{1.26}$$

where:

$$\frac{t}{T_2^*} = \frac{t}{T_2} + \frac{t}{T_2'} \tag{1.27}$$

The so-called joint *free induction decay* (FID) time, T_2^*, is smaller than T_2. The additional dephasing given by T_2' happens in a fixed location affected by an external magnetic field inhomogeneity and the sample dependent susceptibilities. It is important to note that T_2' relaxation is reversible whereas T_2 relaxation is not due to the random nature of the latter.

1.4.1. Spin-echo (SE) experiment

Because T_2 is a parameter that is related to tissue properties, it is important to measure it. In order to get pure T_2 decay, the spin-echo (SE) technique is used to reverse the T_2' relaxation discussed above. Figure 1.11 describes the SE experiment. After a 90° RF excitation pulse (step 1), the spins dephase due to T_2 and T_2' effects as depicted in Figure 1.11 (step 2), by the spreading of the black arrows. After a delay equal to τ, a 180° refocusing pulse is applied about the X-axis. The latter causes the spins to flipped over to the opposite direction along the Y-axis (step 3). This brief refocusing pulse reverses the direction of spin dephasing, and after a second τ delay the T_2' effects are rephased (step 4) and spins are refocused in the –Y direction (step 5). The point where the spins are refocused is called the spin-echo (SE) point.

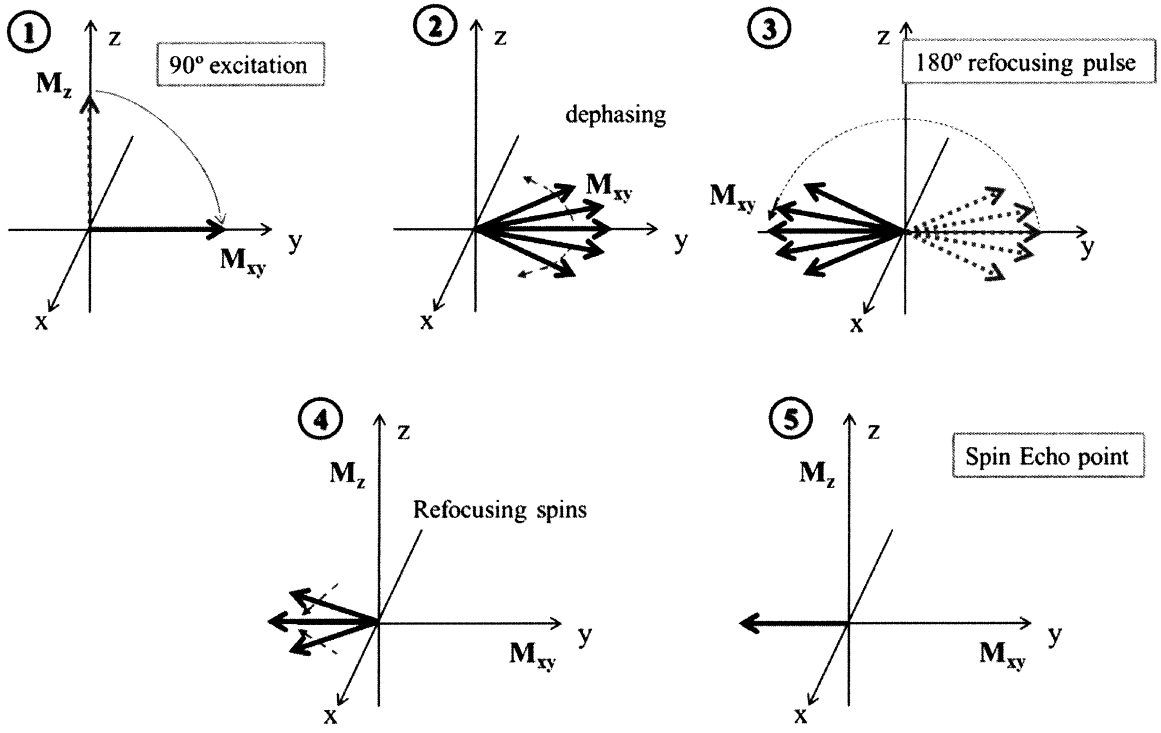

Figure 1.11. Spin-echo experiment.

Figure 1.12 shows a typical SE experiment as well as the signal decay of the transverse magnetization under the T_2^* and T_2 mechanisms. Note that the detected signal is an echo at time = 2τ from the 90° excitation (the SE point). At the SE point the decay due to T_2^* relaxation is refocused but the decay due to T_2 is not. Thus a SE experiment allows for the measurement of the true T_2 decay from the signal envelope.

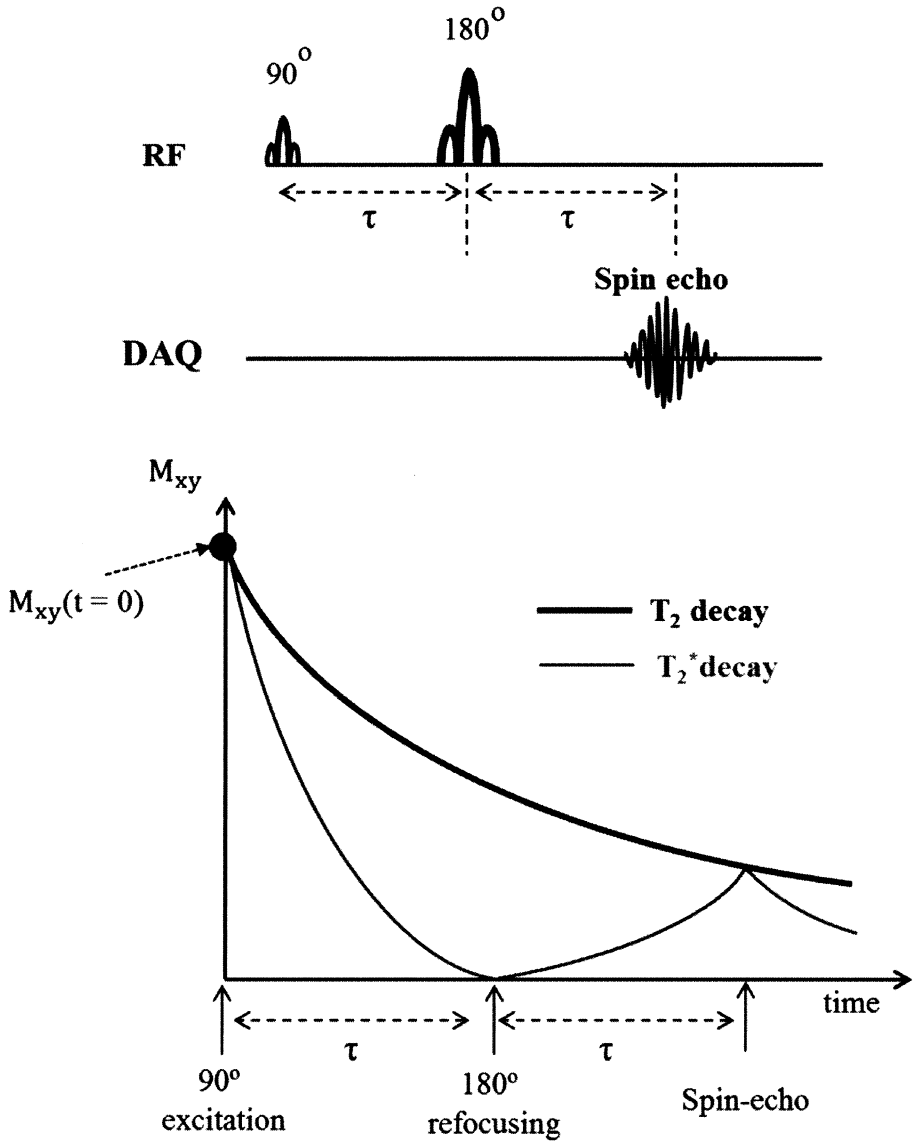

Figure 1.12. Spin-echo experiment and the signal decay due to T_2 and T_2^* relaxation.

1.4.2. Fast spin echo (FSE) imaging experiments

A typical SE MRI experiment is shown in Figure 1.13. The transverse magnetization for a specific slice is generated after a 90° slice-selective excitation. Gradients in the phase encoding and readout axes (indicated in the figure as G_y, G_x,

respectively) are then applied to select a specific location in k-space. A slice-select 180° refocusing pulse is applied and the readout gradient is turned on to read a line of k-space. To collect the next line of k-space the experiment is repeated by changing the value of the phase encoding gradient. The central part of k-space is collected at the SE point. The time between the 90° excitation and a SE point is called the echo time (TE). The time between 90° excitations is called the repetition time, TR.

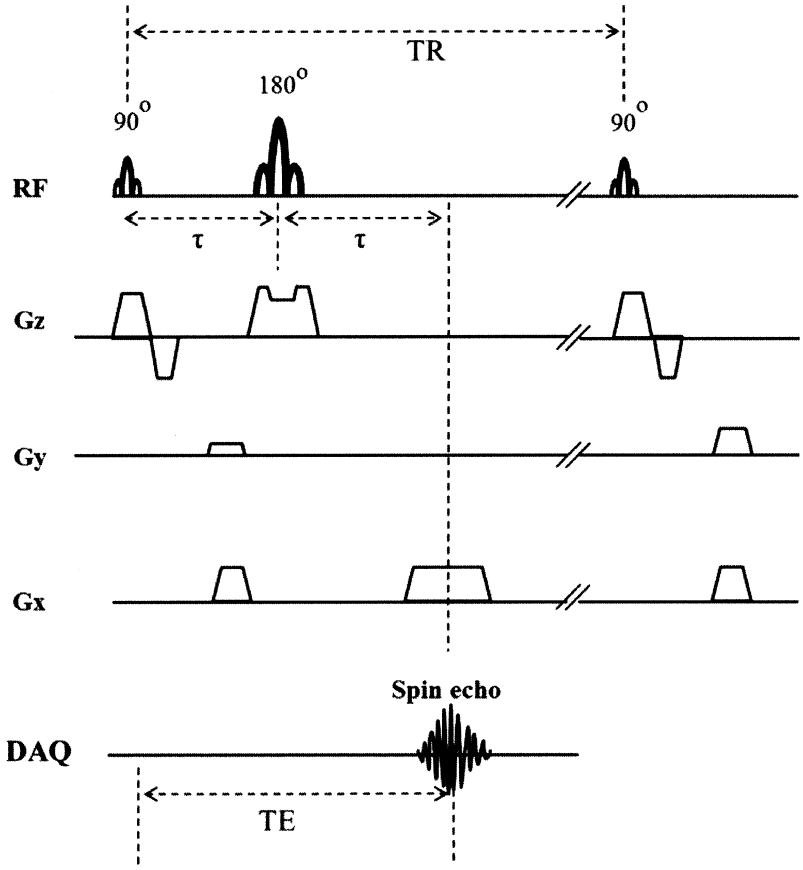

Figure 1.13. SE pulse sequence.

The total imaging time depends on the number of phase encoding (N_y) steps, TR, and the number of averages of excitations (NEX):

$$\text{Imaging time} = N_y \times TR \times NEX \tag{1.28}$$

In a typical SE MRI experiment, TR ranges from 1~ 4 s, thus it takes 4.26 ~17 minutes to collect 256 phase encoding steps for NEX=1.

In order to speed up data acquisition the FSE technique was developed [1]. Figure 1.14 shows a schematic diagram of the FSE pulse sequence. In the latter, a series of 180° pulses are added after the 90° excitation with the goal of refocusing the signal at multiple SE points within one TR period. Note that the amplitude of the G_y gradient is different for each SE point which allows for the acquisition of different k-space lines in one TR period. In an FSE pulse sequence the total scan time is reduced by the echo train length (ETL= total number of SE points within one TR period):

$$\text{Imaging time} = \frac{N_y \times TR \times NEX}{ETL}. \tag{1.29}$$

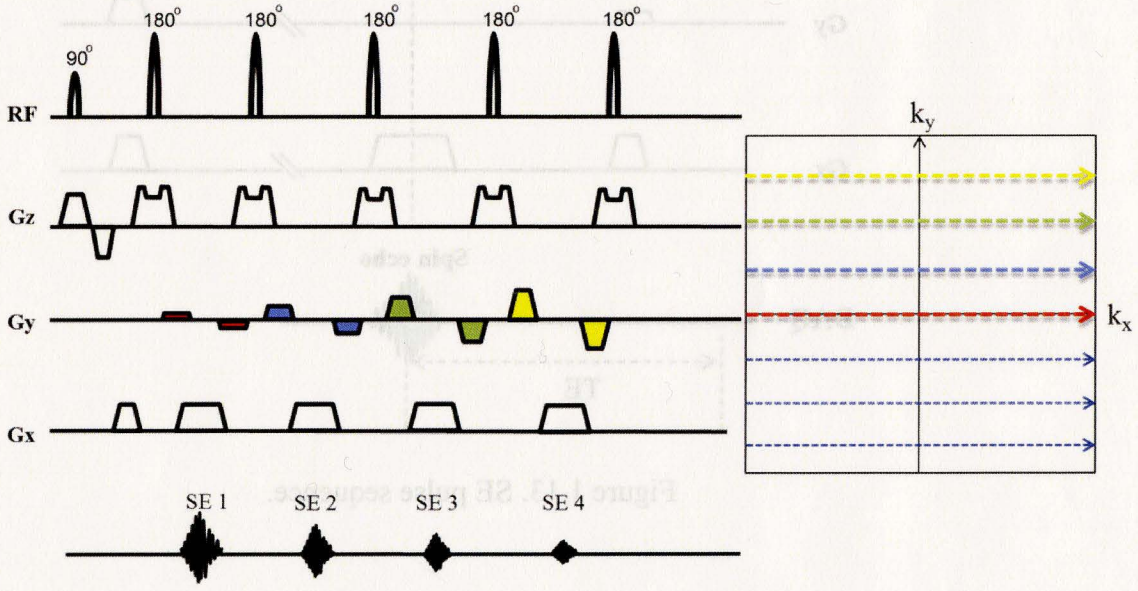

Figure 1.14. FSE pulse sequence and k-space readouts for ETL = 4.

1.4.3. Black-blood preparation

Flowing blood causes artifacts which are more prominent in cardiac imaging due to the fast flow of blood within the heart. In order to remove these artifacts, a technique called double inversion recovery (DIR) [4], takes place before data acquisition in SE and FSE cardiac imaging. The signal from flowing blood is suppressed with this technique, yielding images in which flowing blood appears black.

DIR consists of two 180° inversion pulses to null the signal from flowing spins without affecting the magnetization of the spins within the imaging slice. A schematic depiction of the DIR technique is shown in Figure 1.15 where all spins are assumed to start with the same magnetization, M_o. The first 180° inversion pulse is a non-selective pulse that inverts all spins within the range of the RF transmitter coil. Right after inversion, the magnetization of all spins is $-M_o$. The second RF pulse is a slice-selective 180° pulse that re-inverts the magnetization of spins within the selected imaging slice. As a result, the magnetization of the spins within the slice returns to M_o. The magnetization of spins outside the slice starts to recover at different rates for different components depending on their T_1 relaxation. If the time delay after the preparation period (TI) is chosen so that the blood magnetization reaches zero by the end of TI, the signal from all blood spins within the RF volume will be zero (null point). So blood flowing into the selected slice will not contribute to M_o at this point. Since the null point of blood is ~ 400 ms (for TR = 1RR and a heart rate of 60 bpm) or ~ 625 ms (for TR = 2RR and 60 bpm), blood that was re-inverted within the slice will have flown out of the slice for most subjects. [4]

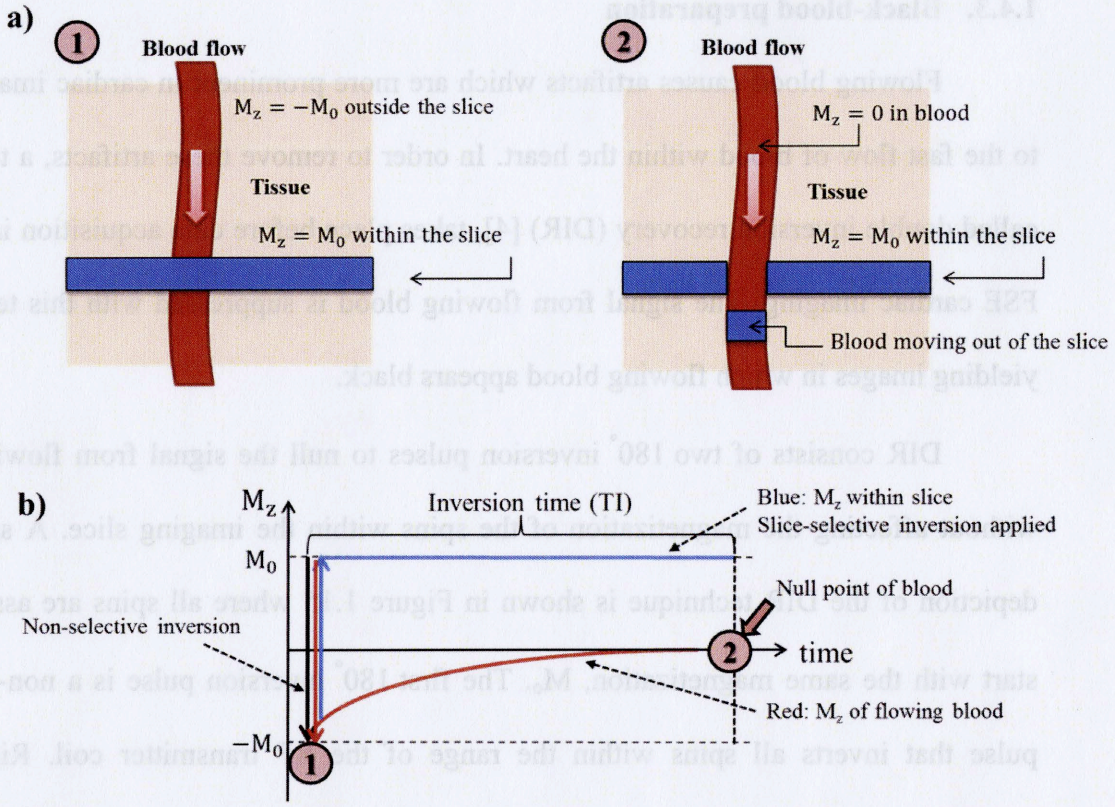

Figure 1.15. DIR Preparation Period to null the signal from blood: (a) illustration of DIR preparation, (b) red curve in the plot is M_z of blood, blue curve represents the M_z of non flowing spins within the slice.

It is important to note that if there is any steady blood within the slice selected, the blood will contribute to the signal. One of the examples where the steady blood signal can be seen is when an MI leads to cardiac dysfunction and the myocardium is no longer able to pump the blood out of the ventricles. Because the signal intensity of flowing blood has higher T_2, appearing brighter than surrounding tissue in T_2-weighted images even at a very long TE (i.e. TE > 100 ms); a trained observer can distinguish the signal from blood from the signal from myocardium.

Chapter 2

Cardiac Magnetic Resonance Imaging

2.1. Cardiac magnetic resonance (CMR)

CMR imaging is used in the clinic for evaluating the anatomy and the function of the heart. CMR is challenging because of the complex anatomy, the dynamic state of the heart and the cardiothoracic cavity, and the presence of blood flow and the lung fields. Thus, CMR requires imaging methods that are robust to motion, flow, and susceptibility artifacts. Moreover, when imaging the myocardium (which is the main goal of the work presented in the thesis) adequate spatial resolution is required since the thickness of myocardial wall is only 20~30 mm in the left ventricle (LV), and 2~3 mm in the right ventricle (RV).

Among the CMR protocols used to evaluate the myocardium, delayed-enhanced (DE) imaging is considered the gold standard in the evaluation of myocardial scar and viability in patients with coronary artery disease. In DE imaging, a Gadolinium (Gd)-based contrast agent is injected intravenously and images are acquired at approximately 10 – 15 minutes after injection. Gd reduces the T_1 relaxation of nearby water molecules, thus areas of abnormal contrast uptake are identified in the image as areas of high signal intensity (reduced T_1) relative to normal myocardium. An example of a DE image is shown in Figure 2.1 where the doughnut shape structure is the LV. Normal myocardium appears dark in the DE image. The regions of scaring due to myocardial infarction (MI) are "enhanced" compared to the normal myocardium.

Myocardial infarction is the end result of an ischemic condition of the heart where myocytes die (necrosis) [13]. Ischemia can be caused by the blockage of arteries that supply oxygen and nutrients to the myocardium. This necrotic event is irreversible. However, not all ischemic conditions lead to cell death and it is dependent on duration and severity of ischemia.

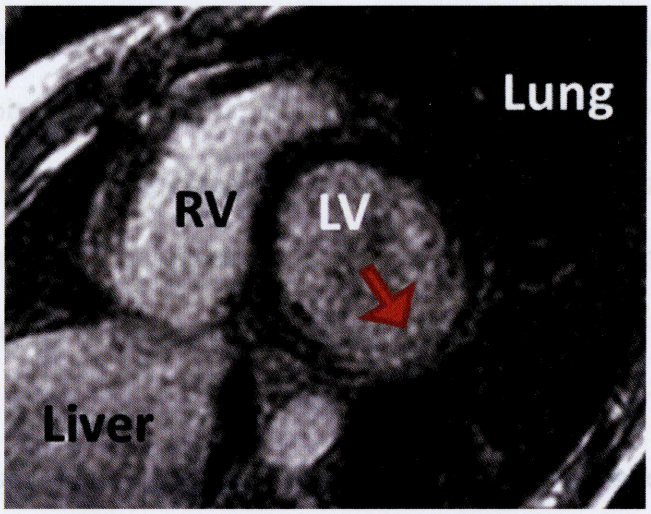

Figure 2.1. DE image, LV showing infarction scar (arrow).

2.2. Edema in the myocardium

Edema, or swelling, is a condition of the tissue in response to any acute injury regardless of its etiology. In the myocardium, edema represents an inflammatory response and is present as both swelling of the myocytes and accumulation of fluid in the interstitial space [13.]. As discussed above, the ischemic heart can lead to MI that is irreversible. However, unlike MI, less severe ischemic *injury* of the myocardium is reversible and the presence of edema is typical after injury. By detecting edema at an

early stage and with the right interventional treatment, the myocardium can regain its functionality. Therefore, detecting edema is critical for the management of patients.

2.3. Imaging edema in the heart via T_2-weighted black-blood imaging

T_2-weighted imaging can be done with the SE or FSE methods with TE long enough such that the different decay rates of the transverse magnetization of the two tissue types (normal myocardium and edema) provide a detectable contrast between them. This technique produces higher signal intensity in edema compared to normal myocardium due to the longer T_2 of the former.

Currently, the most frequently used T_2-weighted imaging technique is the short-TI triple inversion recovery prepared T_2-weighted sequence (triple IR) [14]. In this method, a third inversion pulse is added to the DIR preparation period. The third inversion pulse is slice-selective and is followed by a short TI (150ms) to null the signal from fat. Thus, the triple IR method suppresses signal from fat as well as from flowing blood. Figure 2.2 shows examples of T_2-weighted images acquired using the triple IR method.

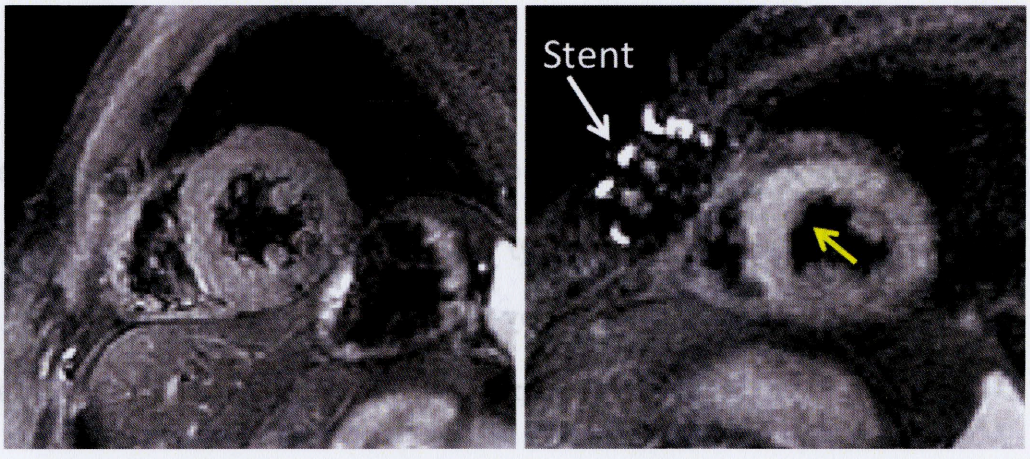

Figure 2.2. T_2-weighted images using Triple IR, edema at yellow arrow.

In the figure the image on the left is from a patient with hypertrophic cardiomyopathy; the image does not show any evidence of inflammation/edema. The image on the right is from a patient with coronary artery disease; the image shows areas of hyperintense signal (yellow arrow), likely representing myocardial edema. Of note, the hyperintense signal can also be amplified by the metallic stents' susceptibility.

The limitation of this technique is an inherent low signal-to noise ratio (SNR) due to the third inversion pulse. Another limitation is that data are acquired at one TE which may not be the optimal in terms of providing adequate contrast between the pathology and normal tissue. Currently, there is no standardized T_2-weighted imaging protocol for the diagnosis of edema in the heart. A problem, that is common to all methods that rely on changes in signal intensity for the identification of pathological changes, is the signal modulation caused by the use of multiple receivers (i.e., coil sensitivities). Because of these limitations it is often difficult to distinguish edematous areas from healthy myocardium. Due to the difficulty in carrying out diagnosis via qualitative T_2-weighted imaging, there is an increased interest in T_2 mapping of the myocardium.

2.4. T_2 mapping

Parametric mapping is a quantitative method where the parameters of a mathematical model are calculated by fitting the acquired data to the model. A parameter map yields parameters on a voxel-by-voxel basis. As indicated in Chapter 1, the signal decay due to T_2 relaxation can be represented by an exponential decay. Thus, for a set of

images acquired at different TE time points the signal intensity for a specific voxel can be represented by:

$$s(TE) = I_0\, e^{-TE/T_2} + \text{noise}. \tag{2.1}$$

where I_0 is initial signal intensity at TE = 0, which comes from transverse magnetization of protons in a voxel; data are acquired at TE = $\{TE_1, \ldots TE_n\}$. The T_2 value and I_0 can be found by conducting an exponential fit:

$$\widehat{I_0}, \widehat{T_2} = \; argmin_{I_0,T_2}\{\sum_n \left\| I_0 e^{-TE_n/T_2} - s(TE_n) \right\|\}\,. \tag{2.2}$$

In order to make the computation efficient, Equation 2.2 is linearized by taking the log to perform a linear least squares fitting. The Equation 2.2 becomes:

$$argmin_{I_0,T_2}\{\sum_n \left\| \log(I_0) - \frac{TE_n}{T_2} - \log(s(TE_n)) \right\|\}\,. \tag{2.3}$$

The outputs of this minimization are $\log(I_0)$ and T_2^{-1}, which is typically referred as R_2.

2.4.1. T_2 mapping using FSE

In 2009, Kim, et al. introduced a breath-hold multi-echo FSE pulse sequence for CMR R_2 quantification [5]. The method utilizes an ECG-triggered DIR multi-echo FSE pulse sequence to yield black-blood images at different TE time points from data acquired in a single breath hold.

In techniques based on multiple spin echoes to generate multiple TE images, there are signal variations between the even and odd echo points. These variations are caused by spins not being flipped to the desired angle by the refocusing pulses. By cycling the direction of the refocusing pulses between subsequent echoes in a multi spin-echo technique, the flip angle errors are corrected for the even echoes but not for the odd echoes. Thus, even echoes are more accurate than odd echoes for T_2 quantification [1]. In the multi-echo FSE pulse sequence developed by Kim et al, a turbo factor of two (ETL=2) is combined with a "reverse centric" k-space reordering. In the latter successive odd and even echoes (referred here as TE_n and TE_{n+1}, $n=1, 3, 5$ ...) fill in the outer and the inner halves of k-space, respectively. In other words, TE_n samples the inner half of k-space, as shown in Figure 2.3, whereas TE_{n+1} samples the outer half. The reverse centric k-space ordering minimizes the effects of echo asymmetry. In Kim's method data for 20 echo points are collected on each TR period yielding a total of 10 k-space data sets from which 10 TE images are reconstructed. From these images a voxel-wise R_2 map is calculated.

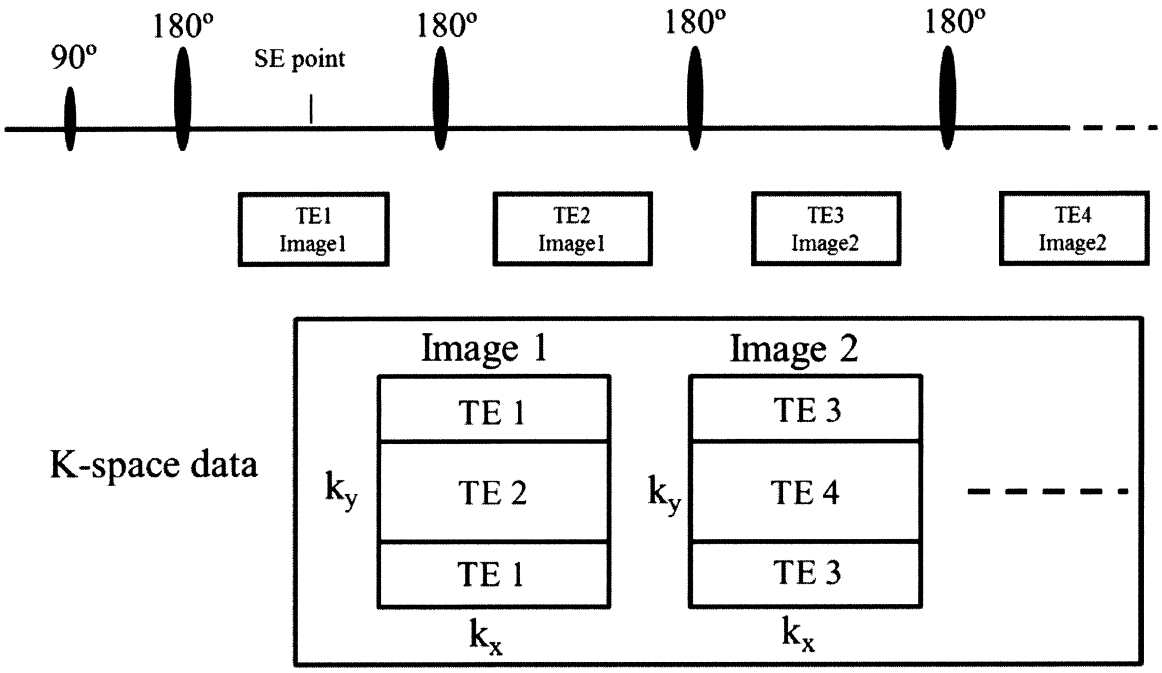

Figure 2.3. Reverse centric reordering in k-space.

Both the intra- and inter-studies showed excellent repeatability with p values < 0.001 and 0.002, for the sample sizes of five controls and three patients, and five controls, respectively. The drawback of the technique is the low spatial resolution of the images (2.66 × 3.83 mm) due to the limited number of points that are collected within a breath hold (acquisition matrix size = 128×45; after parallel imaging acceleration the matrix size is 128×72).

2.4.2. T_2 mapping using T_2 prepared-SSFP

Another technique recently developed for T_2 mapping of the heart is the T_2-prepared steady-state free-precession (T_2 prep-SSFP) method [6]. As shown in Figure 2.4 (a), a T_2 magnetization preparation (T_2-prep) period [7] is applied before a balanced steady-state free precession (b-SSFP) readout is used to acquire all k-space lines for one TE image. The acquisition is timed to readout data for each TE at the same time in the cardiac cycle. A recovery time of 3RR is used between images, as indicated in Figure 2.4 (b), to yield three TE images in seven RR intervals. Compared to the DIR FSE sequence the T_2 prep-SSFP is a bright-blood technique where blood appears brighter than the myocardium.

One of the drawbacks of the technique is that the TE images are collected sequentially which can introduce image misregistration. The fact that the technique is bright blood introduces problems due to partial volume (i.e., blood contaminating the T_2 values of the tissues of interest). Since only three TE images are acquired it is difficult to correct for partial volume effects. The method is also more susceptible to field inhomogeneities compared to FSE method.

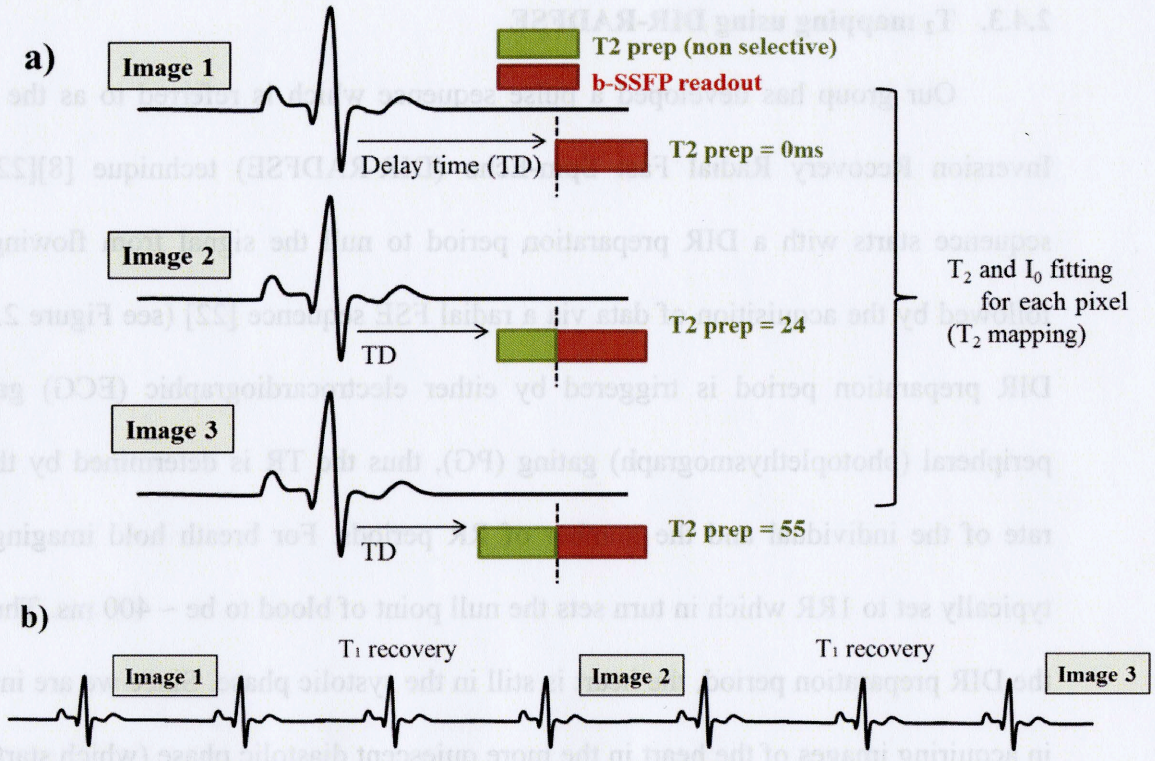

Figure 2.4. T_2 prepared-SSFP.

2.4.3. T_2 mapping using DIR-RADFSE

Our group has developed a pulse sequence which is referred to as the Double Inversion Recovery Radial Fast Spin-Echo (DIR-RADFSE) technique [8][22]. This sequence starts with a DIR preparation period to null the signal from flowing blood followed by the acquisition of data via a radial FSE sequence [22] (see Figure 2.5). The DIR preparation period is triggered by either electrocardiographic (ECG) gating or peripheral (photoplethysmograph) gating (PG), thus the TR is determined by the heart rate of the individual and the number of RR periods. For breath hold imaging TR is typically set to 1RR which in turn sets the null point of blood to be ~ 400 ms. Thus, after the DIR preparation period, the heart is still in the systolic phase. Since we are interested in acquiring images of the heart in the more quiescent diastolic phase (which starts ~ 600 ms after the QRS signal), we need an additional 200 ms delay before the FSE acquisition begins. There is a natural ~200 ms delay for blood to flow from the heart to the tip of the finger so PG is better suited for the experiment, as shown in Figure 2.5. Moreover, PG is often advantageous for MRI triggering compared to ECG gating because the ECG signal is more often lost due to poor conductance in the skin or interferences with the imaging gradients.

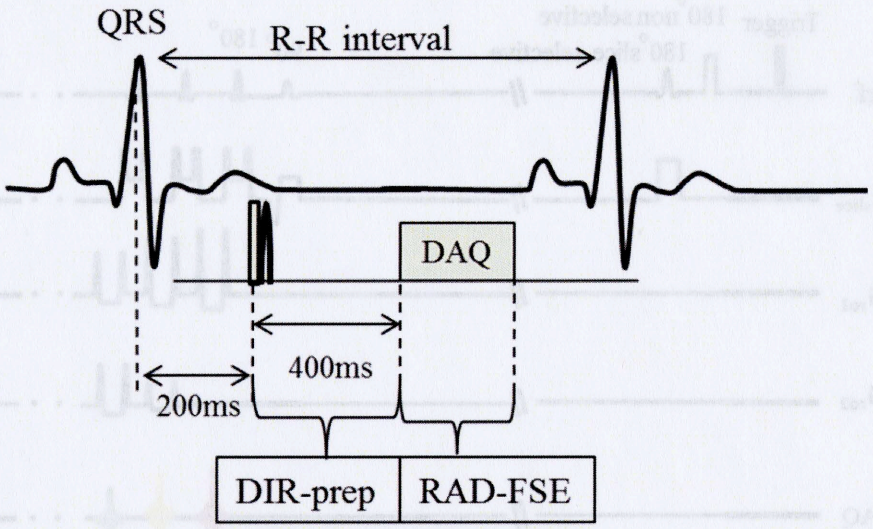

Figure 2.5. DIR-RADFSE data acquisition.

As shown in Figure 2.6, on each TR period we acquired data for 16 different radial lines (ETL=16). This is repeated for 12-16 times (12-16 TRs). Each radial line of data is collected with 256 readout points, thus, the size of the acquisition matrix is 256×192 or 256×256. An eight channel receiver coil (GE 8-channel cardiac array) is used to acquire data from 8 receivers simultaneously. Dummy scans are performed to stabilize the spin system before the data is collected for the duration of 6 TRs. The dummy scans and DIR-RADFSE data acquisition take total scan time of about 22 seconds for a heart rate of 60 bpm.

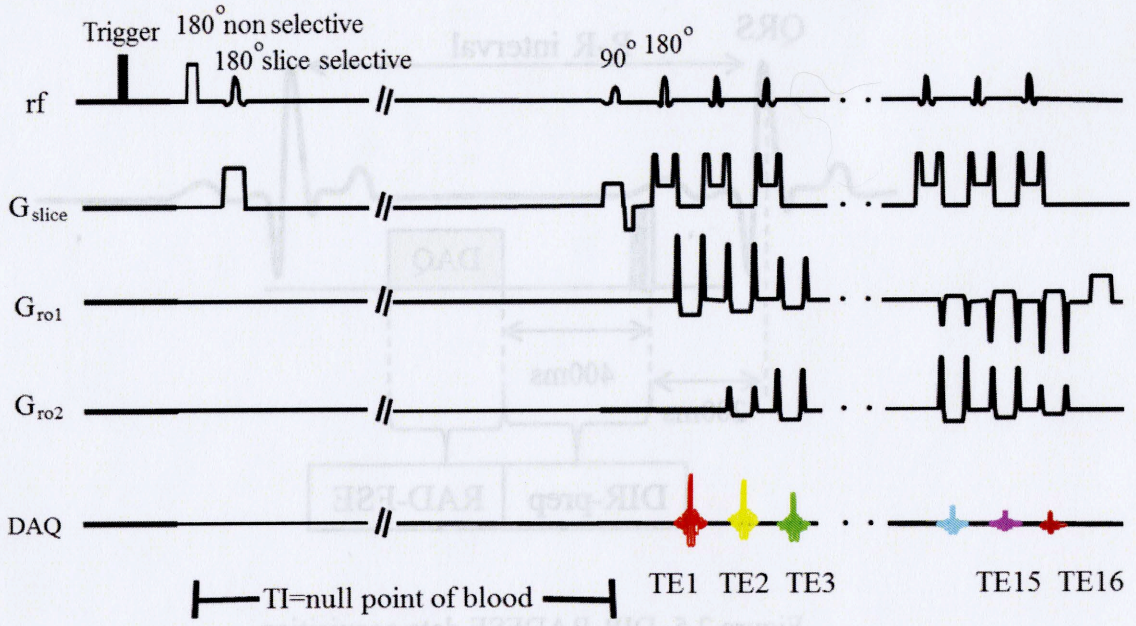

Figure 2.6. DIR-RADFSE pulse sequence.

An advantage of the DIR-RADFSE technique is that, as mentioned in Chapter 1, a radial k-space trajectory minimizes the effects of motion. Additionally a single k-space data set acquired with DIR-RADFSE can produce not only an anatomical image, but also multiple TE images and a T_2 map after post-processing the data as will be described below.

2.4.4. Reconstruction algorithms for T_2 mapping using DIR-RADFSE

Because in radial acquisitions each radial line goes though the center of k-space, a single RADFSE k-space data set can be divided into partial data sets from which images at different TEs (number of TEs=ETL) can be reconstructed. If the entire k-space data has 256 radial lines and ETL=16 each TE data set will only have 16 radial lines. For a data set collected with 256 points along each radial line, each partial TE data set will only be well sampled up to a radius of 10 points (i.e., the Nyquist radius as defined in Chapter 1) but undersampled past the Nyquist radius. In order to overcome problems associated with undersampling, post processing methods have been developed to reconstruct TE images and generate a T_2 map. The (1) echo sharing (ES) [9] and (2) model-based (MB) [10] [11] algorithms are discussed below.

1) Echo sharing (ES) algorithm

The ES algorithm [9] is based on the observation that the low frequency region of k-space (region at the center of the k-space) has the majority of the signal energy and has contrast information between tissues, such as T_2 information. The high frequency region (which is undersampled in the TE images as described above) has information of fine structures such as tissue boundaries but less on the bulk contrast of images. By using data at a specific TE in the central part of k-space and data at other TEs in the outer part of k-space, it is possible to maintain the desired contrast in the images while minimizing artifacts due to undersampling.

A schematic representation of the ES algorithm is shown in Figure 2.7, for ETL = 4. Up to the first Nyquist radius, data from one TE (e.g. TE_1) is placed in the central part of k-space to reconstruct an image with a bulk contrast equal to TE_1 ($TE_{eff} = TE_1$). Past the first Nyquist radius k-space is filled with data from neighboring TEs (i.e. TE_2) up to the second Nyquist radius (determined from the combined TE data sets). The process of mixing the TE data sets is continued in successive tiers until the entire TE data sets are used. This method is repeated for each TE. The k-space data sets are then reconstructed to obtain images at different TEs from which a T_2 map is computed.

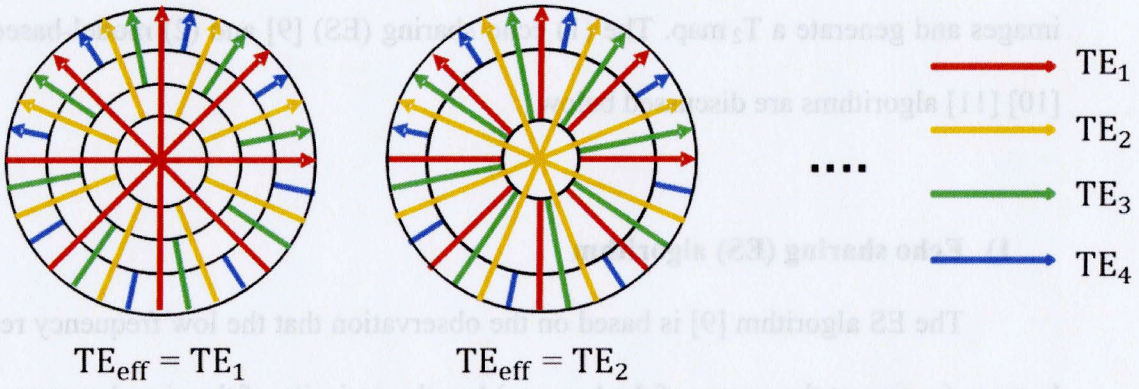

Figure 2.7. Diagram of echo-sharing in k-space. For simplicity and ETL = 4 is used in this example.

2) Model-based (MB) algorithm/REPCOM

As an alternative to the ES approach, MB algorithms [10] [11] were developed to reconstruct TE images without mixing TE data sets. In the MB algorithms, parameters are estimated iteratively by fitting the acquired k-space data to a model describing the signal decay; for the case of T_2 estimation, the signal model is assumed to be a mono-exponential decay. The goal is to minimize the difference between the acquired k-space data and the signal model. The data consistency term that describes this difference is:

$$\sum_n \left\| FT_n(\boldsymbol{I_0} e^{-TE_n/\boldsymbol{T_2}}) - \boldsymbol{K}_n \right\|^2 . \quad (2.4)$$

where FT_n denotes the Fourier transform of the signal model for all k-space locations during n^{th} SE period, and $\mathbf{K_n}$ denotes the measured k-space data at TE_n.

Based on a priori knowledge of the object, penalty terms can be added to Equation 2.4. With the penalty functions, P_n, and the corresponding regularization parameters, λ_n, Equation 2.4 becomes:

$$\widehat{\boldsymbol{I_0}}, \widehat{\boldsymbol{T_2}} = argmin_{\boldsymbol{I_0},\boldsymbol{T_2}} \{ \sum_n \left\| FT_n(\boldsymbol{I_0} e^{-TE_n/\boldsymbol{T_2}}) - \boldsymbol{K}_n \right\|^2 + \sum_n \lambda_n P_n(\boldsymbol{I_0}, \boldsymbol{T_2}) \} . \quad (2.5)$$

The non-linear exponential decay model causes scale mismatch between I_0 and T_2 [10]. To solve this problem, a scaling factor (sf) is introduced to the exponential term in Equation 2.5:

$$\widehat{\boldsymbol{I_0}}, \widehat{\boldsymbol{T_2}} = argmin_{\boldsymbol{I_0},\boldsymbol{T_2}} \{ \sum_n \left\| FT_n(\boldsymbol{I_0} e^{-sf \cdot TE_n/\boldsymbol{T_2}}) - \boldsymbol{K}_n \right\|^2 + \sum_n \lambda_n P_n(\boldsymbol{I_0}, \boldsymbol{T_2}) \} . \quad (2.5)$$

The MB algorithm takes advantage of the fact that the angular orientation of the radial lines is different in the TE data sets to overcome to some extent the lack of information in the high spatial frequencies on each set. The disadvantage of the MB

algorithm is that the performance is dependent on the sf. The novel algorithm recently developed by Huang, et al. called REPCOM (Reconstruction of principal component coefficient maps using compressed sensing) [11] addresses the issues associated with the nonlinearity of the exponential term in MB reconstructions. It also addresses the issues related to errors in the T_2 estimation of small objects and edges. The latter have high spatial frequency content, thus the mixing of TE in the high spatial frequencies, as in the ES algorithm, introduces reconstruction errors which affect T_2 estimation.

REPCOM is a principal component analysis (PCA)-based algorithm where the exponential term in the T_2 decay signal model is approximated by a linear combination of a few principal components (PCs). The PCs are generated from a training set of exponential decay curves with a range of T_2 and TE values using the singular value decomposition (SVD) algorithm [12]. The detailed calculations can be found in Huang, et al., MRM, 2012 [11].

Because REPCOM has been shown to yield more accurate T_2 estimates in small objects and for edges, the algorithm may be more suitable for CMR applications. In CMR, one of the difficulties comes from the morphology of the heart. For example, the features of sharp edges are present around the myocardium (both endo- and epi- cardium), infarct scars are typically thin and localized, and regions of edema can be small within the myocardium.

Chapter 3

IMPLEMENTING DIR-RADFSE FOR T_2 MAPPING OF THE HEART

3.1. Introduction

In this chapter, the steps that I took to optimize the DIR-RADFSE method for T_2 mapping in patients are described. The data shown in the experiments in this chapter were acquired on normal controls with DIR-RADFSE. The imaging studies were performed according to the regulations of the Internal Review Board at the University of Arizona.

3.2. DIR-RADFSE and non-axial FOVs

In routine CMR examinations, instead of the axial (AX) slice, the oblique short-axis (SA) view is typically used for the evaluation of the myocardium. In this view the slice orientation is chosen to be perpendicular to the long axis of the heart. In the MRI scanner the SA view is achieved by first running a scout of the patient's thoracic cavity to get a rough idea of the location and orientation of the heart; subsequent scans are then used to obtain the SA view. Figure 3.1 shows an example of the images used to prescribe a SA slice. Figure 3.1(a) is a sagittal scout, an orientation which is close to a 2-chamber view of the heart. This image is used to plan a 4-chamber view of the heart by prescribing a slice that bisects the mitral valve and apex, as shown by the yellow line. The initial sagittal scout is typically obtained with an ungated spoiled gradient echo (SPGR) sequence; the 4-chamber view image is typically obtained with a gated steady-state free

precession (SSFP) sequence (Figure 3.1(b)). The SA slices are planned from the 4-chamber view by orienting the slice perpendicular to the septum as shown by the red line in Figure 3.1(b). In this example the SA slice was acquired with the DIR-RADFSE sequence, which gives the image shown in Figure 3.1(c). If one does not get a true 4-chamber view from the prescription in step 1, the image obtained in step 2 is used to prescribe a 2-chamber view by bisecting the LV from the mitral valve to the apex. The 2-chamber view is then used to prescribe the 4-chamber view from which a SA view is planned. This step may need to be repeated until a true 4-chamber view is obtained.

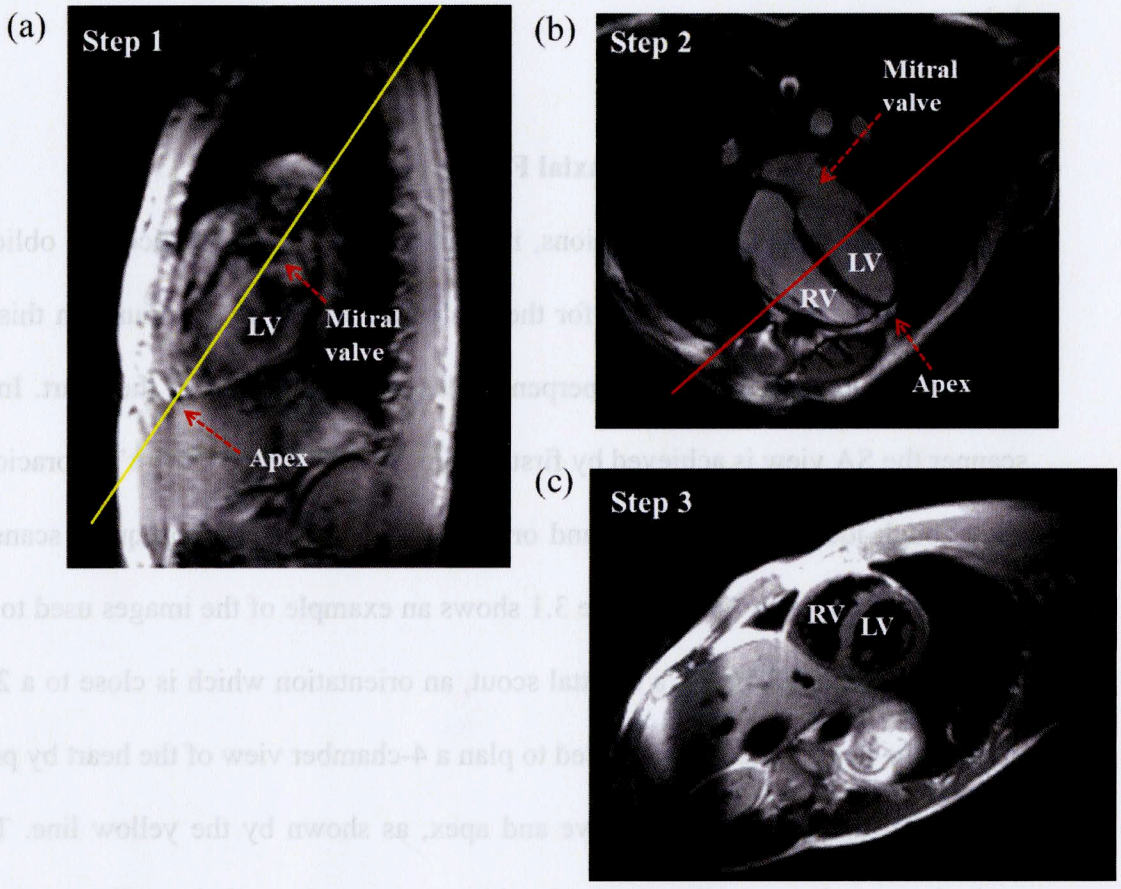

Figure 3.1. Steps to get a short axis slice; (a) Sagittal scout approximating a 2-chamber view obtained with SPGR (b) 4-chamber view obtained with SSFP, (c) the SA view acquired with DIR-RADFSE.

In the SA orientation, even the maximum FOV (in the scanner used in this work the maximum FOV=48 cm) is not large enough to cover the anatomy for most patients. This means that the Nyquist criterion to avoid aliasing is not satisfied. Any object outside the FOV will be a source of artifact, which in radial trajectories will manifest as streaks in the image as shown in Figure 3.2, where the FOV was set to 39 cm. In addition, anatomy inside the FOV can also cause artifacts. For example, fluid-rich areas or areas prone to motion can cause streaks that ran across the heart.

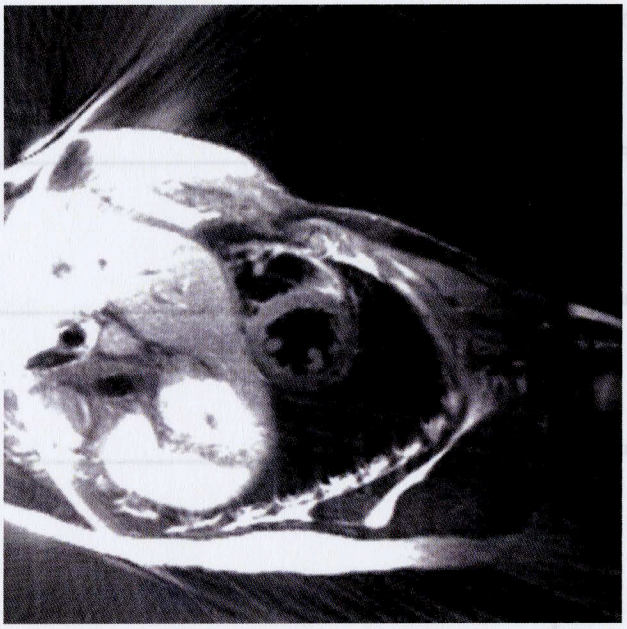

Figure 3.2. Streaks from outside FOV.

3.3. Placement of saturation bands

In order to minimize artifacts coming from anatomy outside and inside the FOV, saturation bands (SATs) can be used. SATs are obtained by exciting a specific area of tissue (a rectangular band) into the transverse plane by using a slice selective 90°

excitation pulse and then dephasing the signal using strong (spoiler) gradients. SATs are placed right before the excitation of the slice to be observed so that the signal remains dephased at the time of data acquisition. In the DIR-RADFSE pulse sequence SATs are placed during the DIR preparation period (Figure 3.3), so there is no increase in imaging time. Figure 3.3 shows a pulse sequence diagram, drawn using the GE simulation software (WTools), where four SATs were prescribed as an example. For the effective suppression of the anatomy in SA acquisitions one can place several SATs (4-6) to cover regions of unwanted signal (see below).

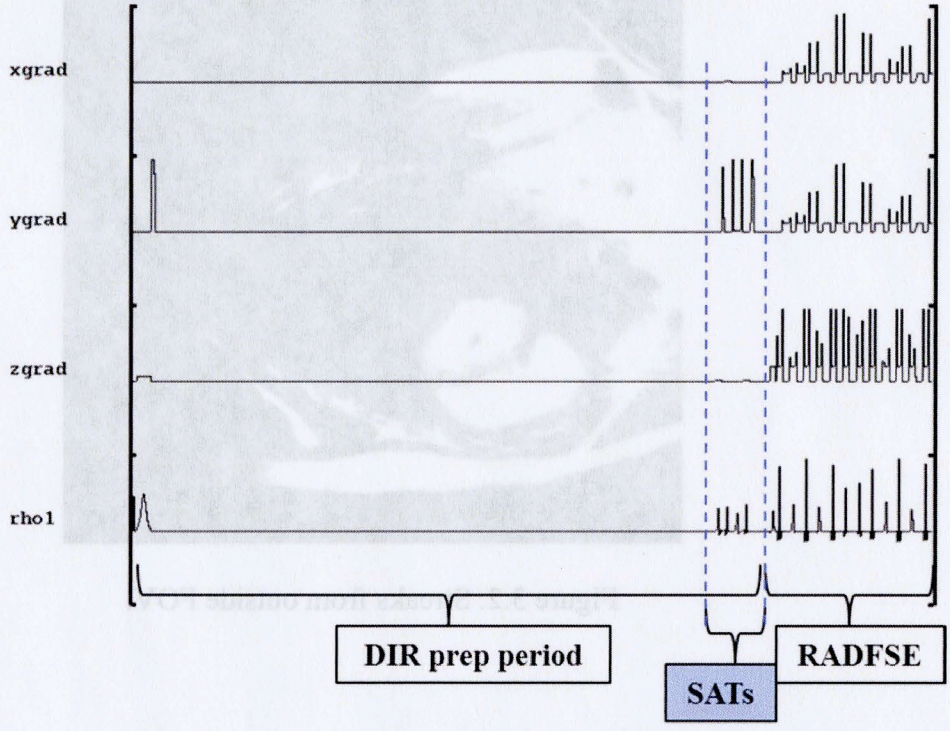

Figure 3.3. Placement of SATs during the DIR prep period.

An example of the effect of SATs is shown in Figure 3.4 on a normal volunteer. Data were acquired with DIR-RADFSE using an eight channel receiver coil on a mid LV

SA slice with FOV = 40 cm and slice thickness = 8 mm. Other imaging parameters were: ETL=16, TR=1RR, receiver bandwidth (RBW) = ±32 kHz, acquisition matrix = 256 (readout points) × 256 (views). Figure 3.4 (a) shows the SAT (5 cm thick) on the abdomen; (b) shows the resulting image where signal suppression can be seen in the region where a SAT was placed (arrow). The thickness of the SATs can be changed; the default is set to 4 cm. Note that with one SAT the streaks are still visible. Figure 3.4 (d) shows an image acquired with two SATs (4 cm thick) placed inside and on the edge of the FOV as shown in Figure 3.4 (c). Figure 3.4 (f) shows an image with three SATs (4 cm thick) placed as shown in Figure 3.4 (e).

This preliminary experiment indicated that streaks can be reduced by placing two or more SATs (4 cm thick) on the abdomen, covering inside and outside the FOV. In the experiments shown in the following sections, we used a combination of SATs with the standard thickness of 4cm.

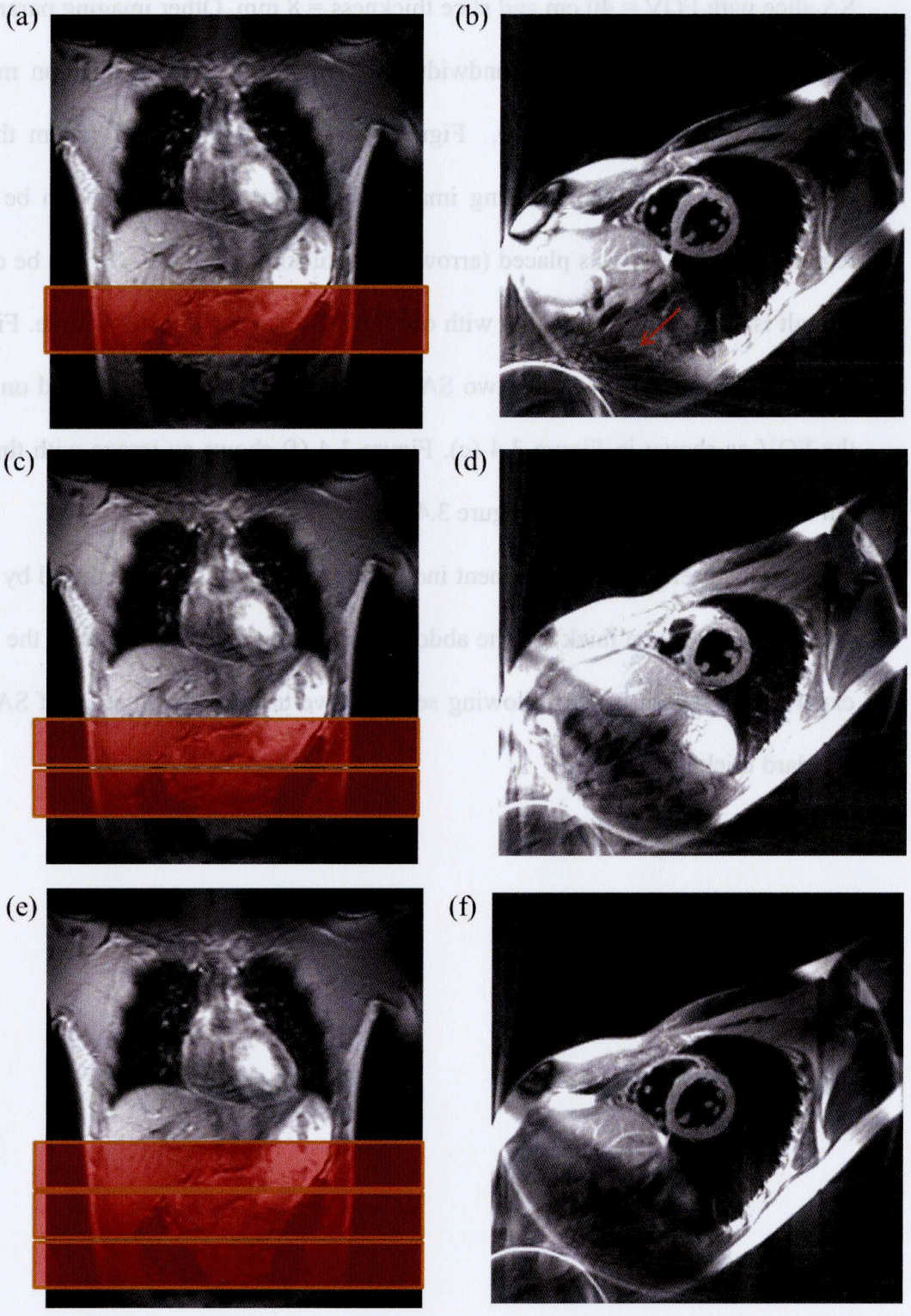

Figure 3.4. Effect of SATs on streaking artifacts.

3.4. Using an RF shield blanket

To further avoid streaking artifacts caused by the anatomy outside the heart area, we tested the effectiveness of using an RF shield blanket (MRI M-07 Breast Shield 36 × 86cm by MWT Materials, Inc., now called Accusorb MRI® from Millimeter Wave Technologies) with and without SATs. For this experiment, we used a phantom in the shape of a rectangular prism filled with doped water. The data were acquired using an eight channel receiver coil with the RADFSE pulse sequence (the DIR blood suppression period and the triggering were not used for the phantom) with parameters: FOV = 48 cm, TR = 1000 ms, slice thickness = 8 mm, ETL = 16, RBW = ±31.25 kHz, and acquisition matrix = 256 × 256.

Figure 3.5 shows images of the phantom with (a) no SATs, (b) two SATs inside the FOV on the right end of the phantom, (c) the blanket on the right end of the phantom (dotted line as an approximate reference for the placement of the blanket), and (d) the blanket and SATs (the same SATs as shown in b). The blanket was wrapped around the phantom, covering the entire portion indicated.

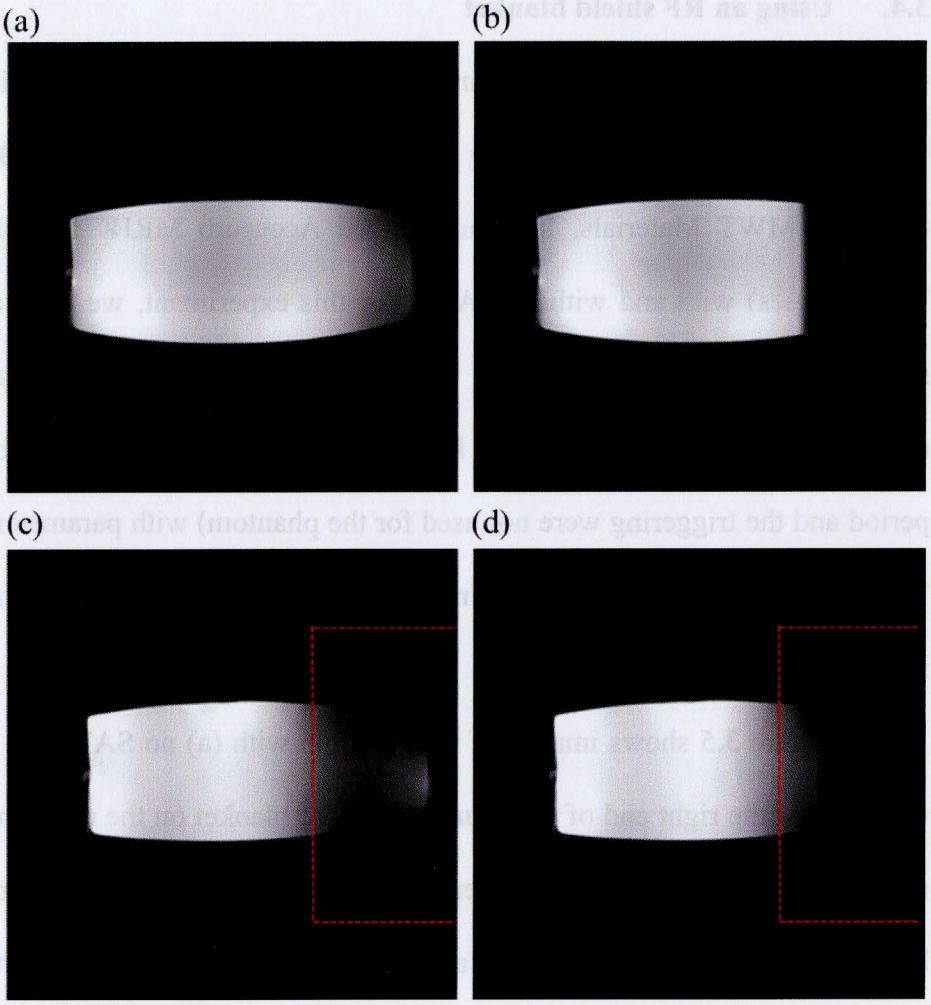

Figure 3.5. Phantom experiment with SATs and the RF shield blanket (a) with no blanket, (b) with no blanket and with two SATs inside the FOV, (c) with blanket, and (d) with blanket and same SATs as in (b).

To quantitatively analyze the results three ROIs were defined, as shown in Figure 3.6, and the SNR was calculated for regions 1 and 2. The mean signal in regions 1 (S1) and 2 (S2) were divided by the standard deviation of the signal in region 3 (SD3). The results are shown as SNR1 and SNR2 in Table 3.1. Furthermore, the contrast to noise ratio (CNR = SNR1 – SNR2) and the percent change in SNR (CNR/SNR1) were

calculated. The results showed that CNR and the % change in SNR were greater when both SATs and the blanket were used (Panel d).

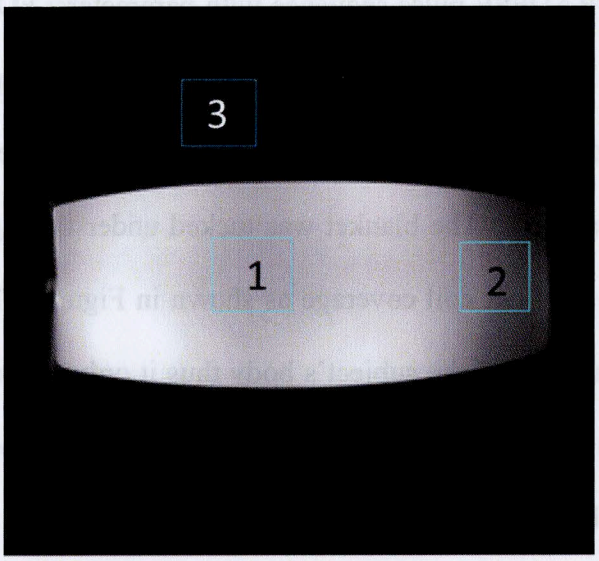

Figure 3.6. ROIs for the SNR calculation.

Table 3.1. Effect of using an RF blanket and/or SAT bands in the SNR of regions 1 and 2 of the phantom shown in Figure 3.6. The calculations were done using the images shown in Figure 3.5.

SNR for different panels in Figure 26	Panel (a)	Panel (b) 2 SATs	Panel (c) blanket	Panel (d) 2SATs + blanket
SNR1	161.70	154.32	167.83	168.10
SNR2	103.19	20.81	47.40	15.55
CNR (SNR1-SNR2)	58.51	133.51	120.43	152.55
% change in SNR CNR/SNR1	36.18	86.52	71.76	90.75

Based on this finding, an experiment was conducted on a human volunteer using the DIR-RADFSE method. The data were acquired with the eight channel receiver coil with the DIR-RADFSE pulse sequence with parameters: FOV = 40 cm, TR = 1RR, slice thickness = 8 mm, ETL = 16, RBW = ±31.25 kHz, and acquisition matrix = 256 × 256. Figure 3.7 shows an example of the setup where the blanket is placed on the abdominal region of the subject. The blanket was tucked under the eight channel receiver coil (~5 cm within the receiver coil coverage as shown in Figure 3.7). The blanket was not wide enough to wrap around the subject's body thus it only covered the front and the sides of the subject. In the experiment, the number and the location of SATs used were also tested to determine the optimal setup.

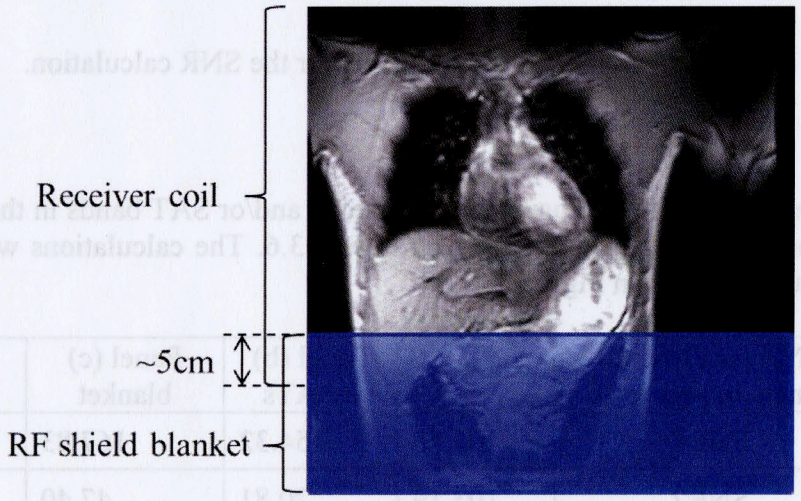

Figure 3.7. RF shield blanket placed on the lower abdomen.

Figure 3.8 shows the resulting images. Initially, only the blanket was used on the lower abdomen (a). Although the blanket alone helped in removing major streaks, better results were obtained by adding SATs. Figure 3.8 shows images with the blanket and (b)

one SAT inside the FOV on the abdomen, or (c) two SATs on the abdomen (one on the edge of the FOV); the placement of the SATs was similar to the examples shown in Figure 3.4.

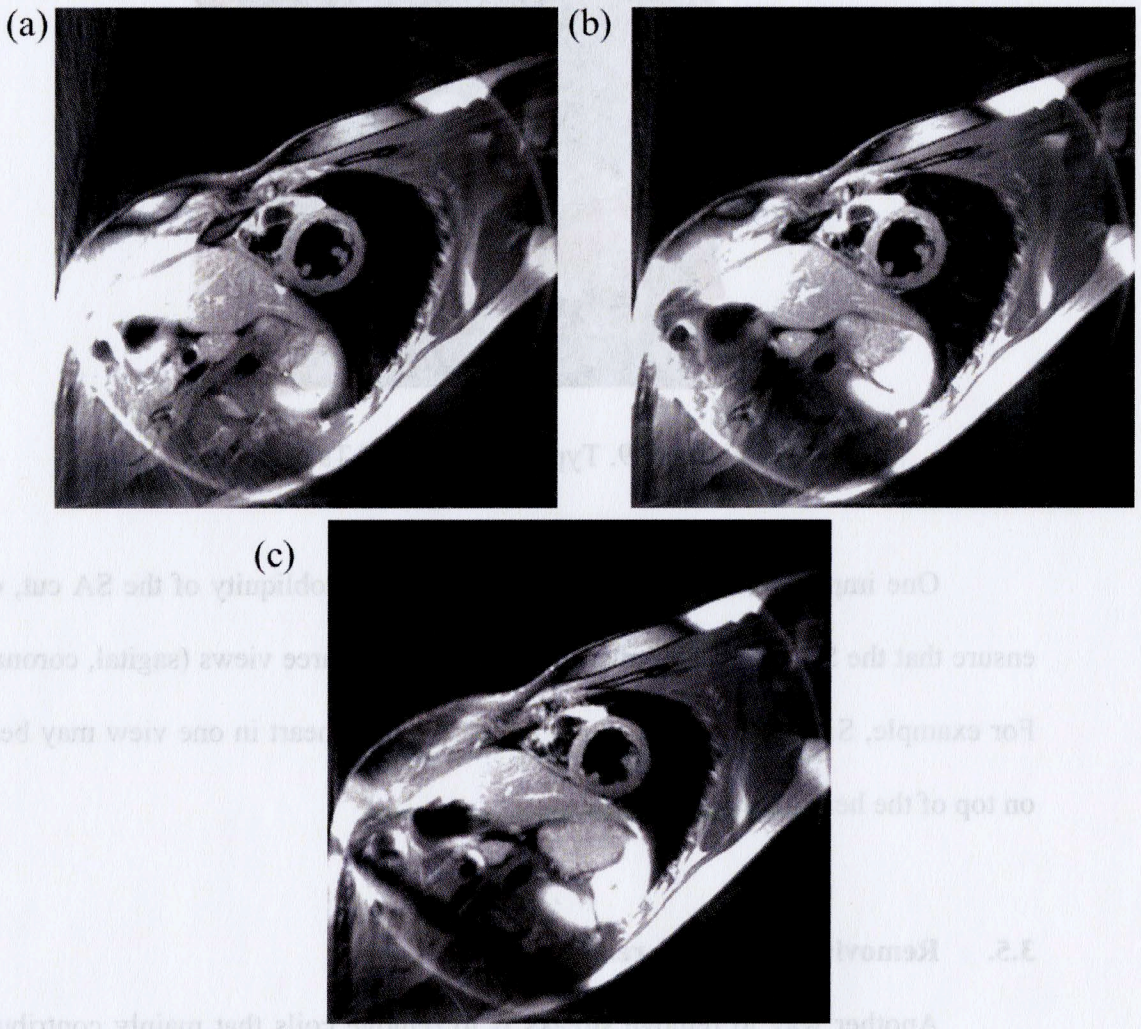

Figure 3.8. Reduction of streaking artifacts by using RF shield blanket and SATs.

The images were acquired with a FOV equal to or smaller than 40 cm in the subjects. We ultimately changed the FOV to the maximum value, 48 cm, for all subjects to further reduce streaking artifacts from outside the FOV. Also we decided to add SATs

on both arms to suppress any aliasing from the extremities.. An example coronal scout showing the typical SATs placement we now use is shown in Figure 3.9.

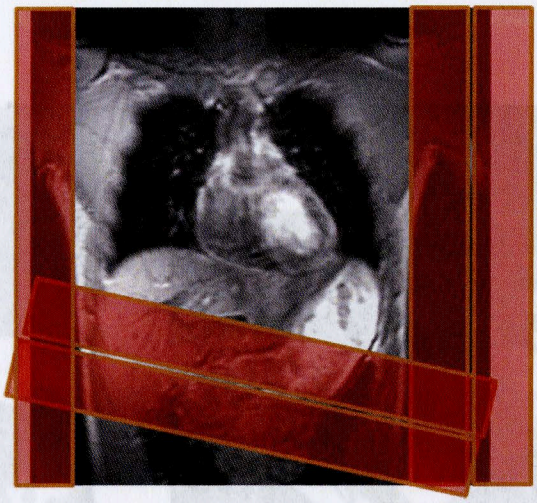

Figure 3.9. Typical graphic SATs placement.

One important consideration is that due to the obliquity of the SA cut, one must ensure that the SAT bands are placed correctly in all three views (sagital, coronal, axial). For example, SAT bands that are not overlaid on the heart in one view may be overlaid on top of the heart in a different view.

3.5. Removing streaks by removing coils

Another way to remove streaks is to remove coils that mainly contribute to the streaking artifact. Figure 3.10 (a) shows an image where the streaking artifact was not ameliorated by the use of SATs and the RF shield blanket. To determine the source of the streaks, I reconstructed images separately coil by coil. On this particular data set, one of the eight coils gave bright streaks (the brightest of these was seen along the X axis)

across the heart as shown in Figure 3.10 (b). Figure 3.10 (c) shows the location of each coil with respect to the body (the anterior and the posterior coils are shifted to the left/right with respect to the body for demonstration purposes). The streaks came from coil #1 which is on the lower right abdominal wall (the heart is being covered mainly by coil #4). After removing coil #1 from the reconstruction, the streaks were significantly reduced (Figure 3.10 (d)). This method worked well in this case because the coil removed was not contributing much signal to the heart.

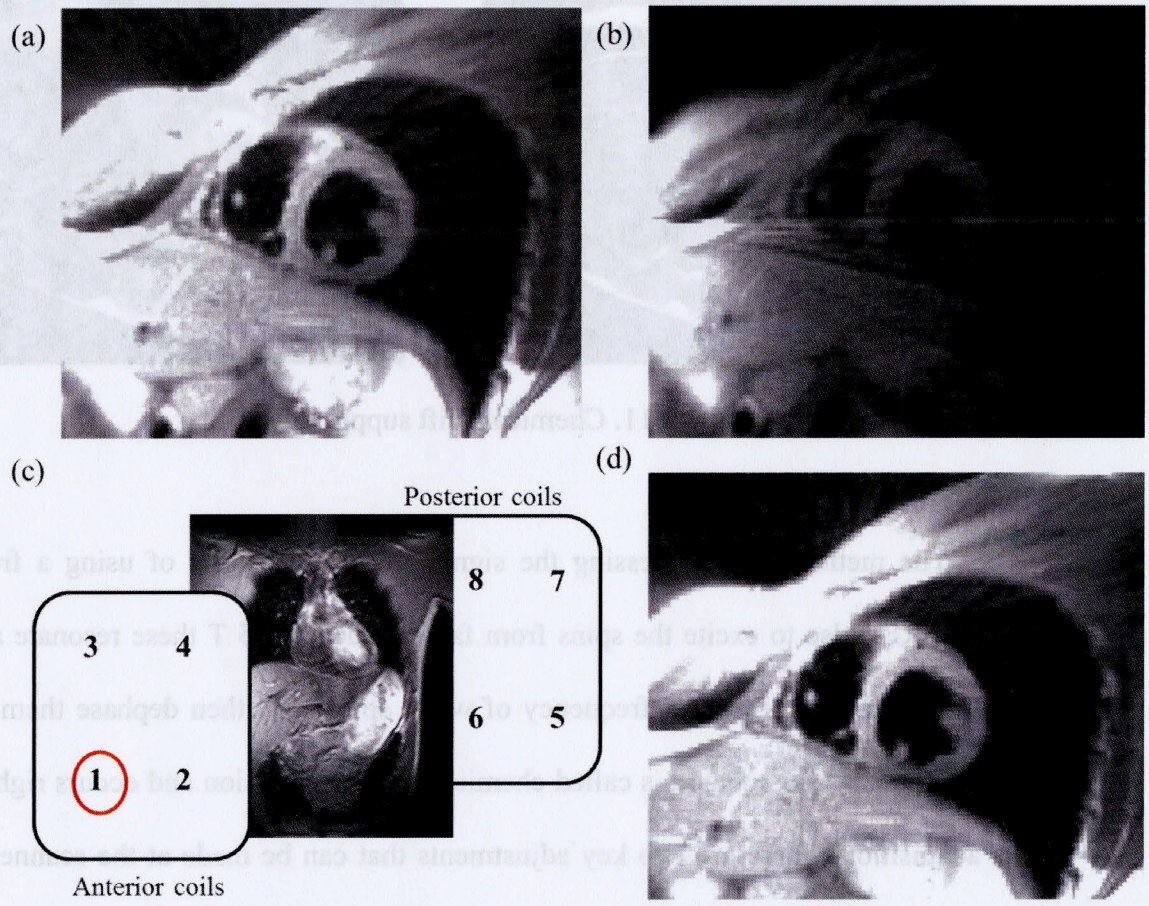

Figure 3.10. Image reconstruction without coil #1 to remove streaks.

3.6. Chemical shift suppression

One of the problems we encountered during data acquisition on human subjects was related to the suppression of subcutaneous fat signal. Subcutaneous fat causes off-resonance artifacts which in radially acquired data manifest as a tuning-fork artifact and general bluriness in the images. A example of an image acquired with DIR-RADFSE where fat is not well suppressed is shown in Figure 3.11 (a).

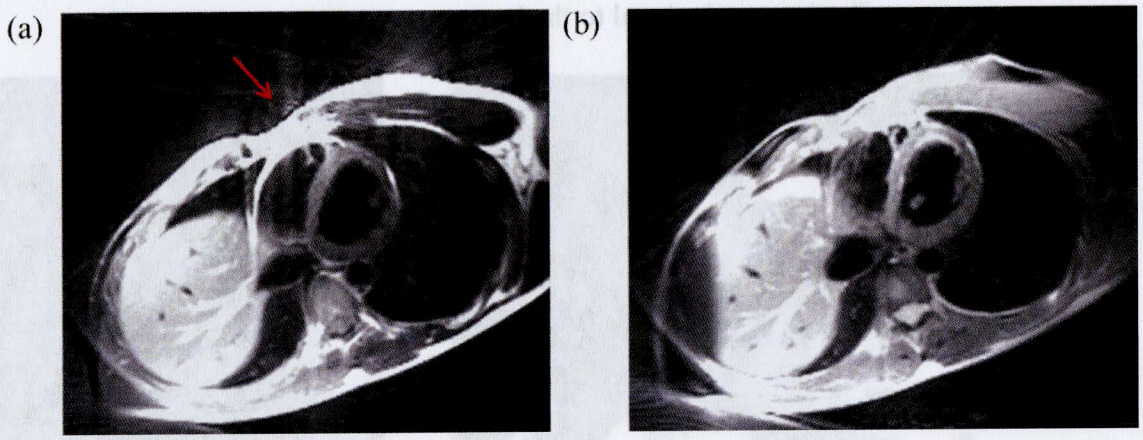

Figure 3.11. Chemical shift suppression on fat.

The method for suppressing the signal from fat consists of using a frequency selective RF pulse to excite the spins from fatty tissue (at 1.5 T these resonate at ~ 220 Hz upfield from the resonant frequency of water spins) and then dephase them using a spoiler gradient. The method is called chemical shift suppression and occurs right before data acquisition. There are two key adjustments that can be made at the scanner during the pre-scan for improving fat suppression. One is to adjust the power of the RF excitation (which in turns controls the flip angle (FA) of the excitation); another one is to adjust the frequency of the excitation. With these adjustments fat suppression can be

improved on a case by case basis. This is shown in Figure 3.11 (b), where the power and the excitaion frequency of the chemical shift selective pulse were adjusted during the pre-scan. Note that the signal from fat around the heart is better suppressed and the tuning-fork artifact as well as the general bluriness in the image is reduced.

The adjustments to improve fat suppression, however, do not work on every subject. Figure 3.12 shows an image of an obese subject where adjustments were made to improve fat suppression. Note that although fat around the heart is relatively well suppressed there are other areas in the FOV where the signal from fat is not suppressed (arrows) leading to an overall bluriness in the image.

Fat suppression can be improved using phase-based chemical shift methods [19][20][21], which is a future extension of the technique as will be discussed in Chapter 5. SATs can also be used to supress the signal from fatty areas that are away from the heart.

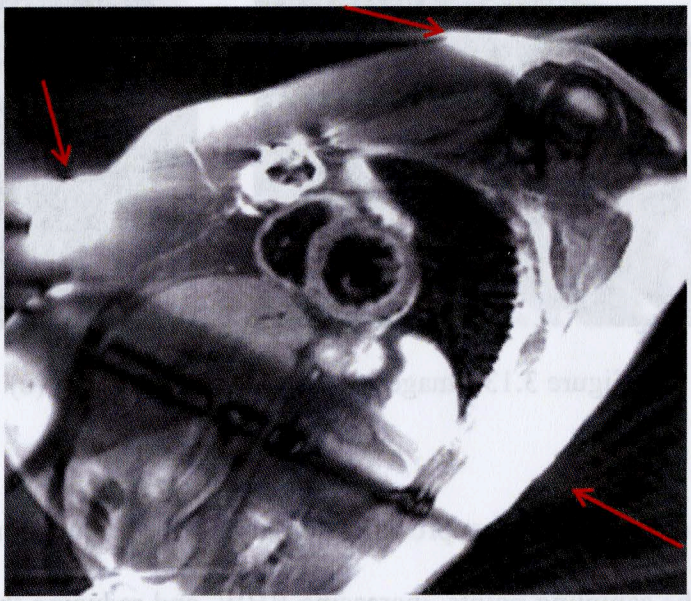

Figure 3.12. Image artifacts due to the unsuppressed signal from fat.

3.7. Imaging with faster heart rates

In cardiac patients, it is common to see high heart rates (85 – 95 bpm). A problem associated with faster heart rates in CMR is that the diastolic period is shorter. Since the acquisition of each echo train of data in the DIR-RADFSE sequence takes place over a window of 128 ms (for the acquisition parameters of ETL=16, receiver bandwidth = ± 32 kHz, and number of readout points = 256), the heart may start contracting during data acquisition causing motion artifacts. An example image from a patient with a HR > 87 bpm is shown in Figure 3.13 (b) compared with a control with a normal HR (average HR = 64 bpm) (a). The image with the faster HR has a blurry and grainy appearance and the heart is contracted compared to (a).

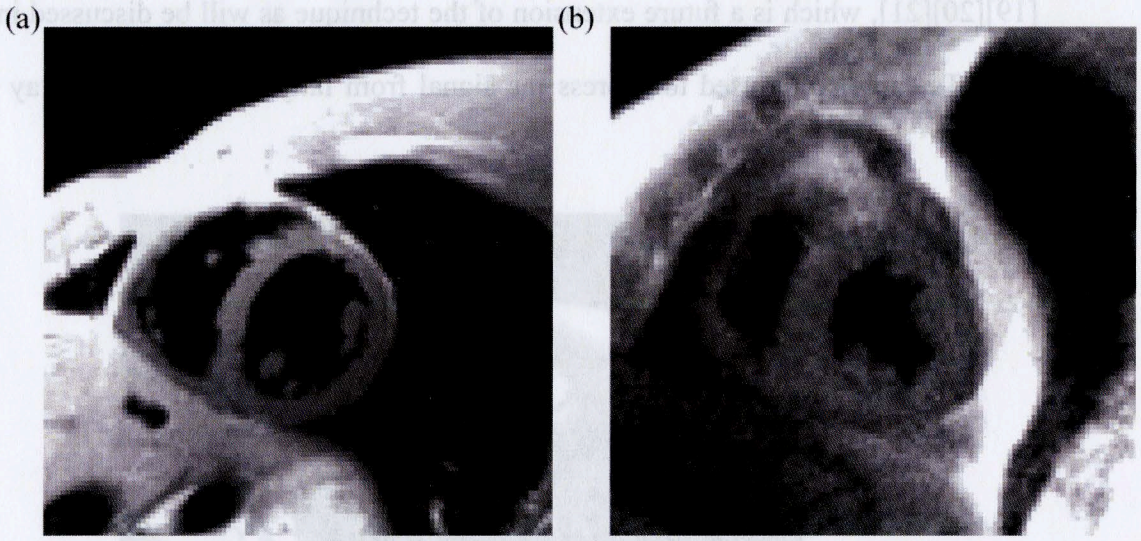

Figure 3.13. Images with (a) normal HR, and (b) faster HR.

There are several approaches to shorten the acquisition time. Among them are reducing the sampling points, increasing RBW, and reducing the width of the refocusing

RF pulses (RRFs). Reducing the sampling points will compromise the image resolution, however. The other two approaches are investigated in the next subsections.

3.7.1. Increase the RBW

In the previous experiments, a RBW = ± 32 kHz was used. If we increase the RBW, the data readout period will be shorter. For example with 256 readout points, if we double the RBW to ± 62.5 kHz, the sampling time will be 2 ms, whereas for a RBW = ± 32 kHz the sampling time is 4 ms. The effect of increasing the RBW is shown in Figure 3.14. Note that in Figure 3.14 (a), where data were acquired with a RBW = ± 32 kHz, the region of the LV closer to the lungs (arrow) has less signal intensity (SI) than the septum; this is a typical artifact caused by cardiac motion. With a RBW = ± 62.5 kHz, the SI through the LV is more uniform. The downside of using a higher RBW is that the SNR is lower. Images in Figure 3.14 were acquired in a control with HR <70 bpm. The effect of RBW increase may be more dramatic for patients with HR > 85 bpm.

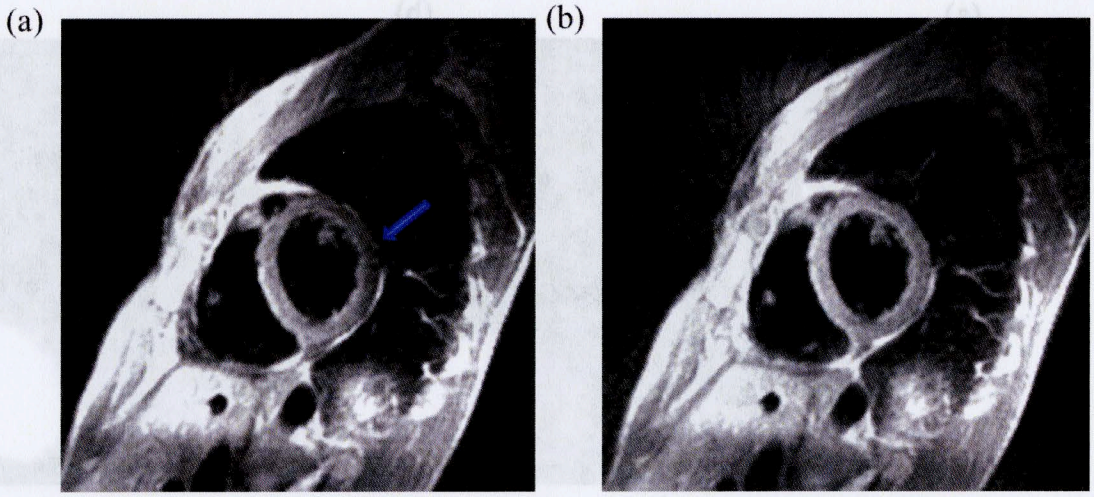

Figure 3.14. Images with RBW = (a) ± 32 kHz, and (b) ± 62.5 kHz.

3.7.2. Decrease in RF pulse length

A second approach to reduce the acquisition time is by decreasing the RRF length. In the DIR-FSE method provided by the scanner's manufacturer, the shape of the RRF is a single lobe sinc with a pulse length of 1.2 ms. This is shorter than the regular RRF which is a three-lobe sinc with a pulse length of 3.2 ms. When the RRF length is decreased, the crusher gradients placed before and after a readout gradient are also shortened because less energy is needed to spoil unwanted spins. The total time for both of the crusher gradients is shortened by ~0.7 ms per readout. Thus the acquisition window of the echo train is shortened by ~43.2 ms for an ETL=16. The disadvantage is that the maximum FA attained by the single lobe sinc is only 155° (see below). Images of a subject with a heart rate > 85 bpm acquired with the three-lobe and single-lobe sinc RRF pulses with RBW = ± 32kHz are shown in Figure 3.15. Figure 3.15 (a) shows the decreased SI in the LV due to the heart starting to contract during data acquisition. With the reduced RRF (b), the signal drop in the LV is not seen.

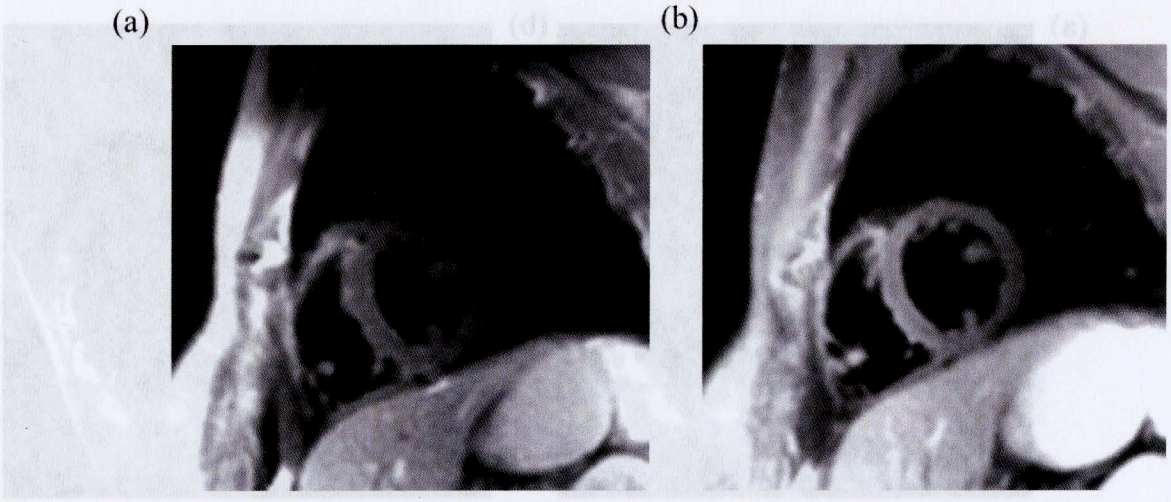

Figure 3.15. Images with refocusing flip angle = (a) 180°, and (b) 155°.

3.8. Problems with refocusing RF pulse with flip angle < 180°

Because T_2 mapping is the main reason for using the DIR-RADFSE method it is important to discuss the problems associated with RRF pulses with FA < 180°. These problems result from using truncated RF waveforms (as explained above) and from non-rectangular slice profiles. In these cases all or some of the spins within the refocusing slice will experience FA less than 180° which will lead to the generation of indirect echoes. These echoes behave differently than the SEs causing the signal to deviate from the exponential model. In order to reduce the indirect echo effect, a technique proposed by Pell, et al. [15] was incorporated into the DIR-RADFSE as a control variable (CV) by a member of the group. The technique involves widening the slice thickness corresponding to the RRF pulses compared to the slice thickness of the 90° excitation such that the slice profile affecting the excited spins approximates better a rectangular profile. Pell et al showed that the optimal refocusing slice thickness was three times wider than the initial excitation RF. Increasing the slice thickness reduces the efficiency in multi-slice experiments since a wider gap between slices is needed. Since the DIR-RADFSE sequence is a single slice experiment (a restriction imposed by the DIR preparation period) there is no loss in time efficiency due to the thick slice approach.

Figure 3.16 shows plots of the signal decay from the data acquired on two phantoms with known T_2 values: 219.1 ms (a,b) and 79.7 ms (c,d). Figure 3.16 (a) and (c) were acquired with the standard refocusing slice thickness (the same as the excitation slice thickness), and (b) and (d) with three times thicker refocusing slice. The blue symbols represent data acquired and the red dotted curves are the fitted T_2 decay curves.

The results showed that indirect echoes are visible; e.g., the second TE point shows higher SI than the first and in general the SI deviates from the fitted curve in Figures 3.16 (a) and (c). With the three times thicker refocusing slice, the data fit to a single exponential T_2 decay curve well as shown in Figures 3.16 (b) and (d).

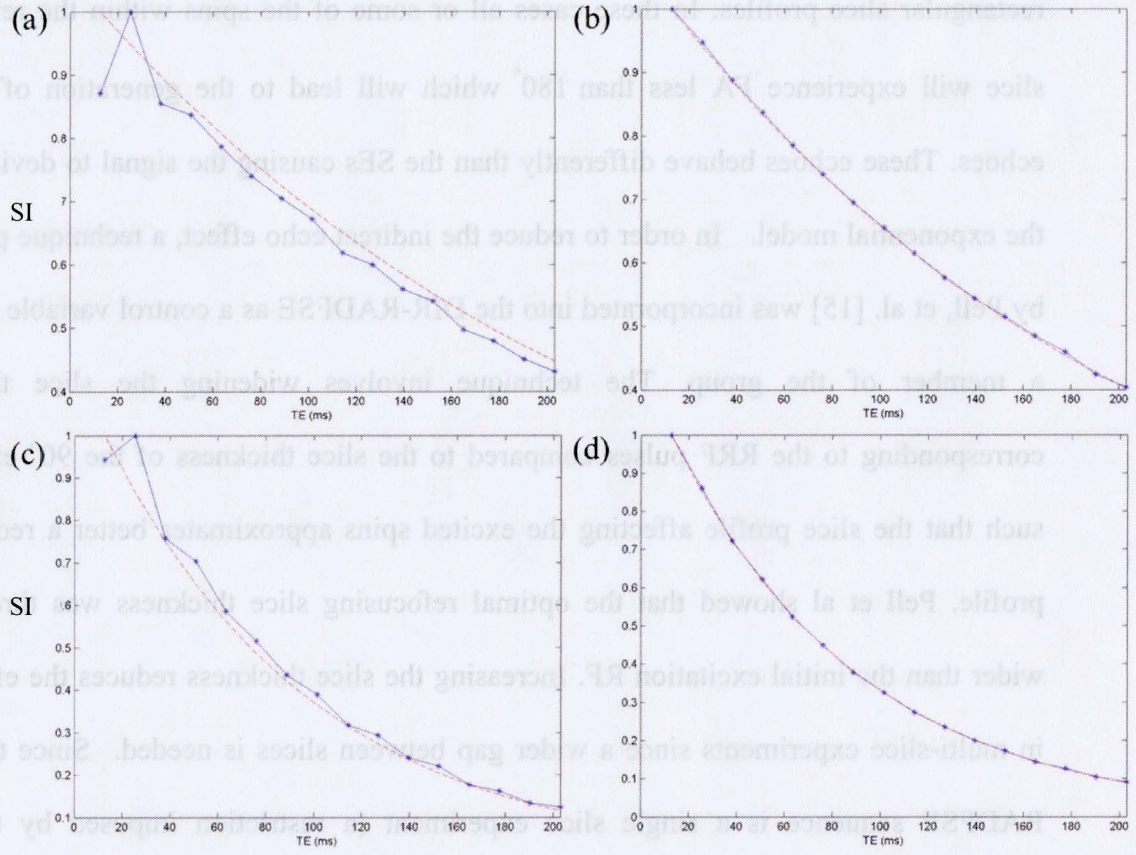

Figure 3.16. Plots of the signal decay with the refocusing slice thickness: (a,c) the same as the excitation slice thickness, and (b,d) three times thick.

The T_2 estimates were (a) 236.68 ms, (b) 208.79 ms, (c) 88.03 ms, and (d) 78.99 ms. Compared to the gold standard values, of 219.1 ms and 79.7 ms (obtained from a single echo SE experiment), data acquired with the three times thicker refocusing slice yielded more accurate T_2 estimates.

3.9. SERENADE algorithm

An alternative way to handle problems related to indirect echoes is to use a method called SlicE Resolved ExteNded phAse graph baseD rEconstruction of principal component coefficient maps (SERENADE) recently developed by our group [16]. It is an algorithm that incorporates the slice-resolved extended phase graph (SEPG) fitting algorithm [17] into a principal component-based reconstruction. The concept is similar to the REPCOM reconstruction but the signal model used in the reconstruction is based on the SEPG model. The latter takes into account the effects of T_2, B_1, and T_1 and utilizes the known slice profiles of the excitation and the RRFs to fit data to a more accurate signal model. The method is shown to produce accurate T_2 estimates from data acquired with FAs less than 180°. The main drawback of the SEPG model is that it is highly non-linear. By linearizing the signal model via principal components the method can be successfully used to reconstruct decay curves from highly undersampled data (less than 10% of the samples required by the Nyquist criteria) with non-180° RRFs.

3.10. Reproducibility study

In the previous sections, the experiments that I conducted were aimed at optimizing imaging of the heart with DIR-RADFSE and at observing the effects of different conditions in a qualitative manner. The experiments in this section were performed to evaluate the reproducibility of T_2 mapping with DIR-RADFSE. Table 3.2 summarizes the experiments chosen to test the effect of different conditions on reproducibility. The details as well as the advantages and disadvantages of the different conditions are summarized on the table.

The main differences between the experiments (Exps.) are:

Exps. #1 and #2: the use of a three times thick refocusing slice to test the effect of indirect echoes.

Exps. #2 and #3: the use of a shorter RRF for shortening the ETL and reduce the effects of heart motion during the acquisition of the echo train.

Exps. #3 and #4: the use of a higher RBW for further shortening the ETL and reduce the effects of heart motion during the acquisition of the echo train.

Exps. #3 and #5: removing SATs to test the effect of aliasing.

Exps. #3, #4, #5, and #6, #7, #8, respectively: the slice orientation (SA vs AX) to test the effect of aliasing which is less pronounced in the AX orientation.

Table 3.2. List of conditions for the reproducibility study.

Exp. #	RRF slice thick-ness	FA (degrees)	RBW (±kHz)	Slice	SAT	**Advantages**	**Disadvantages**
#1	1	180	32	SA	Yes	Better FA (180°) Streak reduction via SATs	More indirect echoes compared to #2 Longer ETL readout compared to #3
#2	3	180	32	SA	Yes	Better FA (180°) Streak reduction via SATs Less indirect echoes than #1	Longer ETL readout compared to #3
#3	3	155	32	SA	Yes	Shorter ETL readout Streak reduction via SATs	Potential lower SNR* and less indirect echo correction compared to #2 due to smaller FA
#4	3	155	62.5	SA	Yes	Shortest ETL readout Streak reduction via SATs	Potential lower SNR* compared to #3 due to higher RBW
#5	3	155	32	SA	No	Same as #3 and also faster to prescribe	More streaks expected
#6	3	155	32	AX	Yes	Same as #3, #4, #5, respectively Less aliasing artifacts compared to SA	More areas of low signal intensity (e.g. lungs)
#7	3	155	62.5	AX	Yes		
#8	3	155	32	AX	No		

* A decrease in SNR: shortening the refocusing RF pulse and/or increasing the RBW reduces the SNR however this could be compensated by the reduction in ETL since the TE data points are collected in the portion of the curve with more signal. Thus, the effect on SNR is not only dependent on the experimental parameters but also on the T_2 values of the tissues.

The reproducibility study was done on healthy volunteers consisting of three females and four males. Data were acquired twice for each condition without the subject changing position in the scanner. The slice prescription was kept the same for each orientation within a subject (in all cases a slice mid distance between the apex and base of the heart was chosen). Pre-scanning was performed before each acquisition. For Exp. #1, 2, 3, 4, 6, and 7, SATs were placed on the abdominal region along with the RF shield

blanket. The chemical shit saturation parameters (the power and the excitaion frequency of the chemical shift selective RF pulse) were adjusted for each subject. Data were acquired during mid-diastole with ETL = 16, TR = 1RR, FOV = 48 cm, excitation slice thickness = 8 mm, and acquisition matrix = 256 × 256.

3.10.1 Image reconstruction

Data reconstruction and T_2 mapping was done using the ES, REPCOM, and SERENADE algorithms. For the ES algorithm a full-tiered reconstruction was used to construct partial k-space data sets [8][9]. The missing k-space data points were obtained by linear interpolation. Images were reconstructed using FBP. For the REPCOM algorithm [11], a training set of decay curves, covering 16 TEs (from ~ 9 ms to 144 ms) and T_2 values ranging from 35 ms to 300 ms with a step size of 1 ms, was used for obtaining the principal components (PC). Three PCs were used in the reconstruction of the PC coefficient maps, from which the TE images were generated and a T_2 map was calculated. The training curves for SERENADE [16] were generated based on B_1, T_1, and T_2. The training curves covered the same TE range and T_2 values as in REPCOM with B_1 values ranging from 0.8 to 1.2 with a step size of 0.05. Since the SEPG signal model used in the SERENADE algorithm is not sensitive to T_1 variations, as shown by Lebel and Wilman [17], T_1 value was fixed to 1000 ms based on the findings on myocardial T_1, shown in a paper by Messroghli, et al. [23]. Both REPCOM and SERENADE have penalty terms for spatial sparsity. The weighting factors used for the penalty terms are obtained by multiplying 0.003 by the number of k-space lines (16 for each TE) and the

mean SI in the anatomical image (reconstructed with FBP using data at all TEs) once noise is removed. The algorithms for the ES, REPCOM, and SERENADE reconstructions are all coded in MATLAB (The MathWorks, inc.) and have been implemented by previous members of the group.

As an example, SA TE images and the T_2 map reconstructed with the ES method are shown in Figure 3.17 (for TE images, only the images for even TEs up to TE14 are shown). The T_2 map is thresholded by a mask created to remove background noise and show only the regions where SI of the corresponding anatomical image is greater than 7% of the maximum SI. The decaying SI can be seen in TE images. The SI of myocardium rapidly decreases and it is almost not visible at TE14. On the other hand, the SI of subcutaneous fat next to the heart can be seen even at TE14, which indicates that the T_2 value of fat is higher than that of myocardium.

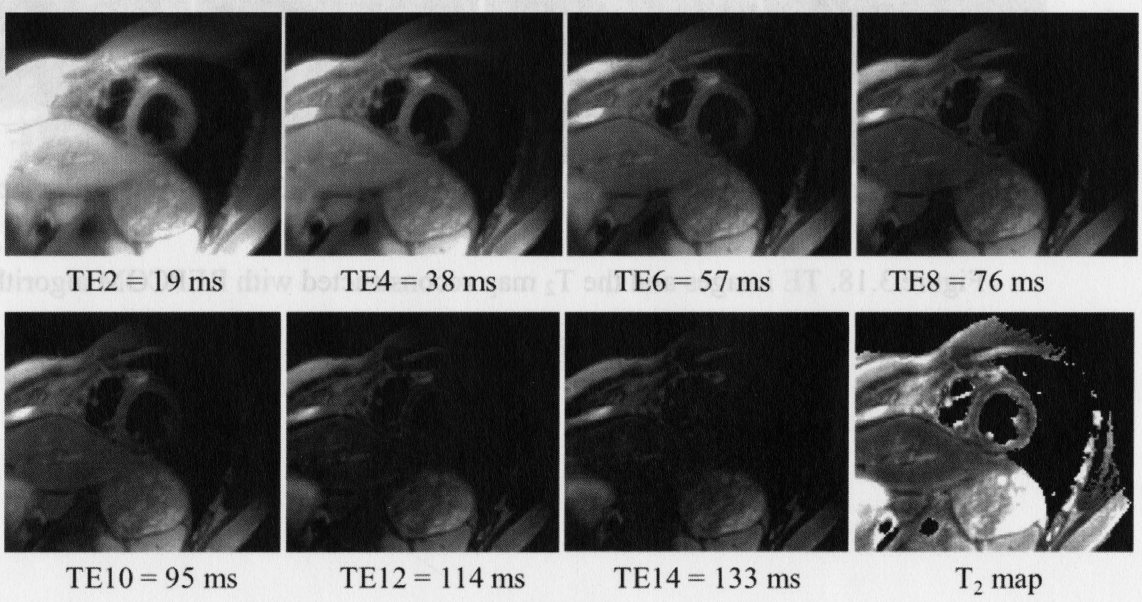

Figure 3.17. TE images and the T_2 map reconstructed with ES algorithm.

Figure 3.18 and 3.19 show the same subject's TE images and the T_2 map reconstructed with the REPCOM algorithm and the SERENADE algorithm respectively. The T_2 maps in Figure 3.18 and 3.19 used the same threshold as the one used in Figure 3.17 to remove noisy regions. Compared to the TE images reconstructed with the ES method, ones reconstructed with the PCA-based algorithms looked noisier especially in the background regions. The noise appearance was not very visible around the heart which is at the center of FOV.

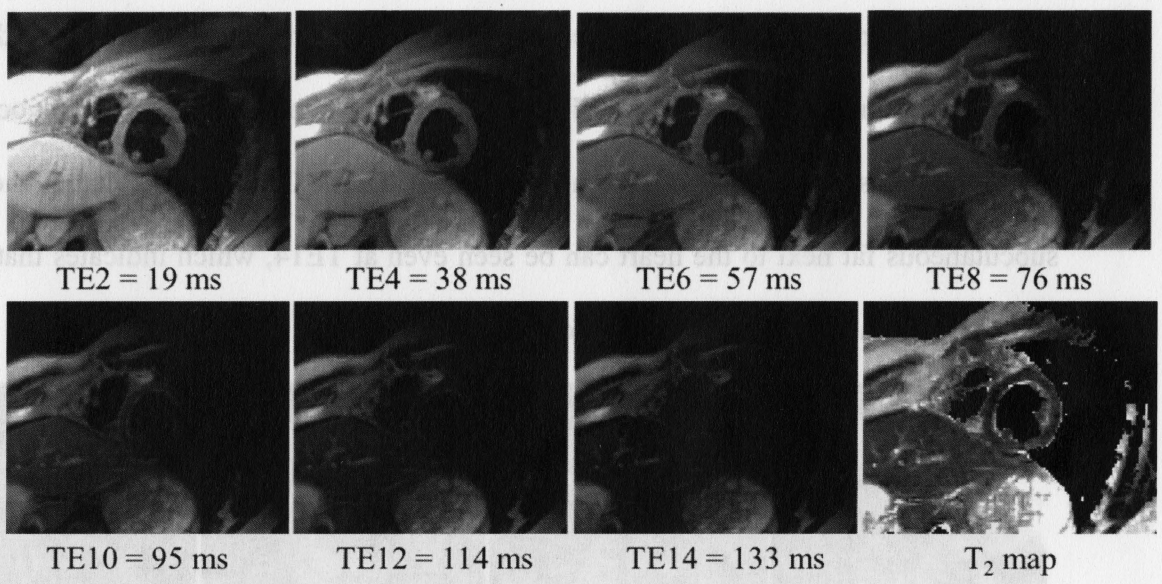

Figure 3.18. TE images and the T_2 map reconstructed with REPCOM algorithm.

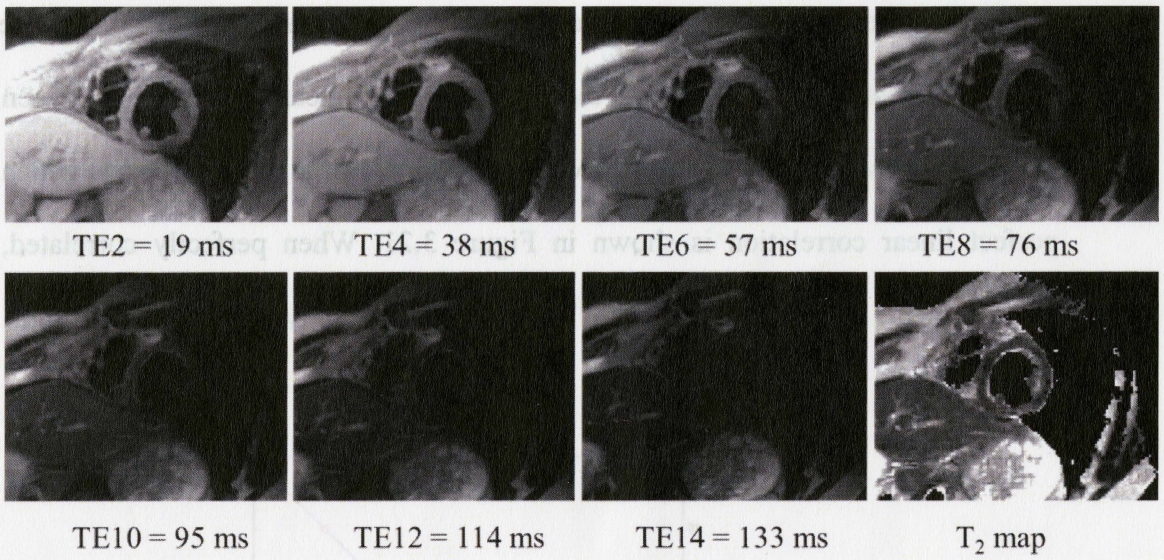

Figure 3.19. TE images and the T_2 map reconstructed with SERENADE algorithm.

3.10.2 Image analysis

For the reproducibility analysis of the T_2 measurement, an ROI of the LV was manually created for each image, as shown in Figure 3.20. The mean T_2 estimates from the ROI were determined for ES, REPCOM, and SERENADE algorithms.

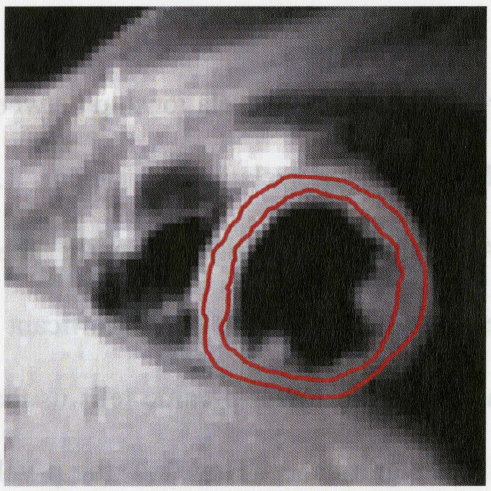

Figure 3.20. ROI drawn on an anatomical image.

The reproducibility of T_2 measurements was assessed using the Pearson's correlation test. The test measures the strength of the linear relationship between sets of Measure #1 (M1) and Measure #2 (M2). An example of a pair of datasets which have a perfect linear correlation is shown in Figure 3.21. When perfectly correlated, the i^{th} measurements from M1 and M2, $M1_i$ and $M2_i$ lie directly on a perfect straight line as shown.

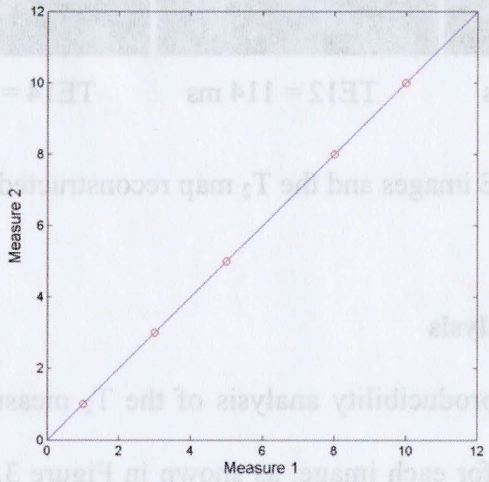

Figure 3.21. An example plot of a perfect linear correlation between a pair of measurements.

The strength of the linear relationship between two data points can be represented with the sample Pearson's correlation coefficient, R. The significance of R is determined by a p-value. A p-value here is a probability that the computed value R have occurred by chance. Hence the p-values tell us how significant the statistical results are. Therefore, obtaining higher R with a lower p-value tells us that the data sets are highly correlated with the statistical significance. How low the p-value should be depends on the study. However, a p-value less than 0.05 is often considered statistically significant [18]. For

this experiment, we chose 0.05 to be the cut-off value for evaluating the statistical significance of the finding. Both R's and p-values in this study were calculated in Matlab® by using a function called *corr*.

3.10.3. Results

Tables 3.3-3.10 show the T_2 estimates for the eight experiments described in Table 3.2. Each table shows data for all subjects and the three reconstruction methods used. For each reconstruction algorithm the T_2 estimates for the two different measurements are listed. N/A in Table 3.3-3.10 indicates that there are no data for the conditions due to the time constraint at the MRI scanner, or the breath-hold was not performed properly.

Table 3.3. Reproducibility study results for Experiment #1 (RRF 1x thick, FA=180°, SA slice, RBW = ± 32kHz).

	ES		REPCOM		SERENADE	
Subject	T_2 (ms), 1	T_2 (ms), 2	T_2 (ms), 1	T_2 (ms), 2	T_2 (ms), 1	T_2 (ms), 2
1	80.59	80.78	55.91	56.81	55.89	56.59
2	71.87	71.25	44.87	44.25	44.69	44.68
3	70.44	75.23	50.62	52.90	50.70	52.86
4	89.84	89.67	59.80	59.52	59.56	62.24
5	84.72	80.15	55.81	49.63	56.17	49.08
6	71.40	70.09	48.99	50.14	49.31	50.67
7	61.34	58.78	37.56	35.91	37.52	35.66

Table 3.4. Reproducibility study results for Experiment #2 (RRF 3x thick, FA=180°, SA slice, RBW = ± 32kHz).

	ES		REPCOM		SERENADE	
Subject	T_2 (ms), 1	T_2 (ms), 2	T_2 (ms), 1	T_2 (ms), 2	T_2 (ms), 1	T_2 (ms), 2
1	81.25	81.58	51.52	52.91	50.80	51.89
2	69.03	67.89	43.98	41.20	43.61	41.02
3	77.61	78.39	55.62	54.83	55.83	54.90
4	92.51	91.12	58.44	58.88	57.40	57.78
5	82.64	84.56	52.53	55.72	55.89	58.28
6	79.01	77.57	57.18	58.81	57.23	58.46
7	60.44	63.37	38.25	38.11	38.45	38.85

Table 3.5. Reproducibility study results for Experiment #3 (RRF 3x thick, FA =155°, SA slice, RBW = ± 32kHz).

	ES		REPCOM		SERENADE	
Subject	T_2 (ms), 1	T_2 (ms), 2	T_2 (ms), 1	T_2 (ms), 2	T_2 (ms), 1	T_2 (ms), 2
1	82.72	84.28	58.29	59.90	58.95	60.62
2	81.60	81.76	65.31	64.46	63.39	62.78
3	77.67	77.40	58.77	58.75	57.98	59.16
4	97.31	93.51	69.93	66.89	72.63	68.63
5	83.43	83.86	55.95	58.75	55.23	55.17
6	80.52	81.10	60.29	61.59	59.73	61.35
7	75.51	74.13	57.59	56.45	60.40	59.49

Table 3.6. Reproducibility study results for Experiment #4 (RRF 3x thick, FA=155°, SA slice, RBW = ± 62.5kHz).

	ES		REPCOM		SERENADE	
Subject	T_2 (ms), 1	T_2 (ms), 2	T_2 (ms), 1	T_2 (ms), 2	T_2 (ms), 1	T_2 (ms), 2
1	78.86	77.99	57.46	57.11	59.28	57.38
2	83.49	80.03	63.00	59.90	62.26	62.85
3	72.90	73.17	58.30	59.10	56.57	59.40
4	86.96	86.86	63.46	64.88	69.68	77.41
5	85.73	82.56	58.36	57.82	59.42	56.90
6	73.99	75.64	60.11	60.17	60.70	60.64
7	78.33	78.64	66.75	66.49	62.84	63.69

Table 3.7. Reproducibility study results for Experiment #5 (RRF 3x thick, FA=155°, SA slice, RBW = ± 32kHz, no SATs).

	ES		REPCOM		SERENADE	
Subject	T_2 (ms), 1	T_2 (ms), 2	T_2 (ms), 1	T_2 (ms), 2	T_2 (ms), 1	T_2 (ms), 2
1	N/A	N/A	N/A	N/A	N/A	N/A
2	81.42	83.00	61.12	62.68	62.88	60.28
3	73.98	77.06	57.29	59.22	57.48	58.39
4	97.34	98.59	67.90	66.55	64.52	66.52
5	84.78	84.01	57.06	55.22	55.04	53.71
6	81.99	80.59	60.01	60.52	59.50	60.21
7	85.72	84.15	57.81	59.91	66.77	66.33

Table 3.8. Reproducibility study results for Experiment #6 (RRF 3x thick, FA=155°, AX slice, RBW = ± 32kHz).

	ES		REPCOM		SERENADE	
Subject	T_2 (ms), 1	T_2 (ms), 2	T_2 (ms), 1	T_2 (ms), 2	T_2 (ms), 1	T_2 (ms), 2
1	80.72	80.71	62.52	62.74	61.34	60.54
2	81.94	81.15	68.32	67.61	70.37	68.06
3	73.75	74.73	63.15	61.58	60.78	61.46
4	95.69	95.58	77.85	71.44	75.13	77.21
5	86.28	88.35	64.10	65.77	63.43	66.40
6	80.43	81.05	63.67	65.20	62.57	64.57
7	85.41	86.14	74.45	67.64	74.47	70.74

Table 3.9. Reproducibility study results for Experiment #7 (RRF 3x thick, FA=155°, AX slice, RBW = ± 62.5kHz).

	ES		REPCOM		SERENADE	
Subject	T_2 (ms), 1	T_2 (ms), 2	T_2 (ms), 1	T_2 (ms), 2	T_2 (ms), 1	T_2 (ms), 2
1	76.66	78.04	62.23	63.22	60.78	62.14
2	83.46	82.33	69.86	69.33	71.48	70.99
3	73.40	71.62	61.25	61.02	62.92	59.93
4	98.66	99.27	73.88	75.49	74.78	71.45
5	86.19	86.85	62.00	71.36	63.91	72.94
6	71.99	73.15	60.73	60.88	61.09	61.09
7	83.87	83.30	70.98	74.72	79.40	74.46

Table 3.10. Reproducibility study results for Experiment #8 (RRF 3x thick, FA=155°, AX slice, RBW = ± 32kHz, no SATs).

	ES		REPCOM		SERENADE	
Subject	T_2 (ms), 1	T_2 (ms), 2	T_2 (ms), 1	T_2 (ms), 2	T_2 (ms), 1	T_2 (ms), 2
1	76.83	77.59	62.44	64.71	61.18	63.14
2	85.32	86.42	73.69	68.82	74.81	69.92
3	73.94	73.98	61.80	61.65	61.52	60.97
4	N/A	N/A	N/A	N/A	N/A	N/A
5	86.58	88.59	62.21	62.69	63.63	64.13
6	75.45	76.39	60.67	63.38	61.46	62.63
7	88.97	87.78	78.92	74.00	76.26	70.77

A summary of the statistical results (R and p values) for all eight experiments and the three reconstruction methods is given on Table 3.11. Figure 3.22 shows examples of the correlation plots for the ES algorithm which illustrates the high correlation between each pair of measurements, much like the plot shown in Figure 3.21.

Table 3.11. Statistical results.

Exp. #	RRF slice thickness	FA (degrees)	RBW (±kHz)	Slice	SAT	**R/p-value ES**	**R/p-value REPCOM**	**R/p-value SERENADE**
1	1	180	32	SA	Yes	0.9565/ 0.0007	0.9373/ 0.0018	0.9202/ 0.0033
2	3	180	32	SA	Yes	0.9876/ 0.00003	0.9785/ 0.00013	0.9843/ 0.0001
3	3	155	32	SA	Yes	0.9743/ 0.0002	0.9419/ 0.0015	0.9633/ 0.0005
4	3	155	62.5	SA	Yes	0.9496/ 0.0011	0.9171/ 0.0036	0.9374/ 0.0018
5	3	155	32	SA	No	0.9691/ 0.0014	0.9059/ 0.0121	0.9405/ 0.0052
6	3	155	32	AX	Yes	0.9908/ 2E-5	0.8894/ 0.0073	0.9176/ 0.0036
7	3	155	62.5	AX	Yes	0.9917/ 1E-5	0.8326/ 0.0201	0.7848/ 0.0366
8	3	155	32	AX	No	0.9860/ 0.0003	0.9666/ 0.0017	0.9041/ 0.0134

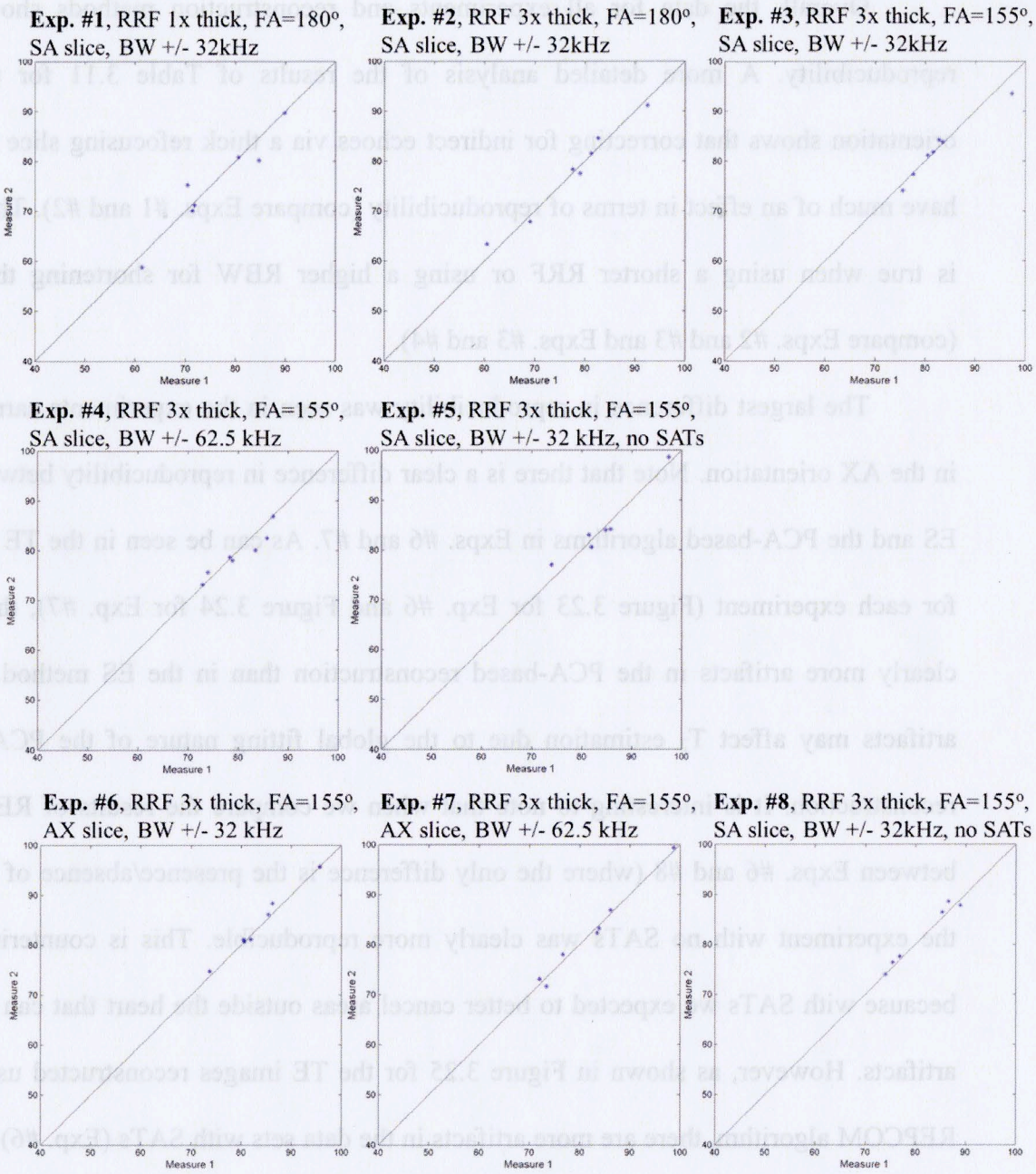

Figure 3.22. Correlation plots for T_2 estimates obtained with the ES algorithm.

Overall, the data for all experiments and reconstruction methods show high reproducibility. A more detailed analysis of the results of Table 3.11 for the SA orientation shows that correcting for indirect echoes via a thick refocusing slice did not have much of an effect in terms of reproducibility (compare Exps. #1 and #2). The same is true when using a shorter RRF or using a higher RBW for shortening the ETL (compare Exps. #2 and #3 and Exps. #3 and #4).

The largest difference in reproducibility was seen in the experiments carried out in the AX orientation. Note that there is a clear difference in reproducibility between the ES and the PCA-based algorithms in Exps. #6 and #7. As can be seen in the TE images for each experiment (Figure 3.23 for Exp. #6 and Figure 3.24 for Exp. #7), there are clearly more artifacts in the PCA-based reconstruction than in the ES method. These artifacts may affect T_2 estimation due to the global fitting nature of the PCA-based reconstruction. It is interesting to note that when we compare the results of REPCOM between Exps. #6 and #8 (where the only difference is the presence/absence of SATs), the experiment with no SATs was clearly more reproducible. This is counterintuitive because with SATs we expected to better cancel areas outside the heart that can lead to artifacts. However, as shown in Figure 3.25 for the TE images reconstructed using the REPCOM algorithm, there are more artifacts in the data sets with SATs (Exp. #6) than in those without SATs (Exp. #8). It is not clear why the presence of SAT bands introduced more artifacts in the TE images. It is possible that the PCA-based reconstruction do not perform well in the areas of the FOV where the SATs are placed due to a lower SNR and

this influences the global fitting of the data. However, more work is needed to test this hypothesis.

In general we expected data acquired in the AX orientation to be more reproducible than data acquired in the SA orientation because in the former there should be less artifacts due to aliasing. With the ES reconstruction, the axial scans have slightly higher reproducibility than the SA counterparts, but this was not always the case with the PCA-based methods (compare Exps. #3 to #6 and Exps. #4 to #7). As can be seen from the TE images in Figure 3.26 (Exps. #3 and #6) and Figure 3.27 (Exps. #4 and #7), there are more artifacts in the AX data. In the AX orientation there are more areas of low signal intensity (e.g. in lungs) which is consistent with the idea that the presence of regions with low SNR may lead to a more unstable reconstruction in the PCA-based methods.

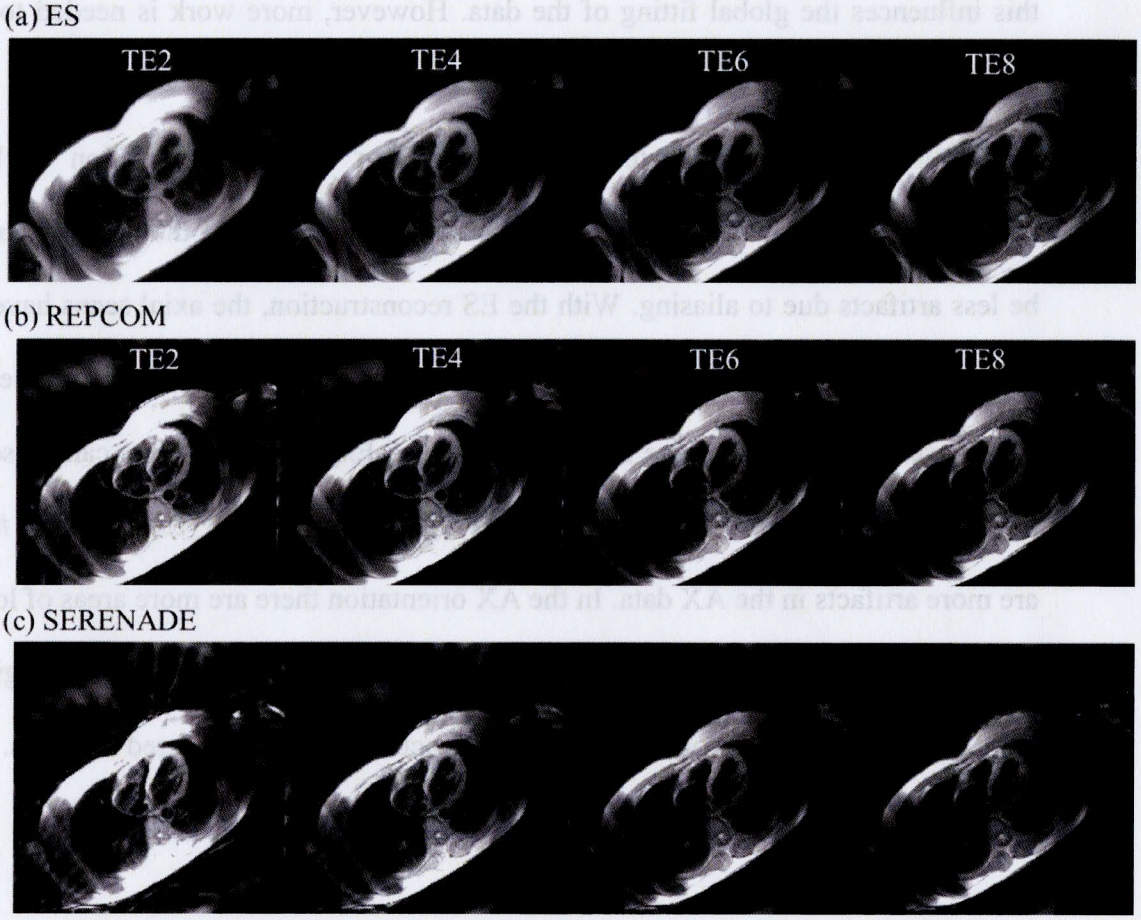

Figure 3.23. TE images for Exp. #6 (AX orientation, three times thick refocusing slice, FA = 155°, RBW = ± 32 kHz, with SATs), reconstructed with (a) ES, (b) REPCOM, and (c) SERENADE.

(a) ES

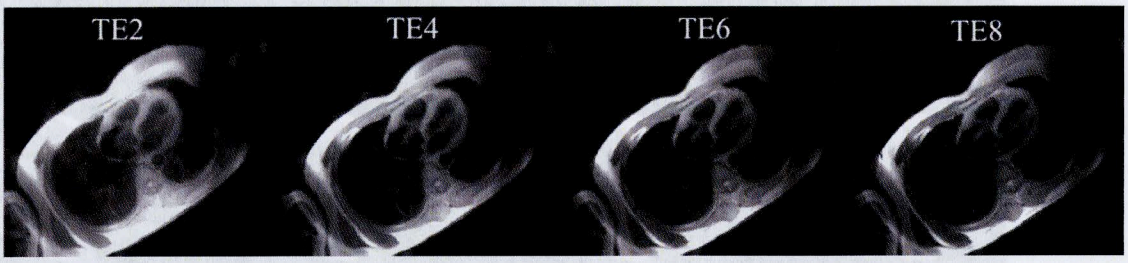

(b) REPCOM

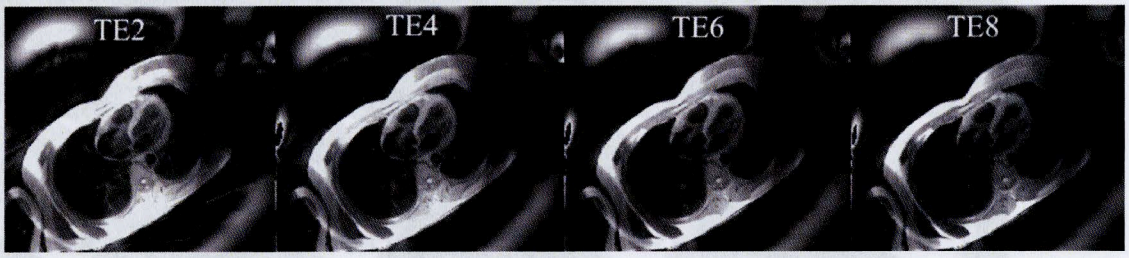

(c) SERENADE

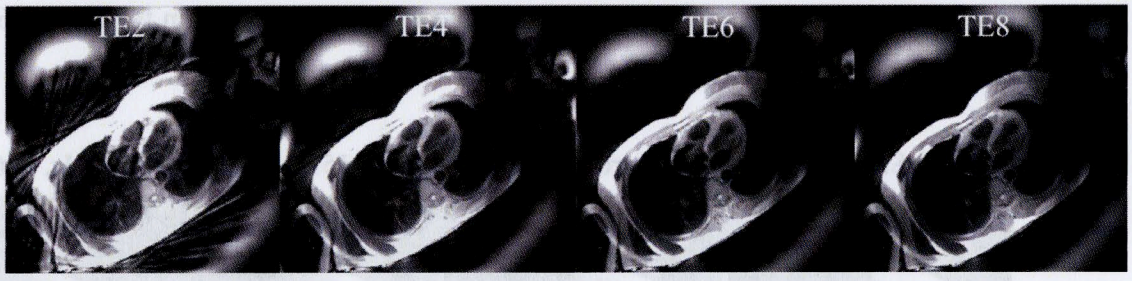

Figure 3.24. TE images for Exp. #7 (AX orientation, three times thick refocusing slice, FA = 155°, RBW = ± 62.5kHz, with SATs), reconstructed with (a) ES, (b) REPCOM, and (c) SERENADE algorithms.

Exp. #6: three times thicker refocusing slice, FA = 155°, with SATs

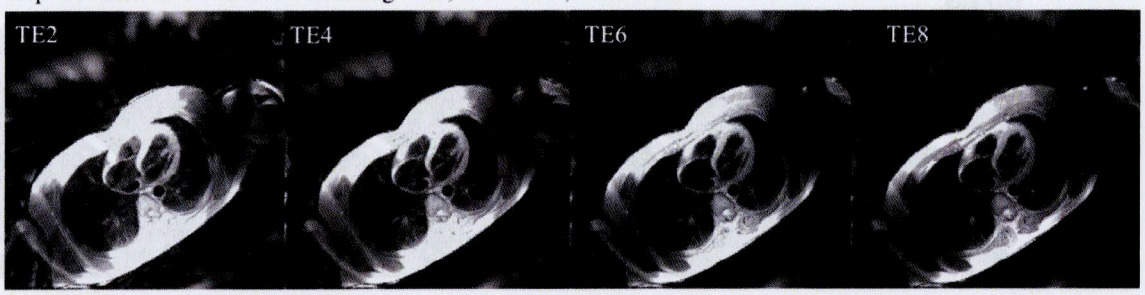

Exp. #8: three times thicker refocusing slice, FA = 155°, without SATs

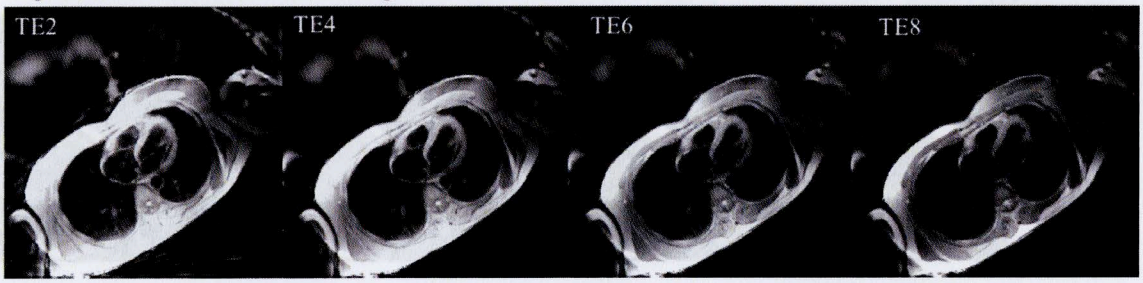

Figure 3.25. TE images reconstructed with the REPCOM algorithm for Exps. #6 and #8.

Exp.#3: SA, three times thicker refocusing slice, FA = 155°, RBW = +/- 32 kHz, with SATs

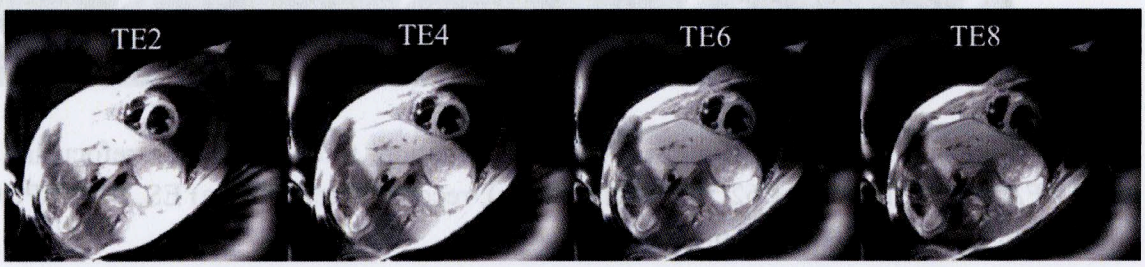

Exp.#6: AX, three times thicker refocusing slice, FA = 155°, RBW = +/- 32 kHz, with SATs

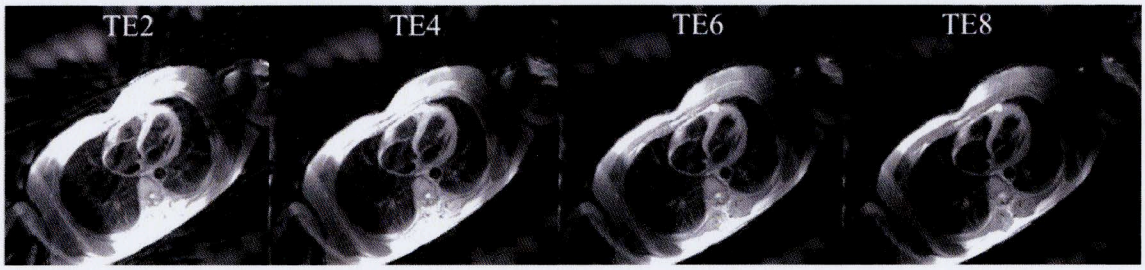

Figure 3.26. TE images reconstructed with the REPCOM algorithm for Exps. #3 and #6.

Exp.#4: SA, three times thicker refocusing slice, FA = 155°, RBW = +/- 62.5 kHz, with SATs

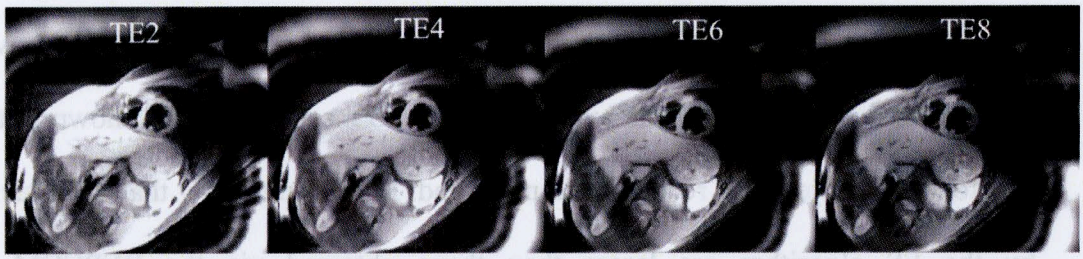

Exp.#7: AX, three times thicker refocusing slice, FA = 155°, RBW = +/- 62.5 kHz, with SATs

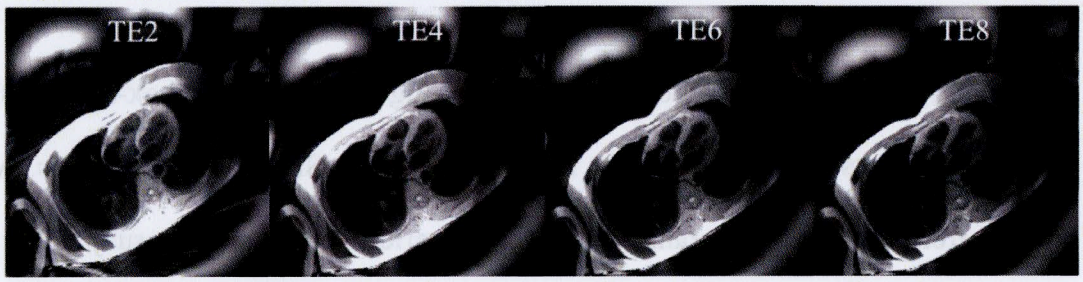

Figure 3.27. TE images reconstructed with the REPCOM algorithm for Exps. #4 and #7.

In addition to the reproducibility study, we also looked at the effects of the experimental conditions and reconstruction methods on the actual T_2 values. Table 3.12 shows the T_2 values for each experiment (the average of the two measurements is shown in the table) and for each subject and reconstruction method. The results show that T_2 values yielded by the ES algorithm are larger than those obtained via the REPCOM and the SERENADE methods. We also looked at the spread of the T_2 values across different imaging conditions (i.e. across experiments). Figure 3.28 shows box-and-whisker plots for all subjects for the (a) ES, (b) REPCOM, and (c) SERENADE methods. As can be seen from the figure, the range of T_2 values varies from subject to subject but the only consistent finding was that the ES method yields larger T_2 values as compared to the REPCOM and SERENADE methods. This may be due to the magnitude reconstruction used to obtain the TE images in the ES algorithm. The current implementation of the ES algorithm uses magnitude data for the images of each receiver coil and the sum-of-squares is used to obtain the TE image that are used in the T_2 estimation (via least squares fitting). Taking the magnitude of the data causes the noise distribution to become nongaussian (i.e. strictly positive), which affects more the data points with low SNR (data at the latter TE points). The SI for the latter TE points is higher due to the magnitude operation and the resulting T_2 values are higher. One way to overcome this is to use the complex data from all the coils and fit the real and the imaginary parts jointly in a least squares fashion. In REPCOM and SERENADE the k-space data is fit to the the PCA-based signal model and are not affected by problems associated with a magnitude reconstruction.

Table 3.12. Comparison of T_2 values (ms) among all experiments for different reconstruction algorithms. The T_2 values per subject are the averaged of the two measurements.

ES

Exp. #	1	2	3	4	5	6	7	8
Subject 1	80.69	81.42	83.50	78.43	N/A	80.72	77.35	77.21
Subject 2	71.56	68.46	81.68	81.76	82.21	81.55	82.90	85.87
Subject 3	72.84	78.00	77.54	73.04	75.52	74.24	72.51	73.96
Subject 4	89.76	91.82	95.41	86.91	97.97	95.64	98.97	N/A
Subject 5	82.44	83.60	83.65	84.15	84.40	87.32	86.52	87.59
Subject 6	70.75	78.29	80.81	74.82	81.29	80.74	72.57	75.92
Subject 7	60.06	61.91	74.82	78.49	84.94	85.78	83.59	88.38

REPCOM

Exp. #	1	2	3	4	5	6	7	8
Subject 1	56.36	52.21	59.10	57.28	N/A	62.63	62.72	63.58
Subject 2	44.56	42.59	64.88	61.45	61.90	67.96	69.59	71.25
Subject 3	51.76	55.22	58.76	58.70	58.25	62.36	61.13	61.72
Subject 4	59.66	58.66	68.41	64.17	67.23	74.65	74.68	N/A
Subject 5	52.72	54.12	57.35	58.09	56.14	64.93	66.68	62.45
Subject 6	49.56	58.00	60.94	60.14	60.26	64.44	60.81	62.03
Subject 7	36.74	38.18	57.02	66.62	58.86	71.05	72.85	76.46

SERENADE

Exp. #	1	2	3	4	5	6	7	8
Subject 1	56.24	51.34	59.79	58.33	N/A	60.94	61.46	62.16
Subject 2	44.69	42.32	63.08	62.55	61.58	69.22	71.24	72.36
Subject 3	51.78	55.36	58.57	57.99	57.94	61.12	61.42	61.25
Subject 4	60.90	57.59	70.63	73.55	65.52	76.17	73.11	N/A
Subject 5	52.63	57.09	55.20	58.16	54.38	64.91	68.42	63.88
Subject 6	49.99	57.85	60.54	60.67	59.86	63.57	61.09	62.05
Subject 7	36.59	38.65	59.94	63.27	66.55	72.60	76.93	73.69

a) ES method

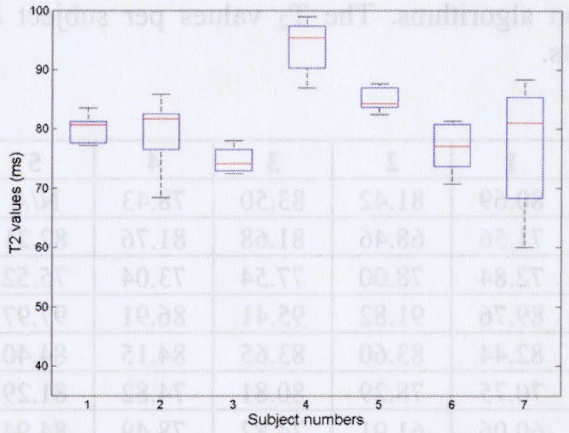

b) REPCOM method

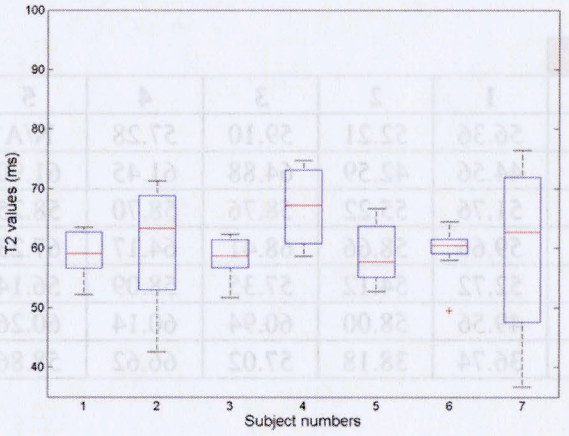

c) SERENADE method

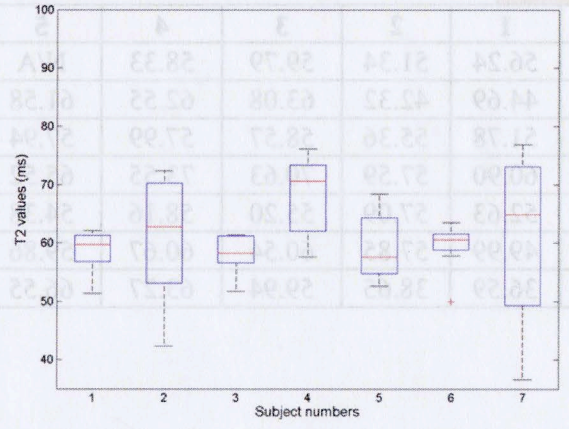

Figure 3.28. Whisker-box plots of all subjects for the three algorithms.

Figure 2.29 (a) shows an example of TE data reconstructed with the ES algorithm exhibiting an increase in SI on the last TE points. The plotted data (blue curve) are for a region within the myocardium for one of the subjects in the reproducibility study (Subject #6, Exp. #1). The best fit is shown by the red curve. Similar increases in SI among the latter TE time points were seen across other experimental conditions and subjects. Figures 3.29 (b) and (c) show the data for the same subject without the last 2 and 3 TE data points, respectively. Except for data around TE2, where there is a clear deviation from the single exponential model due to indirect echoes, the rest of the data points (from TE3 on) are very close to the fitted curves in both (b) and (c). Note that by removing the data points at latter TEs, the estimated T_2 was reduced by ~ 6 ms compared to the T_2 estimated using all the data. Similar reductions were observed for other subjects and experimental conditions.

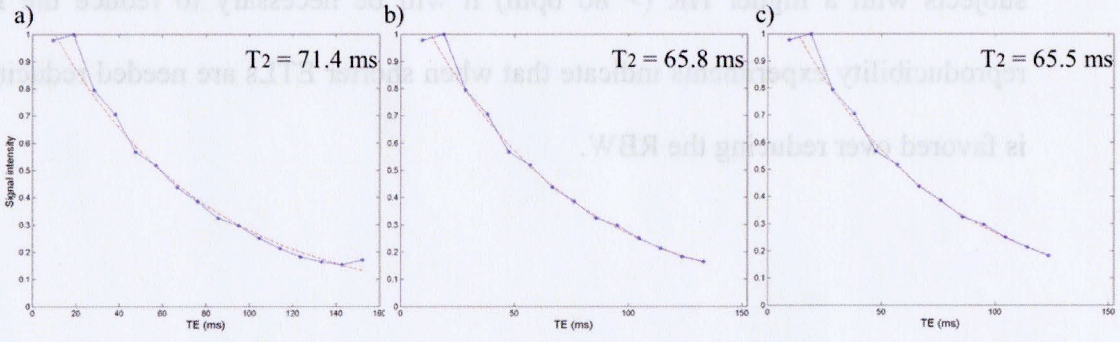

Figure 3.29. Decay curves for in vivo data reconstructed with the ES algorithm. (a) Data for the TE1-TE16 data points (all TE points), (b) for TE1-TE14, and (c) for TE1-TE13.

3.11. Conclusion

By means of the studies described above, we have optimized an imaging protocol using DIR-RADFSE, which makes use of the following in all CMR procedures: the maximum FOV to reduce the artifacts coming from outside the FOV, a RF shield blanket to reduce the unwanted signal within and outside the FOV (covering the abdominal regions below the heart), chemical shift suppression on fat, and SATs placed on both of the arms as well as the abdominal regions and, depending on the subject, in other areas with high SI (i.e. over abdominal fat and shoulder regions if necessary).

The reproducibility study indicated that in the SA orientation most of the experimental conditions were similar. However, acquiring data with a three times thick refocusing slice should be preferable due to the improved profile of the refocusing slice. The experiments above were performed in healthy volunteers with HR < 80 bpm. For subjects with a higher HR (> 80 bpm) it will be necessary to reduce the ETL. The reproducibility experiments indicate that when shorter ETLs are needed reducing the FA is favored over reducing the RBW.

Chapter 4

IMAGING OF SUBJECTS

4.1. Patient Data

After the initial optimization on phantoms and volunteers (work described on Sections 3.2 – 3.4), I started to evaluate the utility of T_2 mapping with DIR-RADFSE on patients. The patient evaluation was carried out in parallel to the optimization and reproducibility experiments described in Sections 3.5 – 3.10. The imaging of patients was done as a collaborative study with physicians in the division of Cardiology at the University of Arizona Medical Center. The imaging studies were performed according to the regulations of the Internal Review Board at the University of Arizona

A total of 30 patients were enrolled, of which 28 patients, 15 females and 13 males (mean age = 48 y, mean weight 78.8 kg) were able to complete the study. The patients came for a CMR evaluation for various cardiac conditions. Since the goal of this study was to evaluate whether DIR-RADFSE was suitable for imaging patients, we imaged every subject who agreed to participate in the study regardless of the specific heart condition. Out of the 28 subjects scanned, 12 patients had a myocardium related abnormality which, according to the medical report generated after the CMR exam, included scar/fibrosis (detected in the DE images), cardiomyopathy, and myocarditis. Five patients did not have any significant finding; the rest of the patients had coronary artery disease and/or congenital heart disease without any scar/fibrosis. Three cases on different diseases/conditions are selected for discussion in this chapter.

DIR-RADFSE data were acquired as part of the regular clinical examination with the following parameters (standard parameters used for DIR-RADFSE at the time): FOV = 48 cm, slice thickness = 8 mm, ETL = 16, RBW = ±31.25 kHz, the standard RRF thickness with 180° FA, acquisition matrix = 256 × 256, and TR = 1RR with PG gating. An eight channel receiver coil was used. The RF shield blanket, SATs, and chemical shift suppression were used.

For each case below the TE and anatomical images and the T_2 maps, reconstructed with the ES algorithm, are shown. In all cases the DE images, acquired 10 – 15 minutes after the intravenous injection of MultiHance (gadobenate dimeglumine, Bracco Diagnostics Inc., USA) are shown. The dose of MultiHance was 0.1 mmol/kg. The DE images were acquired as part of the clinical examination using ECG triggering and during the systolic phase of the cardiac cycle. In most of the cases shown in this chapter, the data for all sequences were acquired at the same location and with the same orientation except for the example shown in Section 4.1.1, where the DE data were acquired with a slightly different orientation (i.e., the prescription of the SA view was not the same as for the DIR-RADFSE scan). For each, there is also a comparison between the T_2 maps reconstructed with the ES, and the PCA-based methods (REPCOM and SERENADE).

For comparison, Figure 4.1 shows a T_2 map and a DE image of a patient who was not found to have any heart abnormality after the CMR examination. The figure shows the anatomical image (reconstructed using data at all TEs) as well as the colorized T_2 map overlaid onto the anatomical image. The uniform blue-toned myocardium can be

seen in the T_2 map which corresponds to T_2 values ranging from 60 to 80 ms. The DE image shows a uniformly darker myocardium compared to the LV cavity. There is no enhancement within the myocardium which shows that the heart muscle is viable (necrotic scar tissue would have a brighter appearance as shown in the next section).

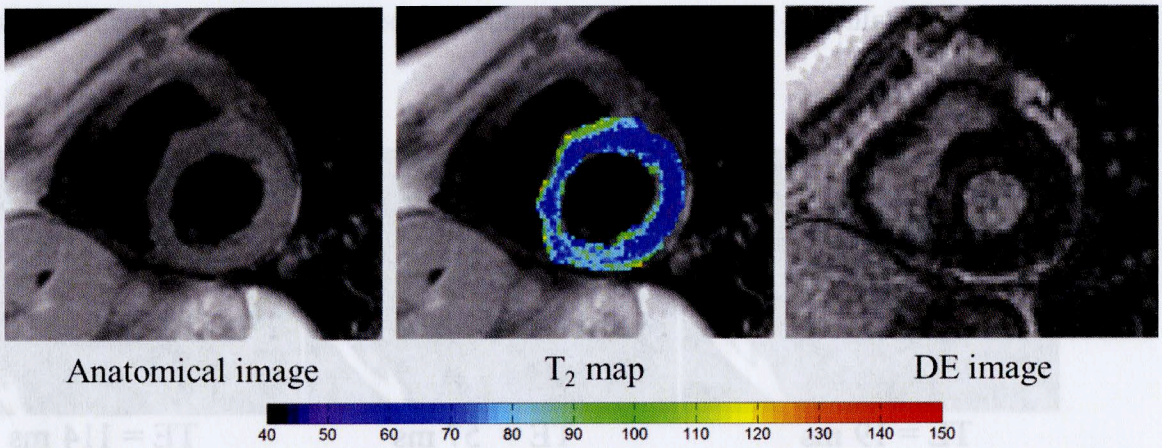

Figure 4.1. Images of a healthy patient.

4.1.1. Cardiomyopathy

In this section, a case of cardiomyopathy is presented. Cardiomyopathy is a general term of an intrinsic disease of the myocardium. There are many kinds of cardiomyopathies. The one shown in Figure 4.2 is the most common cardiomyopathy called, hypertrophic cardiomyopathy, where the myocardium is thickened and enlarged. In Figure 4.2., the images shown on the top row are TE images at different TE time points (only three out of sixteen TE images are shown), and the bottom row shows the anatomical image, the colorized T_2 map overlaid onto the anatomical image, and the DE image.

The DE images showed evidence of myocardial scar/fibrosis. One of the DE images is shown in Figure 4.2 where arrows indicate areas of fibrosis. The disorganized pattern of fibrosis suggests an infiltrative disorder, e.g. cardiac sarcoidosis, which is an immunologic disease with chronic inflammation. The T_2 map in Figure 4.2 shows elevated T_2 values (~130 ms) at the RV insertion point (red arrow) which suggested the presence of edema.

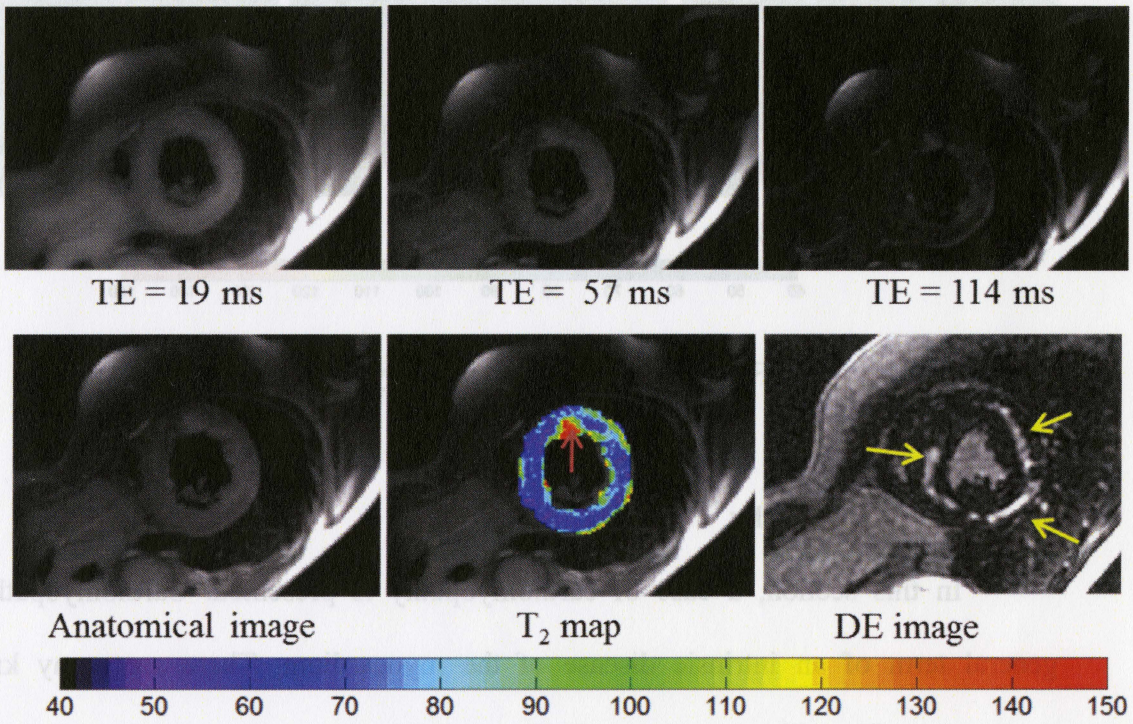

Figure 4.2. Images of a patient with hypertrophic cardiomyopathy.

Figure 4.3 below shows colorized T_2 maps of the myocardium from all three algorithms: ES, REPCOM, and SERENADE. The findings (elevated T_2 values in the RV insertion point) were similar for all reconstruction methods. Overall T_2 values were lower in the T_2 map reconstructed with the PCA-based methods. For the entire region shown in

the figure the mean T_2 values were 80 ms for ES and 72.5 ms for both REPCOM and SERENADE. The parameters used in the REPCOM and SERENADE reconstructions were the same as those described in Section 3.10.1.

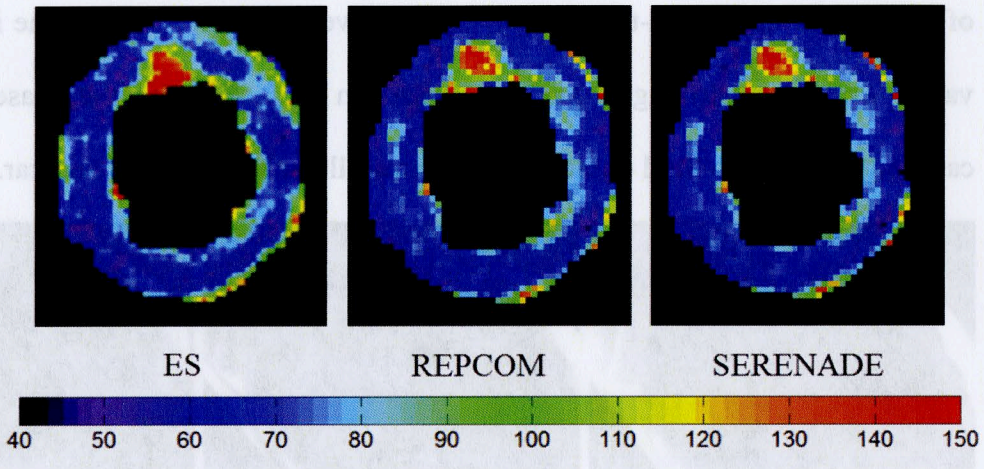

Figure 4.3. T_2 maps reconstructed with ES, REPCOM and SERENADE algorithms.

4.1.2. Myocardial infarction

Figure 4.4 shows images from a patient with a history of cardiomyopathy, coronary artery disease, and a MI incidence. The infarct region is characterized by a thinning of the wall as well as by the presence of scar tissue which can be seen as an area of bright signal in the DE image (arrow). Scars are mainly composed of fibrous tissue and arise after several weeks/months during the healing process (healing time differs in individuals). A recent MI (< 1 week) would typically show signs of edema in the region where the insult occurred, whereas an old MI would only show scar tissue. The clinical findings for this patient did not indicate the presence of edema.

The DIR-RADFSE images show the thinned myocardial wall and higher T_2 values around the region corresponding to scarred tissue in the DE image. The average T_2 around the scarred region (light green region at arrow) was ~ 95 ms. In contrast, the rest of the myocardium (blue-toned color) had the average T_2 of ~70 ms. The increase in T_2 values was not as striking as the case in Section 4.1.1. The slight increase in T_2 in this case might be due to fluid or blood in the extracellular space within the scar.

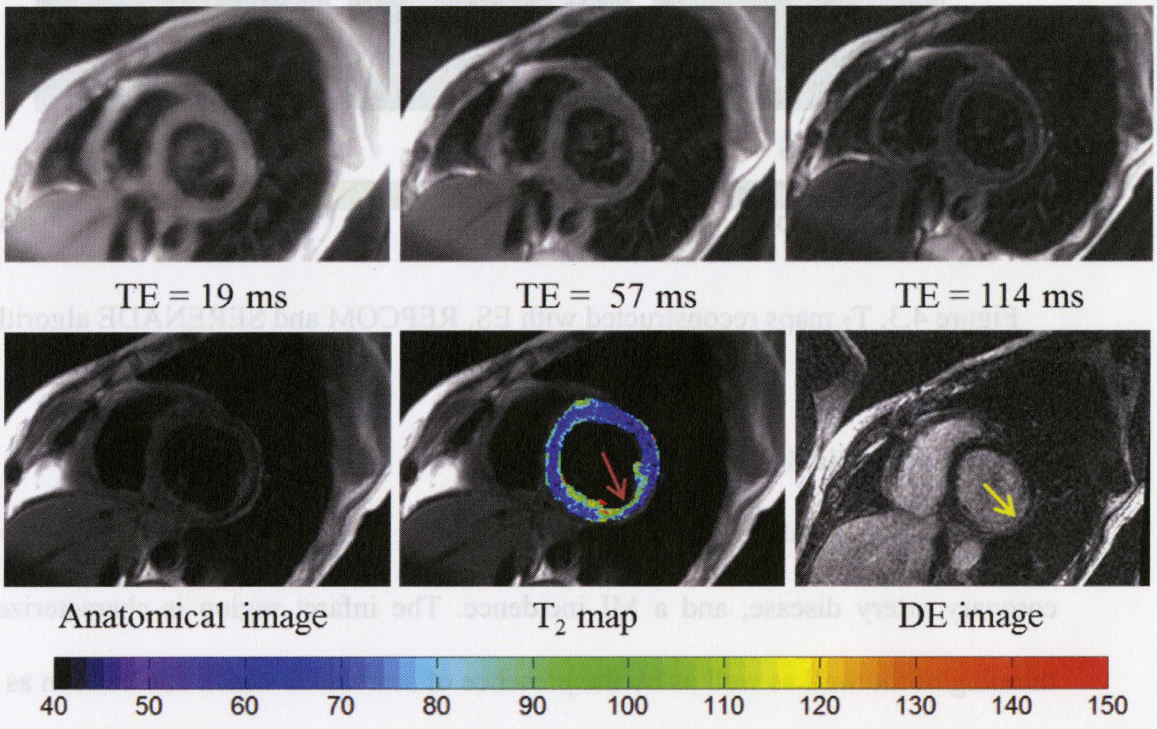

Figure 4.4. Images of a patient with scar tissue due to myocardial infarction.

Figure 4.5 shows T_2 maps reconstructed with all three reconstruction algorithms. As shown previously, overall the T_2 values were higher with the ES algorithm compared to the PCA-based methods. All algorithms showed high T_2 values around the scar. The T_2 was also elevated near edges in the ES algorithm (arrows in Figure 4.5), which is a

common artifact seen with this algorithm. The edge enhancement is not seen with the PCA-based algorithms. As mentioned in Chapter 2, PCA-based T_2 estimation algorithms perform well near edges and in small structures, such papillary muscles along the interior wall.

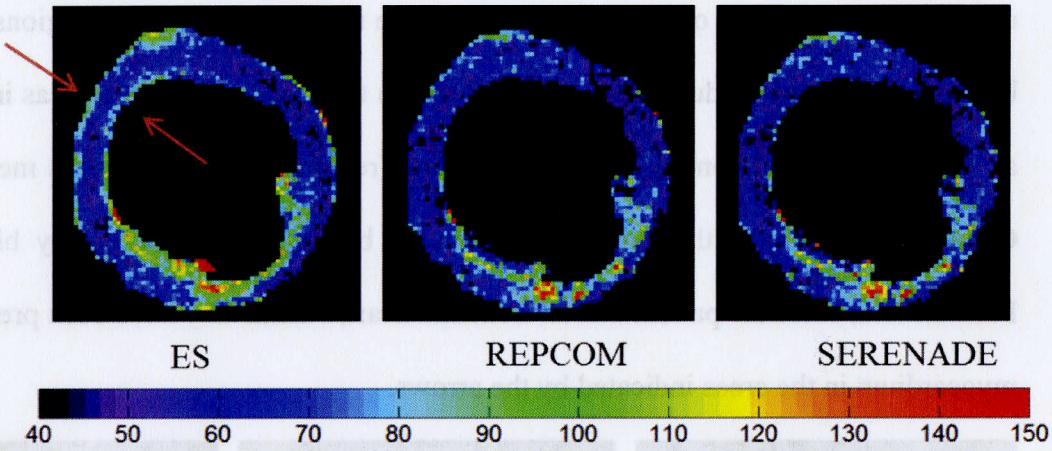

Figure 4.5. T_2 maps reconstructed with ES, REPCOM and SERENADE algorithms.

4.1.3. Ischemic heart with reduced cardiac output

Thus far, we have shown cases where the myocardium was affected but its function was not altered significantly. When large regions of the myocardium have scars, the heart fails to function properly. An example of this is depicted in Figure 4.6 for a subject with an enlarged LV that showed eccentric hypertrophy (characterized by an increase in heart size as well as an increase in wall thickness [13]). As a result, extensive wall motion abnormalities were noted. The DE image shows evidence of scarring at multiple locations within the LV (indicated by arrows). The scar involved 25~75% of the myocardial wall thickness depending upon the location. The ejection fraction of the LV (i.e. the fraction of the end-diastolic volume that is ejected with each heart beat) was only

18%. Compared to a normal heart, in which case the ejection fraction is expected to be 55% on the low end, this heart is malfunctioning and the blood is not being ejected properly. The T_2 map showed regions of elevated T_2 within the posterior myocardial wall (indicated by arrows) which correspond to areas in the DE images that showed enhancement for ~75% of the wall thickness. The increase in T_2 (in the regions indicated by the arrows) may be due to fluid trapped within the scar tissue (green areas in the map) as well as the signal coming from steady blood (red areas in the map). As mentioned in Chapter 2, DIR nulls the signal from flowing blood but not the steady blood pool. Furthermore, since the patient had an ischemic heart, edema may have been present in the myocardium in the areas indicated by the arrows.

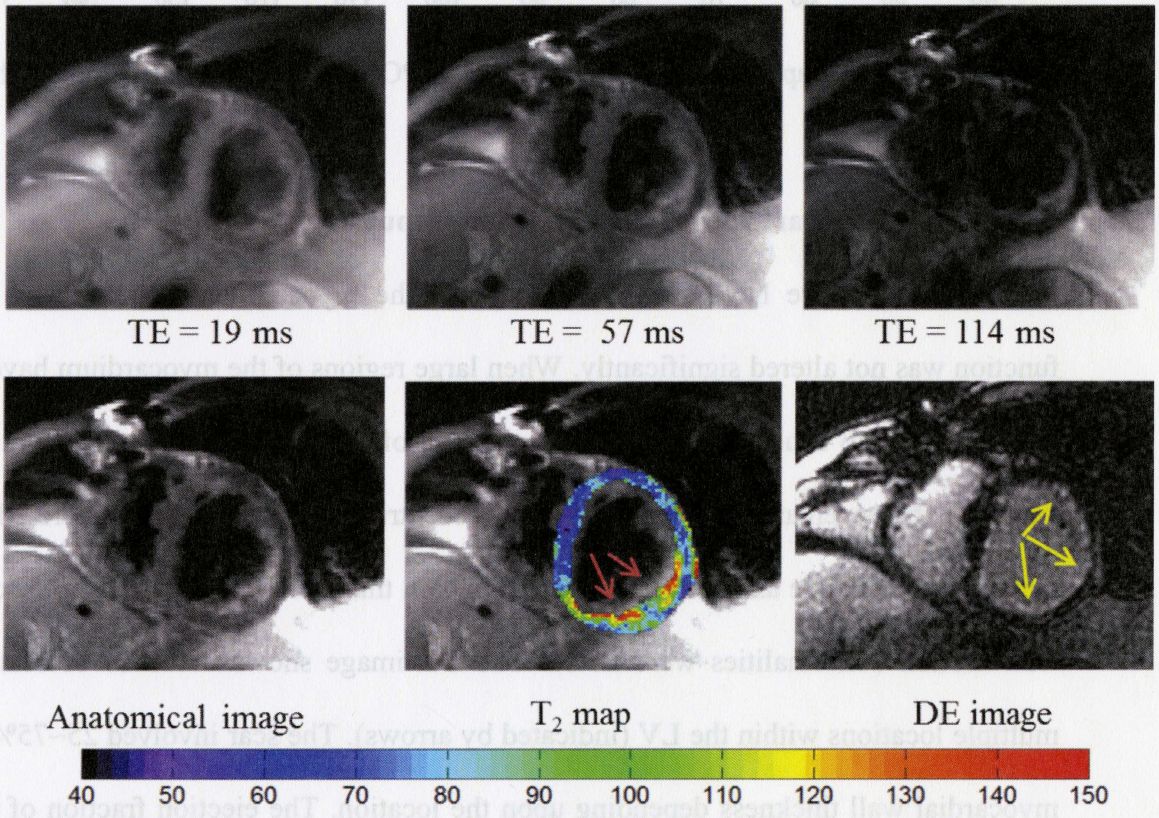

Figure 4.6. Images of a patient with ischemic cardiomyopathy with fibrosis.

T_2 maps reconstructed with the ES and the PCA-based algorithms are shown in Figure 4.7. The T_2 values for the normal regions of the myocardium are lower in the maps reconstructed with the PCA-based methods. However the T_2 values in the region indicated by arrows are higher for the PCA-based compared to the ES algorithm.

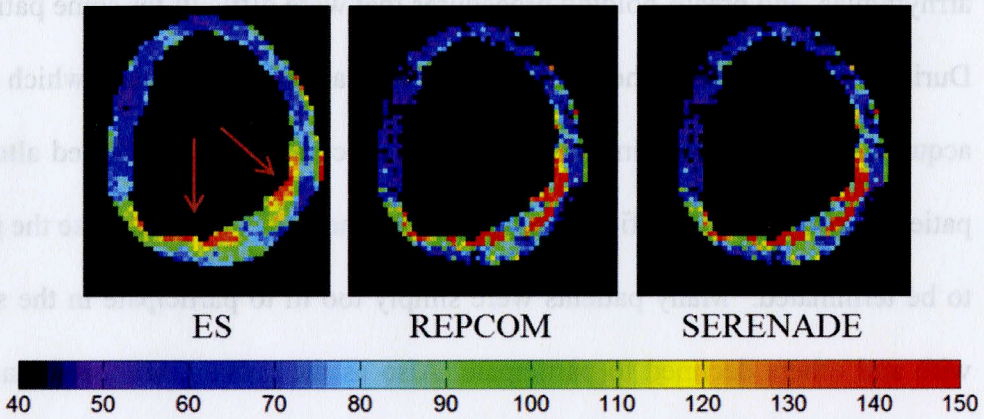

Figure 4.7. T_2 maps reconstructed with ES, REPCOM and SERENADE algorithms.

4.2. Conclusion

Acquiring data on patients in a clinical setting presented unique challenges: The reconstructed images of these patients were very different than those of healthy controls, exhibiting increased artifacts caused by metal objects (e.g. stents, wire-sutures), cardiac arrhythmias, and breath-holding procedures that were difficult for some patients to follow. During the clinical scan, the condition of some patients deteriorated, which made the data acquisition difficult, and in some cases, the process had to be aborted altogether. Some patients experienced significant anxiety during the scans, in which case the procedure had to be terminated. Many patients were simply too ill to participate in the study to begin with and others declined to participate. Also as the entire CMR examination generally takes more than an hour to complete, time constraints limited the amount of research data that we were able to obtain (typically only a few locations were imaged as opposed to the entire heart)

Despite these obstacles the cases presented here indicate that the DIR-RADFSE technique can be used to identify inflammation and fibrosis in the myocardium tissue as well as help assessing the viability of the heart. The high spatiotemporal resolution that this technique can produce is essential for an accurate diagnosis in the context of CMR, wherein small, but clinically relevant, changes in the myocardium are often hard to detect and distinguish from artifacts with techniques currently in use. Additional work is needed before the techniques described herein can be used clinically. In particular, in order to assess the benefit to patients we need to conduct a reproducibility study similar to the one described in Chapter 3.

Chapter 5

SUMMARY AND FUTURE WORK

CMR is a challenging field due to many sources of artifacts (e.g. cardiac motions, blood flow, and structures outside the FOV), the complex anatomy of the heart, and the limitation in the spatiotemporal resolution. To detect devastating myocardial diseases such as cardiomyopathy early, various CMR techniques have been developed in order to identify edema, which is an indication of inflammation in the myocardium. T_2-weighted images can be used to this end, however, the SI modulation depending on the TE point makes it difficult to identify with confidence regions of hyperintensity that may indicate edema. In contrast, the T_2 mapping with the DIR-RADFSE technique discussed in this thesis can provide high resolution TE images at sixteen different TE points and a T_2 map thus providing data with good spatiotemporal resolution from data acquired in a single breath-hold. Moreover, the radial acquisition used with the DIR-RADFSE is more robust to motion compared to the conventional Cartesian acquisition. With the optimization made to reduce various artifacts in this work, clinically significant changes in the myocardium may be better detected using T_2 mapping with the DIR-RADFSE.

5.1. Summary

In this thesis, the optimization of the DIR-RADFSE technique for CMR was discussed, and the reproducibility of T_2 mapping in the myocardium using various imaging conditions and three reconstruction methods (ES, REPCOM, and SERENADE)

was assessed. To test the efficacy of the various optimization conditions we used phantoms and human volunteers. As a result of the reproducibility study we found that in the SA orientation (the most commonly used imaging plane used to evaluate the heart), all optimized conditions showed excellent T_2 reproducibility irrespective of the algorithm used. The three times thick refocusing slice approach with FA of 180^{o} showed the best reproducibility by improving the refocusing slice profile, regardless of the algorithm used for T_2 reconstruction. When the ETL was shortened to reduce the acquisition window, lowering FA (i.e. 155^{o}) led to more reproducible T_2 estimates than reducing the RBW. Therefore, a reduced FA is a favorable setup when subjects present with a higher HR (> 80 bpm) where the reduction in the acquisition window is inevitable due to the rapid cardiac cycle.

Among the three algorithms tested, the ES-based method showed high T_2 reproducibility even with the data with lower SNR. However, the T_2 values obtained by the ES algorithm were higher than the PCA-based algorithms. This is most likely due to the magnitude operation used in the reconstruction of the TE images as shown in Section 3.10.3.

DIR-RADFSE was also evaluated in a clinical setting while the optimization and the reproducibility studies were being conducted. Case studies support the technique's capacity to detect clinical indications. The PCA-based T_2 maps were found to better estimate T_2 in areas around edges and in small structures. Ongoing clinical studies show that the T_2 mapping with DIR-RADFSE technique can characterize changes in the myocardium that may not be detected with other methods such as DE imaging.

5.2. Future work

Further work is needed in support of the clinical use of the technique. The intra-study reproducibility studies described in Chapter 3 need to be repeated using cardiac patients to characterize the reproducibility of T_2 values and the efficacy of the optimized conditions in this population. To complement this, inter-study reproducibility studies are also needed, and at present these are ongoing with healthy controls.

As discussed in Chapter 3, the complex fitting approach needs to be tested using ES-based T_2 mapping to achieve more accurate T_2 estimation. Within the PCA-based reconstruction methods, the effect of SNR and empty structures on T_2 estimates needs to be evaluated. Both the ES and the PCA-based methods have advantages and disadvantages and depending upon the experimental conditions one may be preferred over the other.

As mentioned in Chapter 4, one of the challenges in CMR is related to the time constraints of cardiac examinations. To reduce the setup time of the DIR-RADFSE scans, techniques for achieving optimal chemical shift signal suppression and SAT placement are desirable. For better chemical shift suppression of T_2 maps, an alternative approach is to use a phase-based chemical shift method developed by our group, the radial gradient and spin-echo acquisition (RAD-GRASE) strategy [19][20][21]. In the GRASE method the fat and water components as well as a T_2 map of the water component are generated with correction for the effects of field inhomogeneities. The method not only produces a T_2 map but also a lipid fraction map from the data acquired in a single breath-hold. In the GRASE technique, the fat component of the signal does not need to be suppressed during

the pre-scan, which reduces setup time. This technique is presently being optimized for CMR applications. Upon completion of this, the RAD-GRASE technique could be used for the detection of various cardiac diseases. For example, in addition to the disease conditions described in Chapter 4, arrhythmogenic right ventricular dysplasia (ARVD), a genetic disease of the myocardium, could be diagnosable via this technique owing to its ability to detect the lipid infiltrates characteristic of ARVD.

REFERENCES

1. Haacke, EM., et al. Magnetic Resonance Imaging: Physical Principles and Sequence Design. Wiley, 1999.

2. Nishimura, D. Principles of Magnetic Resonance Imaging. Stanford University, 1996.

3. Glover, G., et al. Projection Reconstruction Techniques For Reduction of Motion Effects in MRI, Magn Reson Med, 2009; 28:275-289.

4. Simonetti, OP., et al. Black blood T_2-weighted inversion recovery MR imaging of the heart. Radiology, 1996; 199:49-57.

5. Kim, D., et al. Breathhold multiecho fast spin-echo pulse sequence for accurate R_2 measurement in the heart and liver. Magn Reson Med, 2009; 62(2):300-6.

6. Giri, S., et al. T_2 quantification for improved detection of myocardial edema. J Cardiovasc Magn Reson, 2009; 11(56).

7. Huang, TY., et al. T_2 measurement of the human myocardium using a T_2-prepared transient-state TrueFISP sequence. Magn Reson Med, 2007; 57(5):960-6.

8. Altbach, MI., Barr, T., et al. T_2 mapping of the heart with high temporal and spatial resolution using a radial double inversion fast spin-echo pulse sequence with view sharing. Journal of Cardiovascular Magnetic Resonance, 2012; 14(suppl 1):O112.

9. Altbach, MI., et al., Processing of radial fast spin-echo data for obtaining T_2 estimates from a single k-space data set. Magn Reson Med, 2005; 54:549–559.

10. Block, KT., et al. Model-Based Iterative Reconstruction for Radial Fast Spin-Echo MRI. IEEE Transactions on Medical Imaging, 2009; 28: 1759-1769.

11. Huang, C., et al. T_2 mapping from highly undersampled data by reconstruction of principal component coefficient maps using compressed sensing. Magn Reson Med. 2012 May; 67(5):1355-66.

12. Ramsay JO, Silverman BW. Functional Data Analysis. Springer-Verlag, 1997, ISBN 0-387-94956-9.

13. Kumar, V., et al. Robbins Basic Pathology. Saunders/Elsevier, 2007, ISBN-10: 1416029737.

14. Friedrich, MG., et al. T_2-weighted imaging to assess post-infarct myocardium at risk. JACC Cardiovasc Imaging. 2011 Sep;4(9):1014-21.

15. Pell, GS., et al. Optimized clinical T_2 relaxometry with a standard CPMG sequence. Journal of Magnetic Resonance Imaging, 2006, 23:248–252.

16. Huang C, et al. Indirect Echo Compensated T_2 Mapping from Highly Undersampled Radial FSE Data with SERENADE. Proc. Intl. Soc. Mag. Reson. Med. 20 (2012): 362.

17. Lebel, RM., and Wilman, AH. Transverse Relaxometry with Stimulated Echo Compensation. Magnetic Resonance in Medicine, 64: 1005-1014 (2010).

18. Daniel, WW. BioStatistics. Wiley; 9th edition. 2010.

19. Reeder, SB., et al. Iterative decomposition of water and fat with echo asymmetry and least-squares estimation (IDEAL): application with fast spin-echo imaging. Magn Reson Med, 2005; 54:636-644.

20. Li, Z., et al. Fast Decomposition of Water and Lipid Using a GRASE Technique with the IDEAL Algorithm. Magn Reson Med 57:1047–1057, 2007.

21. Li, Z., et al. Rapid Water and Lipid Imaging with T_2 Mapping Using a Radial IDEAL -GRASE Technique. Magn Reson Med, 61:1415, 2009.

22. Altbach, MI., et al. Radial Fast Spin-Echo Method for T_2-Weighted Imaging and T_2 Mapping of the Liver. Journal of Magnetic Resonance Imaging, 2002; 16(2): 179–189.

23. Messroghli, DR., et al. Human Myocardium: Single-Breath-hold MR T_1 Mapping with High Spatial Resolution – Reproducibility Study Radiology March 2006 238:3 1004-1012.